Chapter 6
Nitrides of Boron and Group III Metals

In this chapter, *written by Yu.F. Zhukovskii* (*quantzh@latnet.lv*), theoretical models of 1D BN, AlN, GaN nanostructures as well as their properties are described and discussed.

Boron nitride semiconductors with stable *h*- and *c*-crystalline structures attract enhanced technological attention due to their unique properties. The formation of hexagonal BN NTs, both single- and multi-walled, can be considered as a result of the rolling-up of an *h*-BN(0001) honeycomb nanolayer (boronitrene), which is similar to the construction of carbon nanotubes from graphene. Like the latter, boronitrene is an almost flat hexagonal monolayer formed by a periodic network of sp^2 B-N bonds (where the influence of sp^3 bonding is neglected). Rolled-up SW and DW nanotubes as well as their bundles have been simulated in a large number of studies. According to the numerous publications, rolled-up BN NTs are the second most wide-spread type of nanotubes after CNTs. Other types of hollow 1D nanostructures of BN were simulated too, e.g., polyhedral nanotubes and nanoscrolls. To model BN NTs, both finite cage-like tubules (with either semi-fullerene caps or H-passivated edges) and periodic 1D nanotubes are used.

Equilibrium BN NT structures with different chiralities for single-, double- and triple-wall configurations, their cohesive, electronic and vibrational properties are studied by a number of methods: atomistic formalism of many-body empirical potentials, dynamical shell model, molecular dynamics and tight-binding methods, as well as the first principles methods of DFT-LCAO, PW DFT and DFT-LACW (Linearized-Augmented Cylindrical Waves). A growth mechanism for rolled-up single-wall BN nanotubes synthesized using the CVD (Chemical Vapor Deposition) method was simulated too.

The formation of BN nanoscrolls is dominated by two major energy contributions: an elastic energy increase caused by bending the BN layer (decreasing stability) and a free energy decrease generated by the van der Waals interaction energy of overlapping regions of the layer (increasing stability). As the structure is rolled up, the layer curvature increases before the layers overlap, and so do the torsion and inversion contributions to the strain energy. Thus, the rolled nanostructure becomes

less stable in relation to the undistorted (planar) configuration, which makes the transition from planar to rolled nanostructures energy-assisted.

Similar to diamond nanowires, theoretical studies on BN NWs were performed based mainly on their densely-packed c-BN structure. The structural, electronic and thermal properties of BN nanowires with optimized zinc-blende morphology were carefully simulated using the DFTB and molecular dynamics methods. The homogeneous BN NWs represented infinitely extended 1D prismatic crystallites cut from a c-BN crystal perpendicular to the (001), (111), and (110) section planes. BN NW stability strongly depends on the nanowire morphology. Apart from prismatic-type BN nanowires, theoretical simulations are performed also on BN nanofilaments of atomic diameters with the structure of the linear chain -B-N-B-N-, which can be doped by different atoms and functionalized. When joined to metallic electrodes (e.g., Al and Au) fragments of monoatomic BN filaments, which were found to be semiconducting, give rise to ballistic conductance along the linear $(BN)_m$ chains.

Two stable 3D morphologies of the technologically important group-III metal nitrides (AlN and GaN) are known: the hexagonal wurtzite (w) and the cubic (c) zinc-blende (sphalerite). 2D nanolayers of AlN and GaN were studied mainly for the densely-packed polar surfaces (0001) and (111) of the wurtzite and zinc-blende, respectively. A bilayer cut from the densely-packed n-type slabs with either w-(0001) or c-(111) termination forms buckled sp^3-bonded honeycomb 2D nanostructures, whose atop images are hexagonal like as those of the quasi-flat sp^2-bonded boronitrene.

Finite cage-like and infinite tubule models were used for the theoretical simulations on the SW AlN, GaN and $Al_xGa_{1-x}N$ nanotubes. Variation of Al concentration in $Al_xGa_{1-x}N$ nanotubes results in both linear and non-linear band gap change between the extreme values from the perfect GaN and AlN NTs. The latter are preferred in the growth of a faceted hexagonal-shaped nanotube wall continuing along the radial direction, analogously to faceted Si and SiC NTs. A wide spectrum of methods was applied in these calculations: atomistic formalism of the many-body empirical potentials, the method of molecular dynamics, DFTB and the ab initio PW DFT and LCAO DFT methods.

For the simulations of AlN and GaN nanowires, two traditional ab initio methods have been applied: the LCAO DFT and PW DFT. The latter method was used for the nanowires incorporated in the repeating tetragonal supercells of a dimension such that the interaction between NWs and their nearest images was negligible. The corresponding 1D NW models were exclusively chosen as those possessing a single-crystalline w-NW morphology (space group $P6_3mc$) with the growth direction along the [0001] axis, although the structure of their lateral facets could not be directly identified in the experiments. The cohesive, electronic, elastic and vibrational properties of AlN and GaN nanowires have been simulated so far. Both continuous and finite element models were used for the detailed description of mechanical (e.g., elastic) NW properties and their comparison with those found with the atomistic models.

6.1 Boron Nitride Bulk and Nanolayers

Boron nitride (BN) is a synthetic III–V compound with extraordinary mechanical, thermal, electrical, optical and chemical properties which are widely applied for various technological purposes [1]. First BN crystalline samples were synthesized at room temperature and atmospheric pressure as structures containing hexagonal sp^2-bonded monolayers isomorphic with graphene [2].

Stacked as planes, these honeycomb monolayers form a layered hexagonal boron nitride (h-BN), structurally similar to graphite, differed by the space arrangement of atoms in lattice [3], however, both described by the space group $P6_3/mmc$ [4]. In h-BN lattice, hexagonal rings of the basal planes are located directly above each other, with a sequence of atoms along vertical axis B-N-B-N-achieved via rotation between alternate layers by 180° (Fig. 6.1a). In graphitic structure (g-BN), only half of atoms of one plane lie above or below atoms of the adjacent layers while another half of atoms lie above or below the centers of the adjacent hexagons (as shown in Fig. 6.1b for h-BN with graphite structure). The former crystalline morphology was found to be energetically the most stable as compared to the latter or other structural polytypes of h-BN [4], due to larger electrostatic interaction between layers. Another essential difference between h-BN and g-BN is that the latter provides semi-metallic conductance mainly via noticeably delocalized π-electrons (with orbitals parallel to the honeycomb monolayers, while the ionicity of h-BN makes it a semiconductor with a wide band gap, experimentally estimated to be 5.97 eV [5].

The cubic allotrope of a non-layered BN with a sphalerite-type (zinc-blende) structure described by the space group $F\overline{4}3m$ and known as borazon (Fig. 6.2) is a synthetic material with the second highest hardness and thermal conductivity only
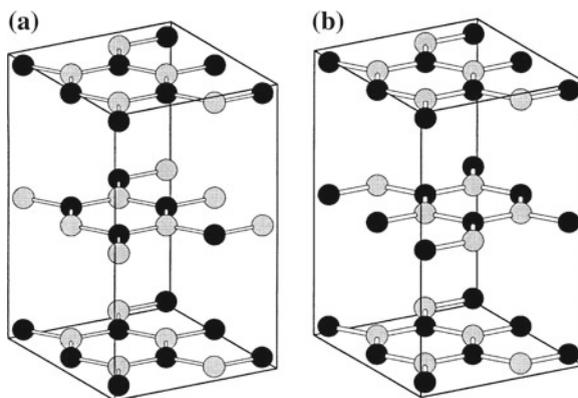
Fig. 6.1 Models of layered hexagonal binary BN allotropes with stable structures of h-BN (**a**) and graphitic g-BN (**b**). B and N atoms are shown as *gray* and *black balls*, respectively [4]
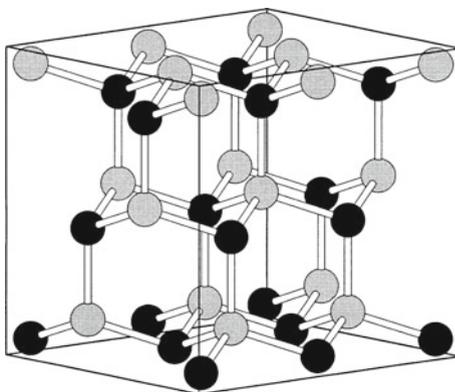
preceded by diamond [1]. In analogy to *c*-SiC considered in Sect. 5.4, *c*-BN is a
sp^3-bonded crystal acting as an electrical insulator and an excellent thermally stable
conductor of heat with a high resistance to oxidation. The cubic boron nitride can
be obtained under a high pressure and a high temperature treatment of *h*-BN [4].
Besides energetically stable *h*- and *c*-crystalline structures, several metastable phases
of boron nitride were also synthesized [1, 6]: (i) *w*- and *rs*-BN (wurtzite and rock-salt
structures, respectively, with sp^3 hybridization), (ii) *r*- and *t*-BN (sp^2 rhombohedral
and turbostratic structures, respectively) as well as (iii) amorphous *a*-BN. Unlike
SiC and the majority of pnictides, which crystallize mainly in sp^3 *c*- and *w*-phases,
whereas their sp^2 hexagonal phase was found to be rather metastable, *h*-BN can be
easy synthesized just as a stable compound and then be transformed to *c*-BN [1]. This
structural difference between similar types of binary compounds is obviously caused
by a specific nature of the chemical bonding in BN, which can be characterized by
considerable values of both ionicity (with charge transfer $1.01\,e$ from B to N atom)
and covalency (B-N bond population was estimated to be $0.58\,e$) [3]. The maximum
of the electron density is localized closer to the midpoint along the semi-covalent
bond, which can be explained by the proximity of ionic radii of B and N atoms as a
result of the electronic charge transfer [7].

The formation of hexagonal BN NTs, both single- and multi-walled, can be
considered as a result of the rolling up of an *h*-BN(0001) honeycomb nanolayer
(boronitrene) [8], analogically to the construction of CNTs from graphene. Simi-
lar to graphene, boronitrene is almost a flat hexagonal monolayer (Fig. 6.3) formed
by a periodic network of sp^2 B-N bonds (where the influence of sp^3 bonding is
neglected), without noticeable buckling observed in a SiC monolayer (Sect. 5.4) and
caused by a competition between sp^2 and sp^3 bonding. Figure 6.3 shows the fragment
of quasi-flat boronitrene.

Fig. 6.3 Fragment of BN(0001) layer: *top* and *across* views. B and N atoms are shown as *middle light* and *small dark balls* [3]
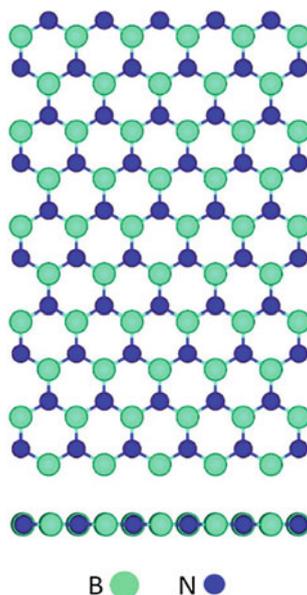
6.2 Boron Nitride Nanotubes

6.2.1 Polyhedral and Rolled-Up Single-Wall Nanotubes

Comprehensive experimental studies of BN nanotubes (e.g., their synthesis) were carried out beginning with the middle of 90s [9] when MW NTs with the inner diameters on the order of 1–3 nm and with the lengths up to 200 nm were produced in a carbon-free plasma discharge between a BN-packed tungsten rod and a cooled Cu electrode. Nowadays, BN NTs are synthesized mainly via catalytic vapor–liquid–solid (VLS) mechanism at a temperature higher than 1000 °C, using different experimental methods (arc discharge, laser ablation and chemical vapor deposition) [10–14]. The most efficient method for the production of BN NTs includes the heating of MgO (particularly doped by SnO) and a boron powder mixture followed by the formation of B_2O_2 gas and its further reaction with NH_3 [10, 14]. Under certain experimental conditions not only SW and MW BN NTs were synthesized but also ropes containing numerous SW or MW nanotubes of similar morphology (bundles) [14].

Since the mechanism of BN NT growth is still not well defined [15], its theoretical simulations continue to attract enormous attention. A large number of atomistic calculations on BN nanotubes (regular, deformed and defective) have been performed so far for both SW and MW NT models of armchair, zigzag and chiral morphology possessing a wide range of uniform diameters (0.5–5 nm) as well as for their bundles. According to the total number of publications, the rolled-up BN NTs is the second widespread type of nanotubes after CNTs. Other types of hollow 1D nanostructures of BN were simulated too, e.g., nanoscrolls [16] and nanoarches [17]. To model BN

NTs, both finite cage-like tubules (with either semi-fullerene caps or H-passivated edges) [16, 18–20] and periodic 1D nanotubes [3, 8, 17, 21–42] were used. A number of methods were applied for their calculations: atomistic formalism of many-body empirical potentials [27], dynamical shell model [24], molecular dynamics [16, 18, 20], semi-empirical tight-binding (TB) methods [19, 23] and MNDO [15], first principles methods of DFT-LCAO [3, 17, 19, 20, 32, 35, 38–40, 42] as well as DFT-PW [8, 21, 22, 25, 26, 28–30, 33, 34, 37, 38, 41] and DFT-LACW (Linearized-Augmented Cylindrical Waves) [36]). In a few theoretical studies parallel with the prediction of the nanotube morphology and the electronic structure, the elastic and vibration properties were analyzed [20, 23–26, 29, 39] as well as thermodynamic conditions for the growth of nanotubes from nuclei [15, 18] and dislocation formation as a result of the strain relief [20].

In spite of the flat structure of boronitrene (Fig. 6.3), the polyhedral model for single-wall boron nitride nanotubes presents a two-shell structure [41]. Within this formalism, the boron atoms have a flatter structure of bonds, which are located closer to the nanotube axis as compared to the nitrogen atoms, which are fixed at pyramidal vertices above a triangular-type boron 1D polyhedron marked by gray lines (Fig. 6.4). The appearance of buckling in BN nanotubes of small diameters can be understood by re-hybridization and the weakening of π-bonds caused by the nanotube curvature [27]. As a result, B atoms tend to keep the sp^2 bonding with inter-bond angles of 120° while N atoms adhere an admixture of sp^3 hybridization, which leads to a smaller bond angle. These effects are contributive to the change of bond lengths and diameters in BN NTs. Except for buckling effects, boron nitride nanotubes with polyhedral quasi-hexagonal morphology (marked by black lines) constructed for different chiralities (Fig. 6.4) look qualitatively similar to the corresponding polyhedral models of CNTs. Optimization of the bond lengths and inter-bond angles in such models of both BN NTs and CNTs was performed using the DFT-GGA method [41].

(6,0) zigzag   (5,3) chiral   (5,5) armchair
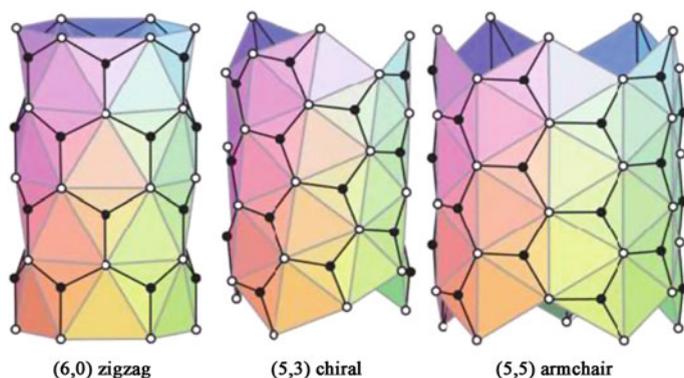
Fig. 6.4 General polyhedral models of BN nanotubes for three types of chirality. B and N atoms are shown as *white* (*hollow*) and *black balls* (Reprinted figure with permission from Lee et al. [41], Copyright (2010) by the Royal Society of Chemistry)

A number of SW BN NT simulations performed within the traditional rolled-up model, mainly for *ac*- and *zz*-chiralities, considered dependencies of different nanotube properties on gradually growing diameter D_{NT} varied from 0.5 up to 5.0 nm [3, 25–27, 35, 39]. Similar to *ac*- and *zz*-SiC nanotubes described in Sect. 5.5.1, both (6,6) and (12,0) SW BN NTs possessing the diameters of 8.4 and 9.6 Å, respectively, are shown in Fig. 6.5a, b [3]. The effect of buckling in these BN nanotubes reduces with the growth of their diameters (Fig. 6.6) achieving practically negligible values for SW BN NTs of larger diameters shown in Fig. 6.5c, d (24.9 and 28.7 Å corresponding to (18,18) and (36, 0) chirality indices, respectively).

Since hypothetical SW BN NTs with the infinite diameter should coincide with a boronitrene layer, a consequent growth of nanotube diameters leads to a substantial decrease of strain energies per formula unit, as defined in (6.1) and shown in Fig. 6.7a, similarly to that considered for Si NTs (Sect. 5.2.1). At the same time, the values of bond lengths (d_{B-N}), effective atomic charges (q_B and q_N) as well as the band gap ($\Delta\epsilon_{gap}$) (Fig. 6.7b) approach to the same values as were calculated for the BN(0001) nanolayer (1.44 Å, 0.99 e and 7.09 eV, respectively) [3].

$$E_{strain} = \frac{1}{m}(E_{NT} - kE_{slab}), \qquad (6.1)$$

(a) optimized single-wall (6,6)*ac*-BN NT (aside and across images), $D_{NT} = 0.84$ nm;

(b) optimized single-wall (12,0)*zz*-BN NT (aside and across images), $D_{NT} = 0.96$ nm;

(c) optimized single-wall (18,18)*ac*-BN NT (aside and across images), $D_{NT} = 2.49$ nm;

(d) optimized single-wall (36,0)*zz*-BN NT (aside and across images), $D_{NT} = 2.87$ nm.
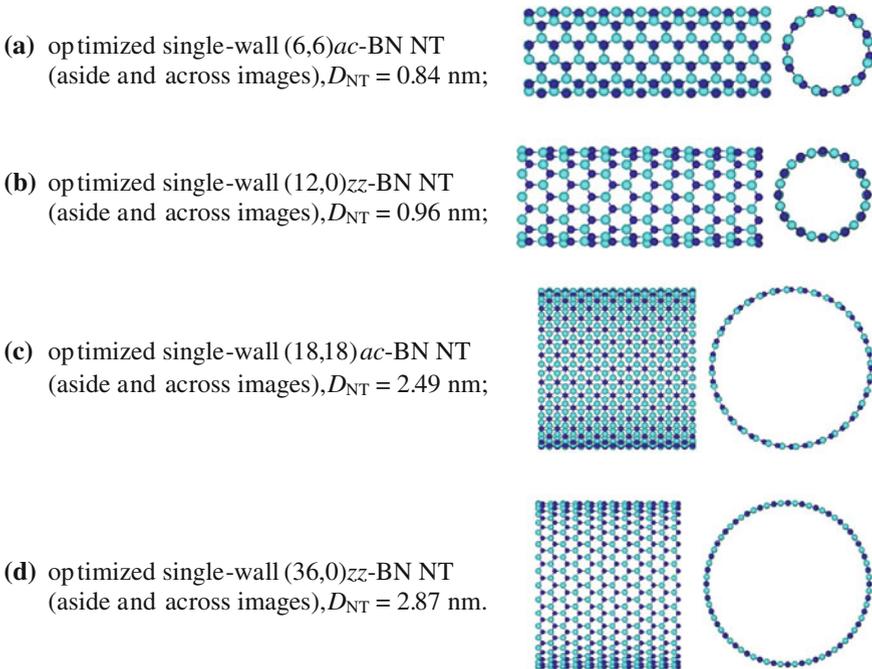
Fig. 6.5 Lateral and cross-section images of rolled-up SW BN NTs of different diameters possessing different chiralities. B and N atoms are shown as *light* and *dark balls*, respectively [3]
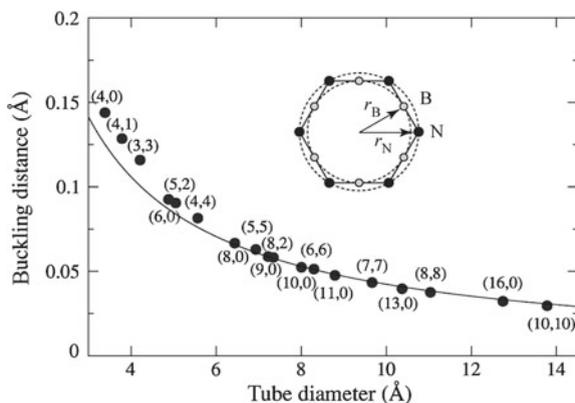
Fig. 6.6 Buckling distance in BN single-wall nanotube ($\delta r_{\text{BNNT}} = r_{\text{N}} - r_{\text{B}}$) as a function of NT diameter [25]

where k is a number of slab unit cells with the same number of BN formula units (m) as in nanotube unit cells, while E_{NT} and E_{slab} are the total energies *per* corresponding unit cells. The energy curves $E_{strain}(D_{\text{NT}})$ for BN nanotubes of both chiralities qualitatively coincide for $D_{\text{NT}} > 1.0$ nm (Fig. 6.7a), i.e., just NT diameter determines the strain energy. As to $\Delta\epsilon_{gap}(D_{\text{NT}})$ curves (Fig. 6.7b), they approach to each other and to the gap of BN nanolayer for $D_{\text{NT}} > 1.5$ nm. On the other hand, because of some distortion of B-N bonds, their orientation in relation to the NT axis as well as due to the nanotube buckling, the dependences of arbitrary $d_{\text{B−N}}$ and $q_{\text{B}}(q_{\text{N}})$ on D_{NT} and NT chirality are quite complicated [35]. Moreover, Fig. 6.7 shows that the properties of ultrathin BN NTs, e.g., those corresponding to indices (4,4) and (6,0) for *ac-* and *zz*-chiralities, respectively, substantially differ from the properties of thicker SW NTs, which can be explained by a slightly different bonding nature in the former ones, as described above.

6.2.2 Vibrational Properties of Rolled-Up Single-Wall Nanotubes

Reproducible synthesis of single-wall BN NTs and experimental studies of a number of their structural, electronic and vibrational properties [43, 44] provide possibilities for reliable verification of the corresponding theoretical predictions. One of the most convenient and effective experimental tools for identification of SW NTs was found to be Raman and infrared (IR) spectroscopy [44]. A number of phonon calculations for CNTs were performed using the force constant approach [45, 46] where these interatomic constants were fitted to experimental data up to the fourth nearest-neighbor interaction. Such an approach provides a fast estimate and, in combination with the zone-folding method (i.e., finding of the nanotube phonon frequencies from those of a corresponding nanolayer to be rolled into it) [46], results
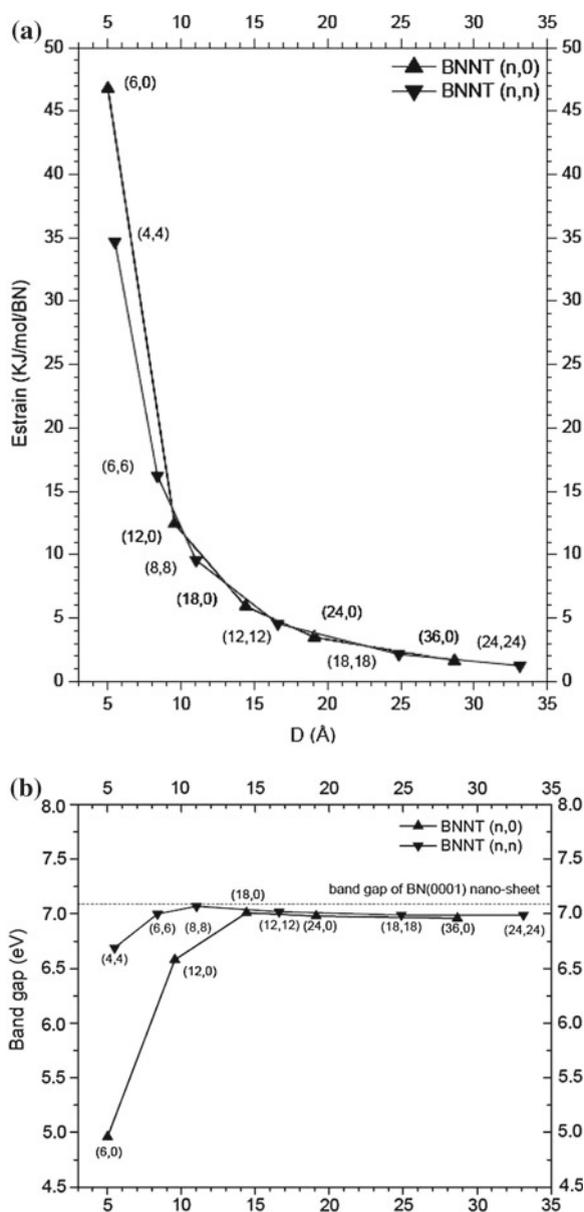
Fig. 6.7 Strain energies (**a**) and band gaps (**b**) of *ac*- and *zz*-BN nanotubes (Fig. 6.5) as functions of NT diameters [3]

in a good qualitative understanding of the vibrational properties of the nanotubes. Going beyond the force constant approach, the phonon dispersion in CNTs was calculated using tight-binding, DFT-LCAO and DFT-PW techniques, but the latter was

Fig. 6.8 Phonon dispersions and VDOSs for *ac*-BN NT calculated using ab initio and zone-folding methods. The *solid and dotted lines* in VDOS panel (**c**) correspond to the two plots of vibrational band structure (**a** and **b**), respectively. The *boxes* and *asterisks* in the left panel are described in text [25]
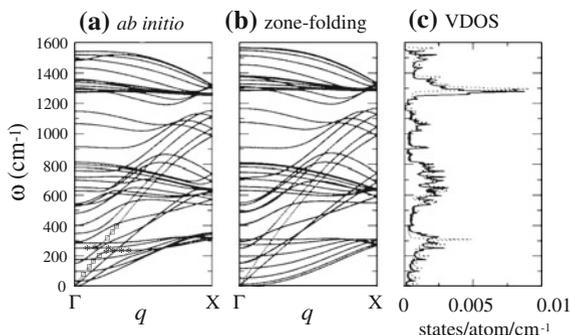
estimated as a more precise due to a better agreement with the experimental data [47]. The phonons in SW BN NTs have been calculated so far using the TB technique [23], the dynamical shell model [24], as well as ab initio methods of DFT-PW [25, 26, 29] and DFT-LCAO [39].

The phonon dispersion relations as well as the corresponding vibrational densities of states (VDOSs) obtained for a (6,6) BN nanotube using the first principles and zone-folding methods [25] are compared in Fig. 6.8. (A similar comparison was recently made for polyhedral Si NTs as considered in Sect. 5.2.4 [48].) Both approaches differ mainly in the low-frequency part of the spectrum, due to the coupling of in-plane and out-of-plane modes of nanolayer upon rolling into a nanotube. This results in a stiffening of the low-frequency nanotube modes. Another pronounced difference is the avoided crossings in the ab initio dispersion relation. According to the non-crossing rule of von Neumann and Wigner [49], the energy levels of modes, which have the same symmetry, do not cross when an adiabatic parameter (the phonon wave vector in this case) is changed. A prime example is the longitudinal (L) optical mode marked by boxes, which starts from zero frequency at Γ point of the Brillouin zone with the same slope as the L mode of nanolayer and displays evidently avoided crossing with the radial breathing mode (RBM at 251 cm^{-1}) marked by asterisks. Both modes possess A_1 symmetry at point Γ (Fig. 6.8). Figures 6.9 and 6.10 demonstrate the mapping of the three optical modes of nanolayer at Γ point onto the corresponding A modes of *zz*-NT [25]. The out-of-plane optical
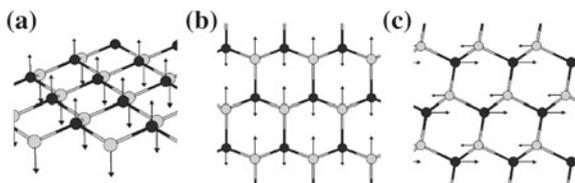
Fig. 6.9 Sketch of the optical phonon modes at Γ point in hexagonal BN nanolayer: **a** out-of-plane (ZO) mode, **b** transverse optical (TO) mode, and **c** longitudinal optical (LO) mode. (B and N atoms are shown as *light gray* and *black balls*.) For the assignment of "transverse" and "longitudinal", the phonon wave vector points in a horizontal direction with $q \to 0$ [25]

Fig. 6.10 Sketch of high-frequency A modes in zz-BN NT: **a** radial buckling (R) mode, **b** bond-stretching or longitudinal (L) mode, and **c** bond-bending or tangential (T) mode [25]
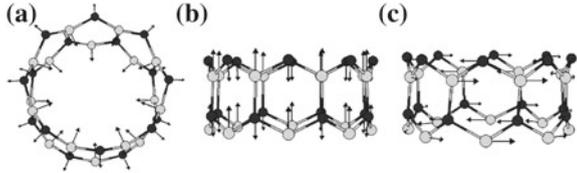
(ZO) modes of nanolayer transform to radial "buckling" (R) nanotube modes where all B atoms move inwards (outwards) simultaneously and all N atoms move outwards (inwards), giving rise to an oscillation of the NT buckling amplitude. The transverse optical (TO) mode of BN nanolayer maps onto the L NT mode, and, accordingly, the longitudinal optical (LO) mode of nanolayer maps onto a transverse or tangential (T) NT mode. In the A modes, all atoms along the circumference move in phase. In the modes of E_i symmetry, there are $2i$ nodes along the circumference (i nodal planes containing the symmetry axis of the tube). The B modes of NTs (n, n) and $(n,0)$ contain $2n$ nodes along the circumference which means that a rotation by certain angle (with the proper translation along the tube axis) maps the mode onto its negative. In other words, for the B modes, the neighboring "columns" of atoms oscillate with a phase difference of π [25].

The points in the BZ of BN nanolayer give rise to the Raman- and IR-active A, E_1 and E_2 modes of NT. With a larger NT diameter (when increasing n of (n,n) and $(n,0)$ nanotubes), the BZ points giving rise to the E_1 and E_2 modes converge towards BZ point of the BN(0001) nanolayer. Therefore, for a rough estimate of the frequencies of active modes for NTs of larger diameters, it is sufficient to look at the frequencies at Γ point of nanolayer [25]. For example, the frequencies of modes that correspond to the acoustic branches of nanolayer converge accordingly to zero for large NT diameters. Not all of the A, E_1 and E_2 modes can be Raman active, e.g., the TO mode of a BN nanolayer at Γ point (Fig. 6.9b) folds into a nanotube mode of A_1 symmetry (Fig. 6.10b) and, thus, is Raman active, whereas the LO mode of the nanolayer at Γ point (Fig. 6.9c) folds into a mode of A_2 symmetry (Fig. 6.10c), which changes a sign under reflection at a plane that contains the nanotube symmetry axis.

Figure 6.11 displays the frequencies of the Raman and IR-active modes of zz-BN NT (Fig. 6.5b, d) as a function of nanotube diameter where ab initio values are plotted as figured labels (which filling corresponds to active and inactive modes) while the zone-folding values are connected by lines, to guide the eye and extrapolate to larger NT diameters. The three frequency regimes can be easily distinguishable in Fig. 6.11 [25]:

(1) The low-frequency modes whose frequencies approach zero (for $D_{NT} \to \infty$) are the modes derived from the acoustic branches of BN nanolayer (ZA, TA and LA, according to the classification given in Fig. 6.9).
(2) The three modes that approach $\omega \approx 818 \, \text{cm}^{-1}$ (for $D_{NT} \to \infty$) are radial (R) modes (Fig. 6.10a) related to the optical out-of-plane (ZO) modes (Fig. 6.9a).
(3) The high-frequency regime above $1200 \, \text{cm}^{-1}$ consists of longitudinal (L) and transverse (T) modes (Fig. 6.10b, c respectively) which are zone-folded TO and LO modes of BN nanolayer (Fig. 6.9b, c respectively).

Fig. 6.11 Raman- and IR-active modes in *zz*-BN nanotubes as functions of NT diameter: comparison of ab initio and zone-folding values (marked as figured labels and lines, respectively). The shape of labels denotes the symmetry of the modes as shown in the legend positioned below. *Black filling* marks modes active in Raman spectra only, *while gray filling* stands for modes which are both Raman and IR active. R, L, and T mark the radial, longitudinal, and tangential high-frequency nanotube modes (Fig. 6.10) while RBM is a radial breathing mode [25]
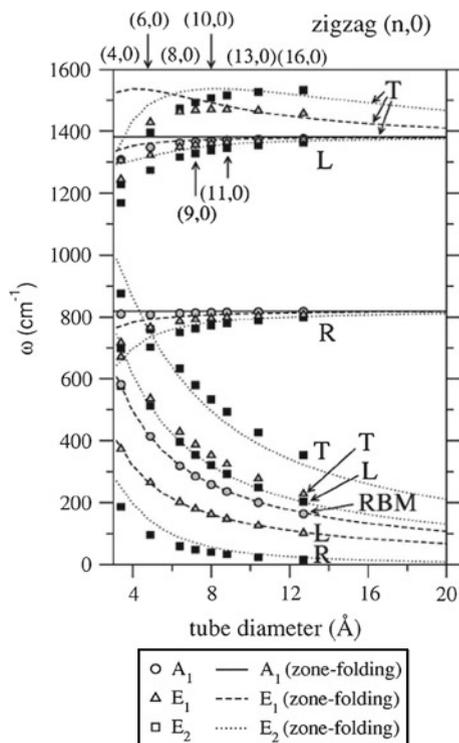
Although the three different frequency regimes were discussed separately only for the case of *zz*-BN NTs (Fig. 6.11), they were also considered for the chiral and armchair nanotubes [25]. Analogically to CNTs, the inverse proportionality of RBM to the NT diameter ($\omega_{RBM} \propto 1/D$) was found to be true also for BN NTs. In fact, not only the radial breathing mode, but most of the low-frequency modes display the same $1/D$ scaling. Only the frequency of the lowest E_2 mode displays $1/D^2$ proportionality [47]. For small BN NT diameters, the phonon modes deviate from the functional form A/D or A/D^2, because the linear quadratic behavior in the acoustic branches of BN nanolayer ceases to be valid further away from Γ point. Only the RBM follows the functional behavior A/D down to very low diameters [25].

A combined study of BN nanotubes by Raman and IR spectroscopy can serve to distinguish armchair nanotubes (where IR- and Raman-active modes are disjoint) from chiral and zigzag NTs, where the IR-active modes are a subset of the Raman-active modes. In particular, the radial breathing mode is both Raman and IR active for chiral and zigzag NTs, but only Raman spectra are active for armchair nanotubes, which make them a universal tool for experimental studies on single-walled nanotubes with a hexagonal morphology.

The further progress of theoretical simulations on the Raman spectra was the expansion of the bond polarization model, which was developed earlier for a descrip-

tion of the non-resonant Raman intensities of metallic CNTs [46], for the case of semiconducting BN NTs [29].

The basic assumption of the bond-polarization model [50] was that the total polarizability can be modeled in terms of the single bond contributions. Each bond was assigned a longitudinal polarizability, α_l, and a polarization perpendicular to the bond, α_p. Thus, the polarizability contribution of a particular bond d was defined as [29]:

$$\alpha_{ij}^d = \frac{1}{3}(2\alpha_p + \alpha_l)\delta_{ij} + (\alpha_l - \alpha_p)(R_i R_j - \frac{1}{3}\delta_{ij}) \qquad (6.2)$$

where $\boldsymbol{R}$ is a unit vector along the bond. The second assumption was that the bond polarizabilities depend only on the bond length $|\boldsymbol{R}|$. Comparison of the non-resonant Raman spectra, calculated for ac- and zz-BN nanotubes of different diameters using both the ab initio method (as described above [25]) and the bond-polarization model [50], is given in Fig. 6.12. The Raman spectra were averaged over the polarization of the incoming and scattered light.
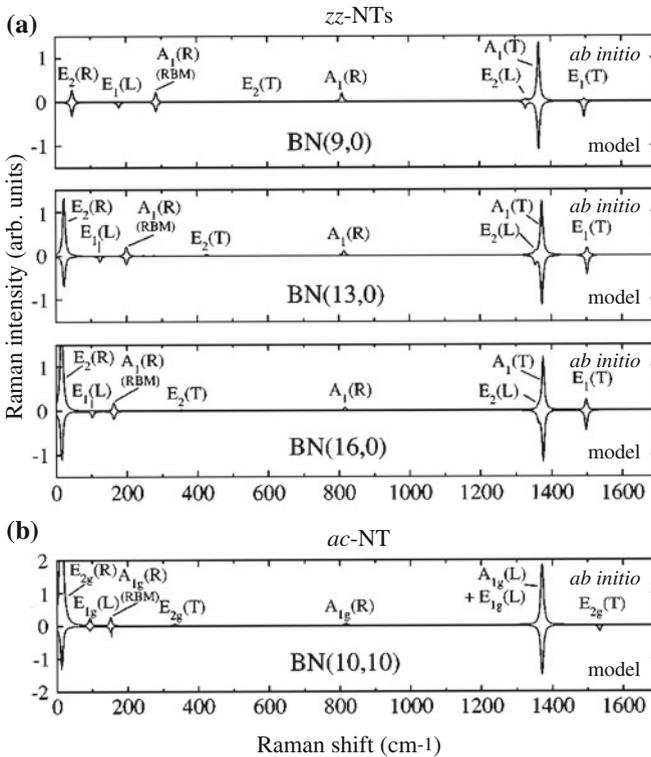
Fig. 6.12 Raman spectra for different BN NTs (**a** and **b**): comparison of ab initio calculations (*positive axis*) with the bond-polarization model (*inverted axis*) [29]. The symmetry assignment was described elsewhere [51]. The R, T and L modes are defined in Fig. 6.10 [25]

The peaks of zz-BN NTs below $700 \, cm^{-1}$ arise due to low-frequency phonon modes derived from the acoustic modes of BN nanolayer whose frequency scale is inversely proportional to the NT diameter (except for the $E_2(R)$ mode, which scales with the inverse square of the diameter) [29]. The $E_2(R)$ mode gets quite intense with the increasing D_{NT}, but its frequency is so low that it is hard to distinguish it from the strong Raleigh-scattering peak in experiments. The $E_1(L)$ peak possesses practically vanishing intensity in the ab initio spectrum and is overestimated in the bond-polarization model. The radial breathing mode yields a clear peak that should be easily detectable in Raman measurements of BN NTs, just as in the case of CNTs. Both ab initio and bond-polarization model calculations yield a similar intensity for this peak. The high-frequency modes above $700 \, cm^{-1}$ are derived from the optical modes of BN nanolayer and change weakly with the diameter. The $A_1(R)$ mode at $810 \, cm^{-1}$ gives a small contribution that might be detectable. The intensity decreases, however, with the increasing diameter. The bond-polarization model only yields a vanishingly small intensity for this peak. At $1370 \, cm^{-1}$ a clear signal is given by the $A_1(T)$ mode, which has a very similar intensity both in ab initio and model calculations. The small side peak at a slightly lower frequency is due to the $E_2(L)$ mode. The $E_1(T)$ peak at $1480 \, cm^{-1}$ is gaining intensity with the increasing nanotube radius. The overall Raman spectrum for ac-BN (10,10) nanotube exhibits trends similar to those of zz-BN NTs [29].

6.2.3 A Growth Mechanism of Rolled-Up Single-Wall Nanotubes

While theoretical studies of CNT growth mechanisms based on different approaches are quite widespread during the last ten years [52–63], only a limited number of analogous studies on growth of BN NTs have been performed so far [15, 38, 43] although morphologically both types of hexagonal nanotubes are similar. One of the key reasons for this difference is the composition of BN NTs from the two different atomic species unlike monatomic CNTs, which makes the synthesis of the former more complicated [38]. CNTs are typically synthesized from hydrocarbon precursors when using the CVD (Chemical Vapor Deposition) method [64] and, according to the current theoretical understanding of the CNT formation process, individual carbon atoms diffuse in or on a catalytic metal nanoparticle, forming graphene-like flakes $(C_n)_{ads}$ that eventually give rise to their swelling after the appearance of pentagonal defects within a honeycomb structure [63]. A metallic substrate can assist in saturating the dangling bonds of flakes at their borders in favor of the formation of semi-fullerene-like embryos with the energy cost due to the curvature induced by the presence of periodically distributed pentagons, the appearance of which can be accelerated by a defective structure of the catalytic particle. A further step includes a gradual growth of this nucleus to a capped CNT under the influence of a permanent flux of the hydrocarbon molecules towards the interface between the metallic substrate and the graphitic adsorbate [55].

Assuming that the aforementioned ideas are relevant also to the growth of BN NTs, it is important to understand the factors that determine whether individual nitrogen and boron atoms diffusing on a catalytic surface result in the formation of capped BN embryos. The first principles calculations were performed [38] in order to confirm this prediction and to study the behavior of N_2, B_2, and BN molecules on an iron catalyst where the precursors used for producing BN NTs were already decomposed into individual B and N atoms and adsorbed upon the catalyst. The stepped *bcc*-Fe(110) surface was chosen as a typical catalytic substrate used for CVD growth. It was shown that B_2 formation dominates on flat terraces of the iron substrate, while at step edge regions BN formation is the most favorable reaction (Fig. 6.13).

The thermodynamic analysis of BN NT nucleation upon a catalytic surface was performed [15] to obtain a functional dependence of embryo's structure on the reaction parameters. At the beginning of nucleation, a few B and N atoms precipitate on the surface of a metal particle already saturated with them previously being combined into nanostructures with B and N atoms arranged in hexagons, which transform to a flat graphene-like nanolayer bonded with its edges to the metal surface (Fig. 6.14). This form of the nucleus is the most favorable because of the elimination of dangling bonds in the BN cluster as considered above. BN NT nucleus significantly differs from that of CNT, the closure of which requires the insertion of six pentagon C rings into the hexagonal network. Indeed, the insertion of pentagon (or any other odd-member rings) in BN NT nucleus results in the formation of weak B-B and N-N bonds and, therefore, is energetically unfavorable [15]. Since the closure of BN NT requires the insertion of three or four four-membered (tetragonal) rings and one octagonal ring, primary nuclei can be structurally different. Figure 6.14 shows the mapping diagram
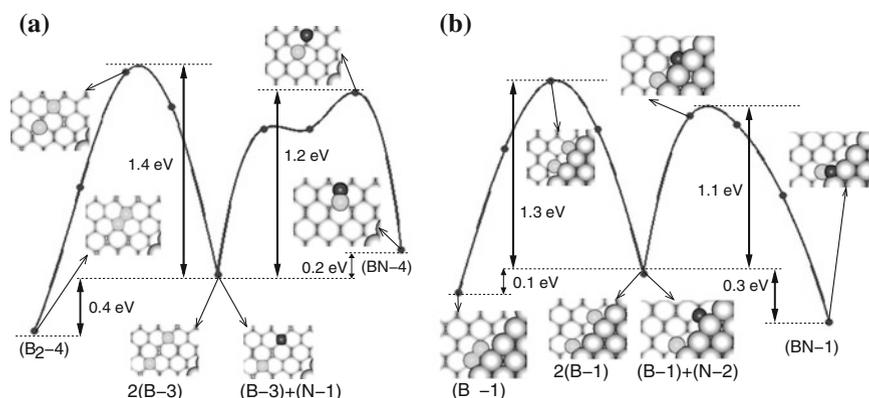
Fig. 6.13 Reaction barriers along a few reaction paths upon the stepped *bcc*-Fe(110) surface (where the external terrace is shown brighter than the internal one) for **a** reactions at the terrace $[2(B-3)] \rightarrow (B_2-4)$ and $[(B-3)+(N-1)] \rightarrow (BN-4)$ as well as for **b** reactions at the step edge $[2(B-1)] \rightarrow (B_2-1)$ and $[(B-1)+(N-2)] \rightarrow (BN-1)$. *Middle gray* and *small black* balls correspond to boron and nitrogen atom, respectively. The zero of energy for reactions $X^* + Y^* \rightarrow XY^*$ is fixed at the energy $E(X^* + Y^*)$, where both X and Y are at the same unit cell. The zero of energy for competing reactions forming B_2 and BN are set at the same value, in order to make the comparison of energy barriers easier [38]
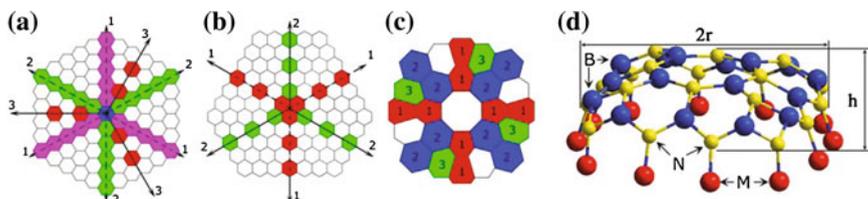
Fig. 6.14 Three principal types of BN NT nucleus: **a** with a BN hexagon at the *top* of the end cap (placement of tetragons in "1" or "2" locations results in the formation of *ac*-NTs, while placement in "3" locations results in the formation of *zz*-NTs, while arbitrary combination of "1", "2" or white results in the formation of chiral nanotubes); **b** with "star structure" (single atom of B (or N) at the *top* of the end cap (placement of tetragons only in "1" or "2" locations results in the formation of *zz*-NTs, any other combinations of locations result in the formation of chiral nanotubes); **c** octagonal ring at the top of the end cap (placement of tetragons only in "1" or "2" locations results in formation of *ac*-NTs armchair tubes, their placement in "3" locations results in the formation of *zz*-NTs, while any other combinations of locations results in the formation of chiral tubes). **d** Optimized structure of one of possible BN nuclei used for both semi-empirical calculations and thermodynamic modeling (Reprinted figure with permission from Kuznetsov et al. [15], Copyright (2007) by the WILEY-VCH Verlag GmbH & Co. KGaA, Weinheim)

used to generate armchair, zigzag and chiral caps where a combination of the mentioned rings constitutes the morphology of each nucleus. Structures of all types of end caps presented in Fig. 6.14 were optimized using semi-empirical MNDO, etc. methods, in order to analyze trends in the calculated heats of formation for each model [15].

6.2.4 Bundles of Rolled-Up Single-Wall Nanotubes

According to the experimental data, e.g., scanning electron microscopy (SEM), the ensemble of BN NTs grown from the adjacent Fe catalyst particles, using the method of laser ablation, tends to form vertical bundles [43]. The growth of these BN NTs is obtained through the optimum combination of Fe nanoparticles thickness, the laser energy density (deposition rate), and the substrate bias. For example, for the substrate with 12.5 nm thick Fe film at a substrate bias of -300 V [65], the resultant excessive deposition rate generates a coating of BN films on the Fe nanoparticles (Fig. 6.15a). Under these conditions, the deposition rate of BN films is faster than the diffusion rate of grown BN species into the Fe catalyst particles. Thus, BN films coated on the catalyst terminate the contact between Fe and the reactive growth species; this phenomenon is termed the poisoning effect. The thickness of BN films gradually decreases as the substrate bias increases (Fig. 6.15b). BN NTs start to grow at a higher substrate bias as a balance is reached between the rate of film deposition and the re-sputtering rate (Fig. 6.15c). At this total re-sputtering region, there is a suppression of the deposition of BN thin films. BN NTs grow on Fe nanoparticles according to the VLS (Vapor–Liquid–Solid) mechanism. Plasma creates a directional flux of the grown BN species with sufficient kinetic energies, to diffuse into Fe
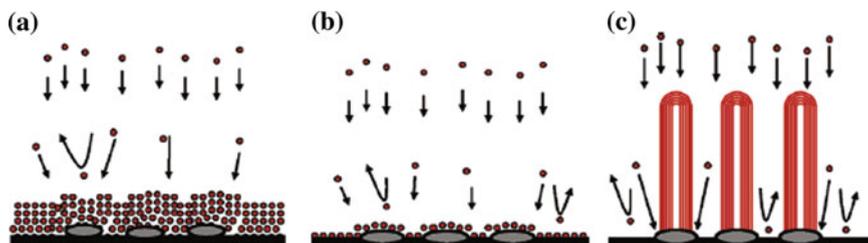
Fig. 6.15 Schematic drawing representing the growth region of BN NT bundles. **a** Deposition of BN nanoflakes on Fe nanoparticles due to low re-sputtering rate of the growth species. **b** Reduced growth rate of BN films with an energetic growth species. **c** Total re-sputtering region wherein BN NTs grow and BN films are suppressed (Reprinted figure with permission from Wang et al. [65], Copyright (2005) by the American Chemical Society)

nanoparticles, which capture and confine them in a nanoscopic space; otherwise, they are re-sputtered off. Super-saturation of Fe nanoparticles with BN vapor causes BN species to condense into the ordered nanotubular structures [65].

Although BN SW NTs can be synthesized as separated nanostructures, they were found to be more stable in bundle forms, due to a considerable inter-tube attraction caused by the polarity of B-N bonds [32]. It plays an essentially more important role than in the case of SiC NT bundle formation as considered in Sect. 5.5.2 not speaking about CNT bundles [66, 67]. Moreover, specific inter-tube interaction in BN SW NT bundles suggests the possibility of more diverse phase transitions in them under the external pressure, which could lead to new crystalline phases with unique structures, novel properties, and potential applications [33]. Nowadays, ensembles of BN NT bundles are not only the basis of many fundamental and significant designs in electronic devices and functional materials (such as super tough fibers, field effect transistors, field emission displays, etc.) but are also ideal media for atomic (e.g., Li, H, and inert gases) or molecular (e.g., H_2) storage [68].

The influence of transverse pressure on the phase transition processes of the aligned crystalline bundles of BN NTs was studied using the first principles calculations on periodic ensembles of the identical nanotubes with *ac* [30, 33] and *zz* [32] chiralities, respectively. The cohesive energy versus *ac*-bundle 2D-lattice constant dependencies shown in Fig. 6.16a illustrate that isolated SW BN NTs would be bundled together spontaneously until $a = 11.5$ Å (a total energy minimum), which corresponds to the inter-tube separation of ∼3.36 Å, consistent with the experimental fact that BN NTs are usually produced in the bundle forms [69]. When *a* is decreased from 11.5 Å under the conditions of the transverse pressure, the total energy of a bundle increases, thus, smooth nanotube walls begin to buckle, which is accompanied by the formation of inter-tube bonds (Fig. 6.16b). At $a = 8.5$ Å, the coordination number of each atom clearly changes from 3 to 4, showing that the energy-consuming $sp^2 \rightarrow sp^3$ transition is achieved (fragment of bundle at the middle of Fig. 6.16b). With the continuously decreasing *a*, each NT is elongated more and more greatly along the nanotube axis until those intra-tube B-N bonds, which are not perpendicular to the NT axis (NPBs), get broken, resulting in the formation of a new layered
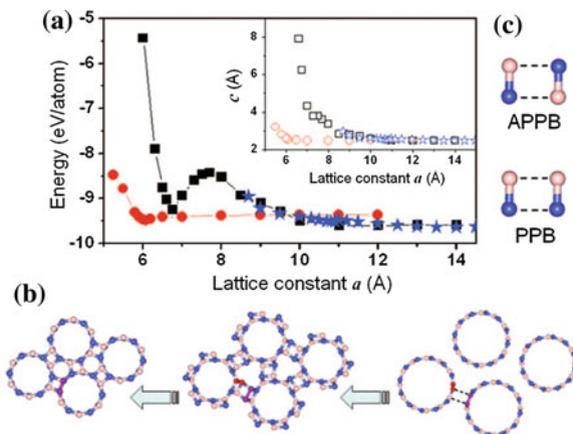
Fig. 6.16 **a** Variations of cohesive energy and lattice constant *c* (*inset*) versus in-plane lattice constant *a* for bundles of (3,3) (*circles*), (6,6) (*squares*), and (8,8) (*stars*) BN NTs. **b** Top view of atomic structures of (6,6) BN NT bundles at $a = 11.0$ (*right*), 8.5 (*middle*), and 6.75 Å (*left*). The bonds with circular and squared labels on the energy curves correspond to intra-tube B-N bonds which are not perpendicular and perpendicular to the NT axis, respectively. *Dashed lines* illustrate a pair of APPBs (*anti-parallel polar bonds*). **c** Patterns of two B-N bond arrangements, APPBs and PPBs (*parallel polar bonds*) between the adjacent nanotubes. *Light* and *dark balls* represent B and N atoms, respectively (Reprinted figure with permission from Hao et al. [33], Copyright (2008) by the American Chemical Society)

porous phase of BN at $a = 6.75$ Å [33]. This step of $sp^2 \rightarrow sp^3$ transition has an exothermic process from $a = 7.7$ down to 6.75 Å. The relative spatial orientations of polar B-N bonds of the adjacent NTs characterize the corresponding inter-tube inter- action for the understanding of the bonding character in bundles under the transverse pressure: (i) in the case of the antiparallel polar bonds (APPBs) arranged between the adjacent NTs (Fig. 6.16c), the external pressure can help the neighboring nanotubes to overcome the deformation energy, to form the inter-tube bonds in the first step of phase transition crucial for the subsequent new phase formation; (ii) the parallel polar bonds (PPBs) arrangement leads to the "frustrated" B-B and N-N bonds, rather than the inter-tube hetero-nuclear B-N bonds. Thus, the results of the calculations [33] show that the BN NT bundles can undergo unique phase transitions under trans- verse pressure. The influence of this pressure on the band structure of *zz*-SW BN (16,0) NT bundles (with initial diameter 1.26 nm of individual shells) was analyzed via the results obtained using DFT-LCAO calculations [32]. The rate of the gradually increasing pressure was chosen to be lower for lower pressures, in order to define the structural behavior prior to a transition taking place (Fig. 6.17). After each pressure increment, the bundle was let to attain equilibrium, and then the change in cell vol- ume was measured. No apparent systematic deviation from the circular cross section was observed below 1 GPa. Beyond this pressure, the BN NT cross section deform to an elliptic forms. Figure 6.17 clearly shows structural arrangements in nanotube bundle when pressure range is either low ($p < 1$ GPa) or high ($p > 1.0$ GPa).
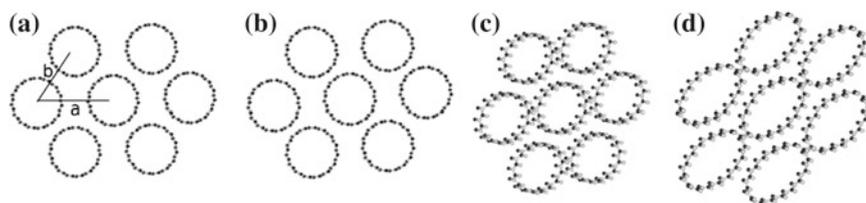
Fig. 6.17 Structure of a (16,0) SW BN NT bundle under the pressure of **a** 0 GPa, **b** 0.9 GPa, **c** 1.2 GPa, and **d** 3.5 GPa (Reprinted figure with permission from Guerini et al. [32], Copyright (2007) by the WILEY-VCH Verlag GmbH %26 Co. KGaA, Weinheim)

To quantify the volume changes occurring at the structural transition in BN NT bundles under the growth of pressure, the variations of magnitudes of UC vectors **a** and **b**, defining the hexagonal basal planes (the distances between the NT centers in the adjacent cells), were considered [32]. It was observed that by increasing the pressure, both vector magnitudes diminished and their decrease was not monotonous. The first vector magnitude is discontinuous and the second one changes the slope in its dependence on pressure, both occurring at $p = 1$ GPa.

The electronic band structure was observed to change rather little with the pressure (Fig. 6.18a–d). One significant change observed at higher pressures was the splitting of the degenerated states in the conduction band bottom. The energy gap at the Γ
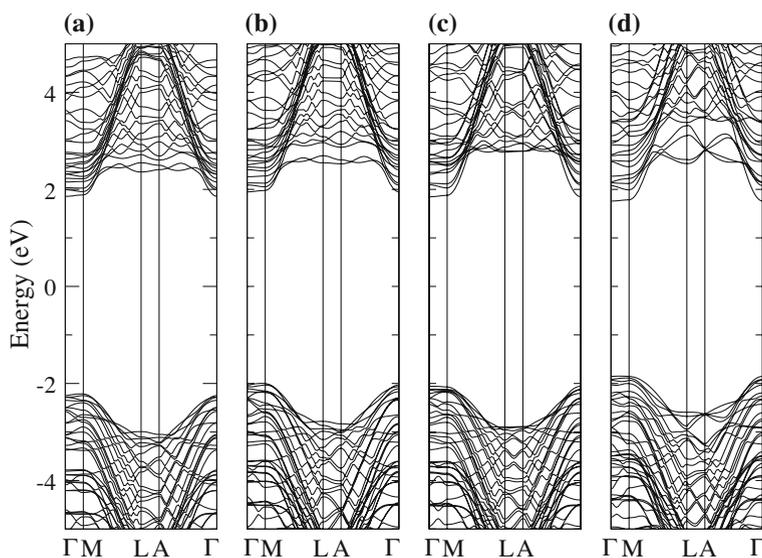
Fig. 6.18 Band structure of a (16,0) zigzag BNNTs bundle under pressure of **a** 0 GPa, **b** 0.9 GPa, **c** 1.2 GPa and **d** 3.5 GPa. The Fermi level localized in zero. The irreducible part of the hexagonal BZ for BN NT bundle is the same as for SiC NT bundle (Sect. 5.5.2) (Reprinted figure with permission from Guerini et al. [32], Copyright (2007) by the WILEY-VCH Verlag GmbH %26 Co. KGaA, Weinheim)

point was observed to diminish considerably with pressure. The value 4.10 eV at $p = 0$ decreased down to 3.61 eV at $p = 3.5$ GPa, although the system remaining a semiconductor at all the pressures considered.

A possible explanation for the different band gap dependence on the pressure in BN NT bundles (as compared to a bulk crystal) was provided as following [32]: (i) by applying the pressure to crystal, the elastic deformation is minute in most cases, due to its rigidity, whereas influence of pressure on bundles of single-wall NTs is rather different, due to their tubular geometry; (ii) although a nanotube is extremely rigid to distortions along the NT axis, it is very flexible to those, perpendicular to the axis, thus, the NT circular cross section may be deformed to an elliptical form; (iii) the instability of the NT cross section under pressure leads to deformations that cause the band gap to diminish in general. According to this idea, a transverse electric field was observed to severely reduce the band gap of a BN NT bundle [70].

6.2.5 Rolled-Up Double-Wall Nanotubes

Alternative ensembles constructed from SW BN NTs of different diameters, reproducibly synthesized and visualized, were found to be multi-wall boron nitride nanotubes with the inter-shell distance of 0.33–0.34 nm [69, 71]. Unlike CNTs, which exhibit rather random chiralities in MW NTs or bundles of SW nanotubes, a strong chirality selection (mainly zz-type) is observed in MW BN NTs [44]. The efficient plasma-arc method of BN NT synthesis was elaborated, which provided the production of almost exclusively double-wall nanotubes in high yield [72]. Moreover, while SW BN NTs of different chiralities with small and middle diameters should naturally undergo out-of-plane buckling, producing a dipolar shell as mentioned above (Fig. 6.6), the DW NTs may help to stabilize the growth of smooth nanotubes (containing mainly the even number of shells) [8]. Large-scale first-principles simulations on DW boron nitride nanotubes were performed earlier either for only $(n_1,0)@(n_2,0)$ chirality [22, 31] or for both $(n_1,0)@(n_2,0)$ and $(n_1,n_1)@(n_2,n_2)$ chiralities [28, 42].

The two mutual orientations of chiral and translational vectors of the constituent BN shells (Fig. 6.19) were considered for simulations of DW BN NTs [42]: coinciding and opposite (i.e., straight and inversed NT structures, respectively, corresponding to both PPB and APPB combinations of B-N bonds considered for SW BN NT bundles, Fig. 6.16). For ac-chirality of DW NTs, the cross-sections of inner and outer shells contain pairs of B and N atoms (B-N bonds) in the corresponding rings with both straight and inversed orientations of the chiral vector (Fig. 6.19a, b respectively), which make each of those electrostatically neutral. The difference of energies for equilibrium configurations of ac-DW BN NTs with the same chirality indices and straight versus inversed orientations of chiral vectors were found negligible, thus, only a-configurations were calculated. For zz-chirality, both straightly-stacked configuration, i.e., the outer B(N) ring across the inner B(N) ring (Fig. 6.19c), and the inversely-stacked configuration, i.e., N(B) across B(N) (Fig. 6.19d) were calculated because the corresponding energy difference between them is noticeable [42]. From

(a) model of straightly-stacked double-wall (5,5)@(10,10) *ac*-BN NT;

(b) model of inversely-stacked double-wall (5,5)@(10,10) *ac*-BN NT;

(c) model of straightly-stacked double-wall (9,0)@(18,0) *zz*-BN NT;

(d) model of inversely-stacked double-wall (9,0)@(18,0) *zz*-BN NT.

● B   ○ B (behind section)   ● N   ● N (behind section)
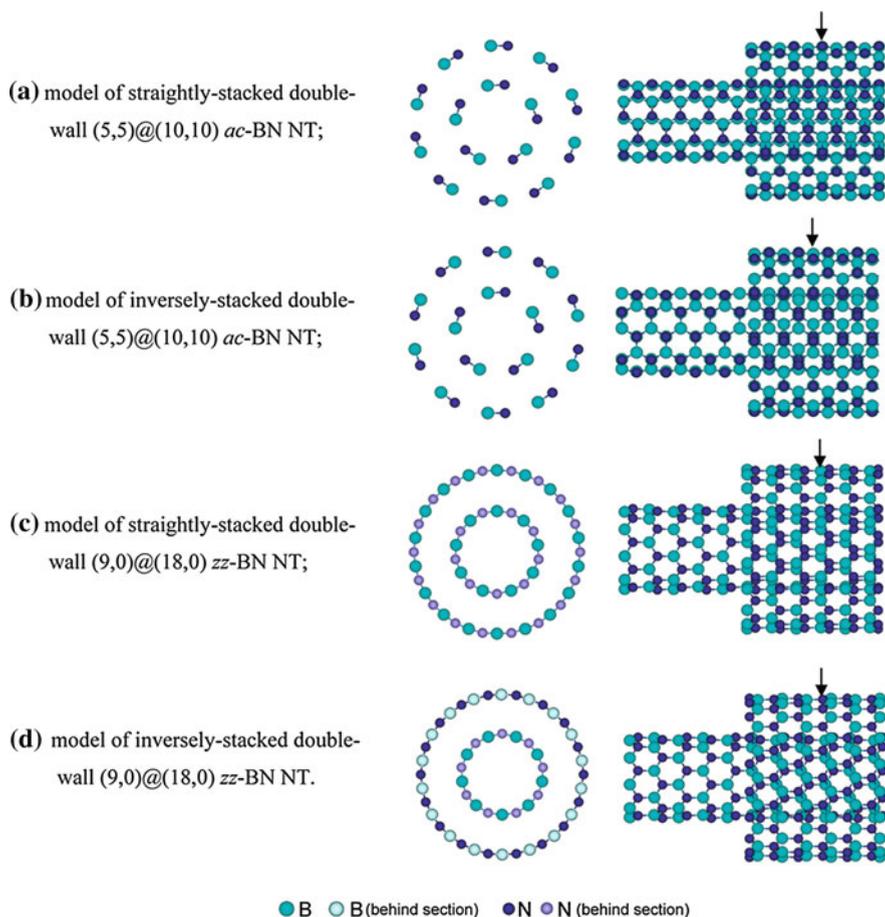
Fig. 6.19 Cross sections and lateral images for *ac*- and *zz*-chiralities of DW BN NTs corresponding to their optimized configurations. For *zz*-DW BN NTs (**c** and **d**), the atoms of the nearest ring behind the cross section are shown as *half-shaded balls*. Arrows above each lateral image of nanotube show directions of the cross sections. For convenience of visualization, lateral images of the inner shells of nanotubes have been chosen as twice as long as those of the outer shells [42]

the electrostatic point of view, the inversely-stacked configuration of *zz*-DW NTs should be energetically more favorable (i.e., positively-charged B ring of one shell is the nearest neighbor to the negatively charged N ring of the other shell, although in-wall B-N interactions are certainly more strong than those between the walls). A similar conclusion was earlier drawn elsewhere [28].

The stability of the DW NTs depends mainly on the inter-wall distance, i.e., a difference between the radii of constituent shells (ΔR_{NT}), and the diameter of the inner shell (D_{NT}^{in}). The binding energy E_{bind} between the constituent shells of a double-wall nanotube was chosen as a criterion of nanotube stability [42]:

$$-E_{bind}(D_{NT}^{in}@D_{NT}^{out}) = E_{tot}(D_{NT}^{in}@D_{NT}^{out}) - E_{tot}(D_{NT}^{in}) - E_{tot}(D_{NT}^{out}), \quad (6.3)$$

where E_{tot} are the calculated total energies of DW NTs and their constituent SW shells (both inner and outer) with the optimized structure. The energy curves $-E_{bind}(\Delta R_{NT})$ for DW BN nanotubes of both *ac-* and *zz-*chiralities are shown in Fig. 6.20 [42]. The maxima of binding energies for these double-wall nanotubes correspond to both optimal (5,5)@(10,10) and (9,0)@(18,0) configurations as well as inter-shell distance 3.5–3.6 Å (*cf.* (5,5)@(10,10), (8,0)@(16,0) and 3.2 Å as described elsewhere [28]). The inversed B-N configuration of *zz-*DW NTs is slightly more energetically favorable than that of the straight B-B one, which confirms the presence of polarization effects in boron nitride MW NTs. Reliefs of the binding energy curves (Fig. 6.20) also give a small preference to the inversed double-wall *zz-*NTs versus *ac-*NTs. These results also favor to the experimentally observed dipolar-shell structured morphology of the MW BN NTs [8]. Obviously, the small values of ΔR_{NT} and D_{NT}^{in} accompanied by the large values of relaxation energy result in instability of DW NTs (Fig. 6.20) while the large values of ΔR_{NT} and D_{NT}^{in} (as well as neglecting relaxation energies) correspond to the quasi-independent non-interacting pairs of SW NTs. On the other hand, E_{bind} is sensitive to ΔR_{NT} while the influence of D_{NT}^{in} on E_{bind} is rather negligible [42]. Fig. 6.21 shows the difference of the electronic charge re-distributions drawn for both optimal and increased values of ΔR_{NT} and D_{NT}^{in} for double-wall *ac-* and *zz-*BW NTs (Fig. 6.19). For the optimal structures of DW NTs, considerable re-distributions of the electronic density can be observed with clearly visible polarization effects, especially around the inner shells. The latter are the largest for the inversely-stacked configuration of *zz-*BN nanotubes, while $\Delta\rho(\mathbf{r})$ function for *ac-*BN NTs is characterized by a more pronounced localization effects [42]. For double-wall nanotubes with large inter-wall distances (Fig. 6.21b, d and f),
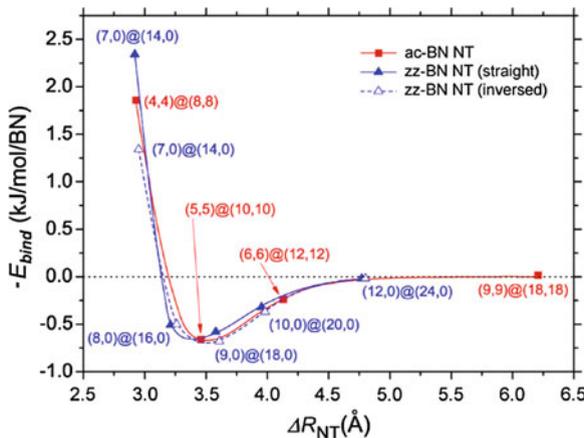
Fig. 6.20 Binding energies E_{bind} versus ΔR_{NT} for the three sets of DW BN NTs with *ac-* and *zz-*chiralities (Fig. 6.19). Spline treatment of *curves* has been performed to make them smooth [42]

Fig. 6.21 Difference
electron density plots $\Delta\rho(\boldsymbol{r})$
(the total electron densities
in the perfect DW BN
nanotube minus the sum of
these densities in the two
constituent SW BN NTs)
calculated for the
cross-sections of nanotubes
depicted in Fig. 6.19:
a (5,5)@(10,10),
b (9,9)@(18,18), **c** straight
(9,0)@(18,0), **d** straight
(12,0)@(24,0), **e** inversed
(9,0)@(18,0), **f** inversed
(12,0)@(24,0). *Solid* (*red*),
dashed (*blue*) and
dot-dashed (*black*) isolines
describe positive, negative
and zero values of the
difference density,
respectively [42]
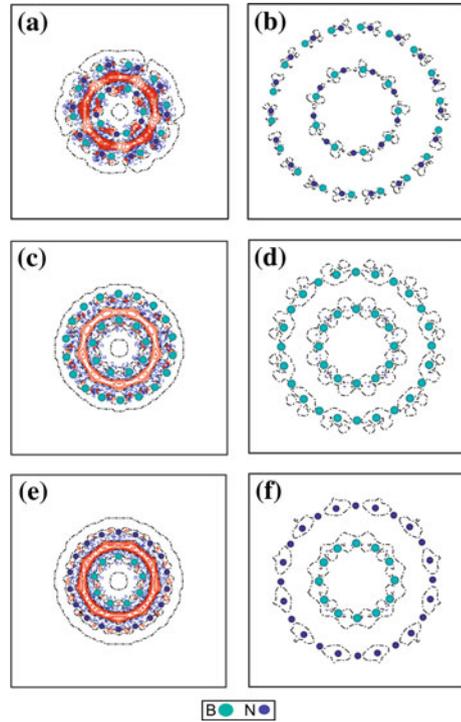
the interaction between the outer and inner shells is very weak, which reduces the stability of DW BN NTs, according to the reliefs of the potential curves (Fig. 6.20). The Mulliken charge population parameters calculated for both chiralities of the optimal and quasi-independent DW BN nanotube structures qualitatively confirm the results extracted from the drawn electron density re-distributions (Fig. 6.21).

For DW BN NTs, the band gap is the most dependent on the diameter of the inner shell being almost insensitive on the inter-shell distance. When comparing the calculated values of $\Delta\epsilon_{gap}$ for DW NTs with those for SW NTs, one can conclude that $\Delta\epsilon_{gap} < 6$ eV for chiralities (4,4), (6,0)–(10,0) of the inner shells, which correspond to $D_{NT}^{in} < 7.5$ Å. With the further increase of D_{NT}^{in} and ΔR_{NT} the value of the band gap gradually approaches to the limit of a BN(0001) monolayer (7.09 eV) On the other hand, the comparison of gap for SW and DW BN NTs with the same outer diameter D_{NT}^{out} shows that the band gaps of the latter are noticeably smaller, by 0.5–1.5 eV (depending on a diameter of the inner shell) [42]. Thus, the band gaps for multi-wall BN NTs can be easier adjusted by the morphology composition of inner walls. For both BN(0001) nanolayer and BN NT morphologies, one-electron N(2p) states prevail near the top of the valence band while the B(2p) states are mainly distributed near the bottom of the conduction band [42]. Owing to a large curvature of the BN NTs of small and middle diameters which induces the hybridization between σ and π states

of both shells, the top of the valence and the bottom of the conduction bands were found to be localized on the outer and inner nanotubes, respectively [22]. Simulations of triple-wall (TW) (5,0)@(13,0)@(21,0) BN NTs [37] mainly confirmed the main conclusions drawn for DW BN NTs. An additional interest attracted theoretical study of structurally compatible DW hetero-nanotubes (CNT@BNNT and BNNT@CNT) with different sizes and combinations of chiralities which possess a number of technological applications [34]. It was found that the features of the highest occupied energy levels and the low-lying conduction bands are mainly determined by CNTs. But when the inter-tube spacing was small, these bands could be modified significantly due to an increased inter-tube interaction. In general, the valence band top and the conduction band bottom consist of mainly $C(2p)$ atomic orbital, regardless of whether the CNT is the outer or the inner tube of a DW NT hetero-structure. When the inter-tube spacing was small, $N(2p)$ electrons also contributed to the bands near the Fermi level because of the coupling between both shells in the double-wall hetero-structure.

6.3 Boron Nitride Nanoscrolls and Nanowires

6.3.1 Nanoscrolls

Although 1D carbon nanoscroll structures (CNScs) were known for more than half a century [73], their systematic experimental studies were begun after the reproducible synthesis of graphene [74, 75]. While CNTs could be imaged as graphene monolayers rolled-up in a way that their ends meet forming a cylinder, the rolled-up graphene monolayers in CNScs form papyrus-like nanoscroll structures (Fig. 6.22). In contrast
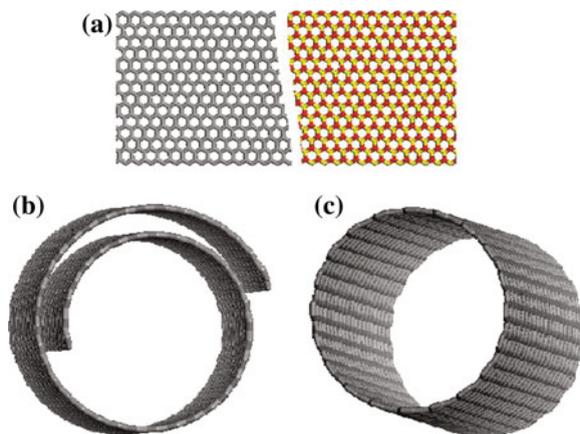
Fig. 6.22 Images of graphene/boronitrene monolayers (**a**), nanoscrolls (**b**) and nanotubes (**c**) (Reprinted figure with permission from Perim and Galvão [16], Copyright (2009) by the IOP Publishing)

to CNTs, nanoscroll diameter could be easily varied (contraction or expansion), making them extremely radially flexible. The self-scrolled tubules possess similar and even more remarkable properties than the planar graphene monolayers [76] and cylindrical CNTs [77] with potential applications in chemical doping, hydrogen storage, Li-battery technology and nano-mechanical devices [75].

Due to the similarity of honeycomb structures of both graphene and boronitrene (0001) monolayers, the morphologies of CNSs and BN NSs could be analogical (Fig. 6.22). However, in spite of a substantial number of theoretical and experimental works reported on BN NTs, as mentioned above, the reference data on BN NSs explored so far is rather scarce [16, 77]. The formation and existence of 1D nanoscrolls was also predicted for other inorganic materials, e.g., GeSi (Sect. 5.5.5). BN nanoscroll structures, simulated using the MD method, were generated by rolling a boronitrene monolayer into a truncated Archimedean-type spiral via rotation around the y' axis defined by the angle θ shown in Fig. 6.23a. This spiral is defined using the parametric equation [16]:

$$r = a\varphi + a_o, \tag{6.4}$$

where r and φ are standard cylindrical coordinates connected by non-zero constants a and a_o. The parameter a is related to the initial interlayer spacing d, i.e., $a = d/2\pi$.
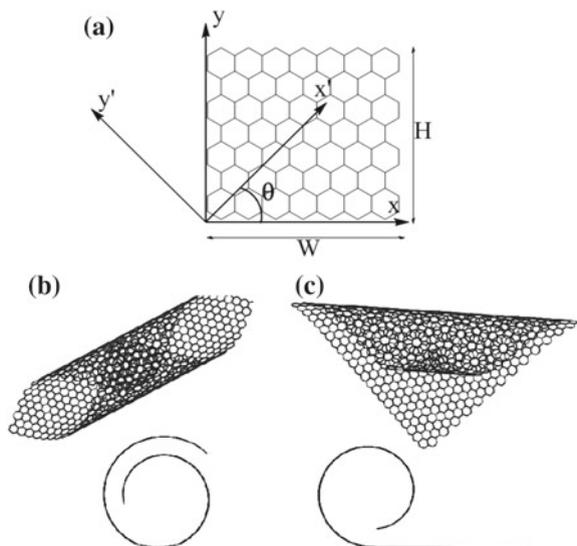
Fig. 6.23 The unwrapped honeycomb monolayer described by width W and height H where x' and y' are the scroll axes rotated by the angle θ relatively to the reference coordinate xy system (**a**). The scroll is generated by wrapping the monolayer around the y' axis. Examples of α- and β-type nanoscrolls with $\theta = 45°$ as well as their cross-sections are shown (**b** and **c**, respectively) (Reprinted figure with permission from Perim and Galvão [16], Copyright (2009) by the IOP Publishing)

Archimedean-type spirals describe well the scroll structures since they have a constant separation distance for successive turns of the spirals. While multilayer BN NScs are likely to exist, only monolayer scrolls have been considered so far [16]. The angle θ defines the scroll configuration: zigzag for $\theta = 0$, armchair for $\theta = 90°$ and chiral for $0 < \theta < 90°$. The analysis of the structural evolution during the scroll formation was restricted by two types: α (Fig. 6.23b), with no uncurled regions of the layer, and β (Fig. 6.23c), where flat and uncurled regions co-exist simultaneously. Although there are numerous other possible initial nanoscroll structures, the basic structural features can be addressed using these two structural types only as demonstrated for the CNSc case [78]. Both α- and β-BN nanoscrolls of different sizes were obtained by varying H and W values (Fig. 6.23a).

The formation of BN nanoscrolls is dominated by two major energy contributions (Fig. 6.24): an elastic energy increase caused by bending the BN layer (decreasing stability) and a free energy decrease generated by the van der Waals interaction energy of overlapping regions of the layer (increasing stability) [16]. As the structure is rolled up, the layer curvature increases before the layer overlap and so does the torsion and inversion contributions to the strain energy. Thus, the rolled nanostructure becomes less stable in relation to the undistorted (planar) configuration, which makes energy-assisted the transition from planar to rolled structures. If no external energy is provided, the curved structures will return to the more stable planar configurations. When the surfaces are overlapping, the van der Waals contributions increase the structural stability. This process can be better visualized by analyzing the van der Waals and bending energy contributions separately (Fig. 6.24b). For small nanoscroll diameters, the bending contributions outweigh the van der Waals energetic gains, thus, the structure becomes unstable and tends to evolve into planar structures [16]. There is a critical minimum of the inner diameter necessary to attain the structural stability of a nanoscroll. Beyond this limit, the rolling process would evolve spontaneously and the final structure can be even more stable than its parent planar
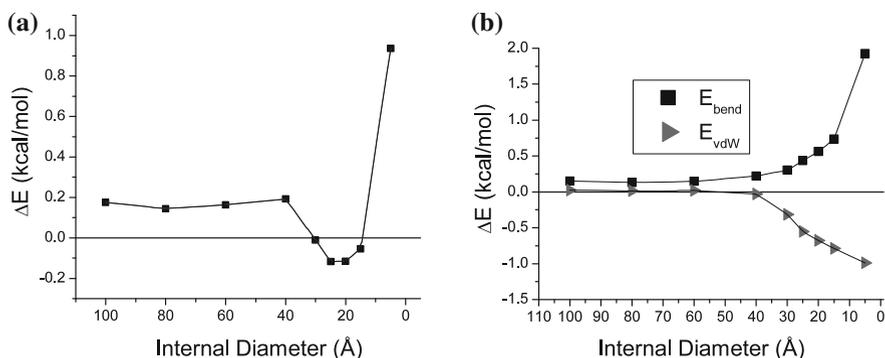
Fig. 6.24 Change in relative total energy (ΔE) during the wrapping of the plane BN monolayer into BN NSc (**a**). Contributions of bending and van der Waals terms to the total ΔE (**b**) (Reprinted figure with permission from Perim and Galvão [16], Copyright (2009) by the IOP Publishing)

configuration. For the case displayed in Fig. 6.24a, this occurs for diameters between 13 and 30 Å. Although these critical values are size- and chirality-dependent, the general behavior displayed in Fig. 6.24 is valid for all types of BN NSc structures. The armchair-type BN nanoscrolls were found to be the most stable configuration, while *zz*-NScs belong to metastable structures that can be thermally converted into armchair scrolls [16]. Chiral nanoscrolls are usually unstable and tend to evolve into *ac*- or *zz*-NScs depending on their initial geometries. Similar to the experimentally observed conically-shaped CNScs [79], BN NScs are also likely to be found in these configurations, according to performed MD simulations. The first successful synthesis route to boron nitride nanoscrolls has been reported quite recently [75].

6.3.2 Prismatic Nanowires

A number of solid substances that possess both anisotropic (e.g., layered) and isotropic crystalline modifications determine their potential capacity to form both NT and NW types of 1D structures [80, 81], as well as the possibility of phase transitions in nanosized forms of these substances. For example, 1D carbon nano-allotropes comprising graphite-like sp^2-bonded nanotubes and diamond-like sp^3-bonded nanowires, can mutually transform to each other ($sp^2 \leftrightarrow sp^3$) under certain conditions. In particular, the experimental method was elaborated for obtaining sp^3 hybridized diamond NWs from multi-wall sp^2 CNTs [82]. On the other hand, since the surface of diamond-like nanowire (characterized by d_{NW} diameter) is partially graphitized, it can be described as mixed $(sp^2)_x + (sp^3)_{1-x}$ 1D carbon nano-allotrope where x is proportional to $(1/d_{NW})^2$ [83]. Similar to carbon, crystalline boron nitride, as described above, can exist in two main modifications: graphitic sp^2-hexagonal (Fig. 6.1a) and diamond-like sp^3-cubic (zinc-blende) (Fig. 6.2). The phase transition $h - BN \rightarrow c - BN$ occurs at T $\sim$ 3,000 K and $p \geq 8$ GPa [84]. Comprehensively studied BN NTs were considered in detail in Sect. 6.2. They weakly depend on the atomic structure of the walls (chirality) and the size of the nanotubes, which is an attractive factor for their use in numerous technological applications. However, experimental data on the alternative group of 1D nanostructures, i.e., monolithic BN NWs, were found to be rather scarce. These nanowires consisted of different phases: (i) a hexagonal structure in the form of a rope of vertically oriented cones rolled of boronitrene nets and embedded in one another [85], (ii) a mixed hexagonal and zinc-blende structure of nanofibres obtained from B-N-O precursor and graphite powder [86], (iii) a turbostratic structure produced from BI$_3$ [87], (iv) an orthorhombic structure synthesized in a hydrothermal route from the solution of H$_3$BO$_3$ in the presence of N$_2$H$_4$ H$_2$O and C$_3$H$_9$N microdoses incorporated inside a stainless steel autoclave [88]. Moreover, the isolation of BN nanowires in a "pure form" for the subsequent investigations was found to be a complicated problem since they were obtained, as a rule, in a mixture with other BN nanostructures (nanotubes, nanoplates, nanocrystallites, fullerenes, etc.) [89].

Similar to diamond nanowires, theoretical studies on BN NWs were performed based mainly on their densely-packed *c*-BN structure [83]. The structural, electronic

and thermal properties of BN nanowires with optimized zinc-blende morphology were carefully simulated using the DFTB and MD methods [81]. The homogeneous BN NWs represented infinitely extended 1D prismatic crystallites cut from c-BN crystal perpendicular to the (001), (111), and (110) section planes, called as NW types I, II, and III, respectively (Fig. 6.25). It was necessary to analyze the dependence of nanowires' stability and properties on their morphology [81]. For example, the properties of nanowires depend on the polarity of their side facets: nonpolar (equal numbers of B and N atoms per surface unit) and polar (either boron or nitrogen atoms form the external surface layers). As to the analysis of dependence of NWs properties on their size, the areas of the cross sections S_{NW} used as the dimensional NW parameter were varied in the range of 20–500 Å^2.

Being dependent on the NW thickness (S_{NW}) and morphology, nanowires of I-III types were found to be different from the point of view of their structural stability and phase transformation [81]. For small nanowires ($S_{NW} < 100\,\text{Å}^2$) of types I and II, the cubic structure was observed to be unstable, with a partial NW transition
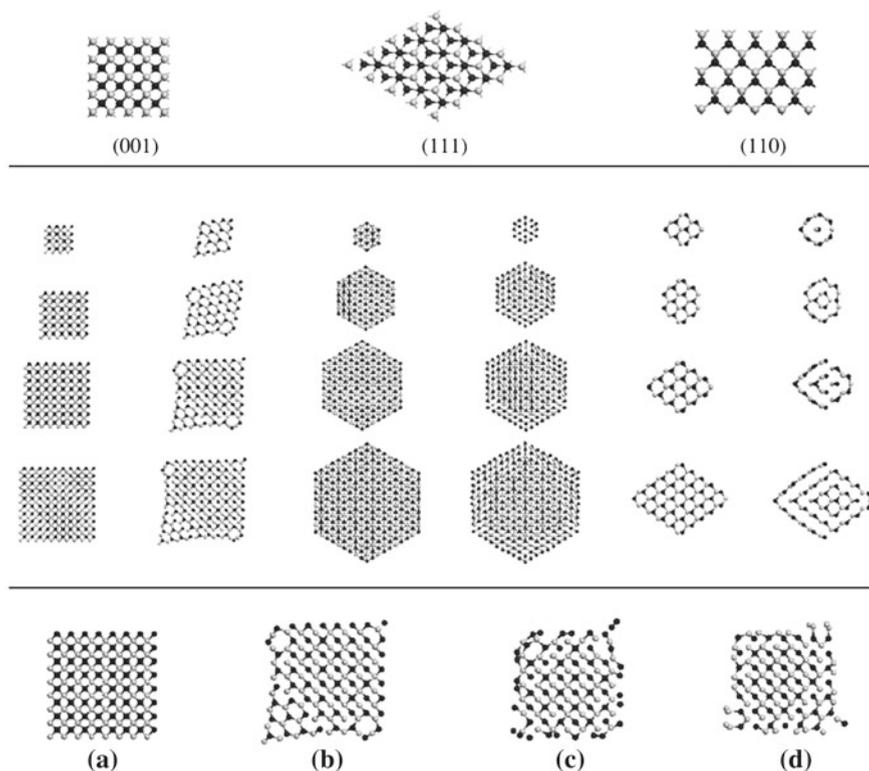
Fig. 6.25 *Top* panel: initial atomic structures of c-BN crystal in the directions of which nanowires of different diameters were cut: [001], type I; [111], type II; and [110], type III. *Bottom* panel: atomic structures of initial (*on the left*) and optimized (*on the right*) BN NW cross-sections [81]

to h-BN structure. Atomic rearrangements in relaxed c-BN NWs of type II (with $S_{NW} > 100\,\text{Å}^2$) resulted in the appearance of two-phase structures, with the outer layers transformed to a hexagonal structure, while the core of c-BN NW remained unchanged. Hence, one could speak about the formation of "hybrid" $(sp^2 + sp^3)$ BN nanowires combining hexagonal and zinc-blende structural types. The formation of two-phase systems was also observed in the case of type I nanowires: they partially segregated with the retention of the cubic structure inside the NW core. Similar graphitization effects were also observed in the cases of reconstruction in both c-BN surface layers [90] and thin c-BN films [91]. For type III BN NWs, the cubic structure proved to be unstable during the optimization procedure in the entire range of their sizes and transformed to the hexagonal one with the foliation of the monolithic nanowire into h-BN fragments (Fig. 6.25). For the thinnest nanowires of this type $(S_{NW} < 10\text{--}15\,\text{Å}^2)$, the energy stabilization occurred due to their transformations to hollow nanotubes with a hexagonal structure [81].

In general, the effect of the atomic rearrangement in the outer layers of BN NWs can be correlated with the lower energy stability of c-BN phase as compared with h-BN: the cohesion energy for h-BN was estimated to be 0.06 eV/atom higher than for c-BN [91]. According to the experimental observation, BN NWs were characterized by the simultaneous presence of sp^2 and sp^3 states [86]. The above described structural rearrangements in BN nanowires were also depended on (i) the type of NW facets (nonpolar or polar) and (ii) the number of dangling bonds per atom upon NW facets [81]. As a result of $sp^2 \rightarrow sp^3$ structural transformations in BN NWs, the interatomic bond lengths l_{B-N} changed noticeably, qualitatively correlating with the change in the coordination numbers of atoms, which equal 3 for the sp^2-bonded hexagonal structure and 4 for the sp^3-bonded cubic structure. Thus, for the thinnest nanowires, their average coordination numbers are noticeably less than three due to the presence of a significant number of surface atoms with dangling bonds. For the bulkiest nanowires, on the contrary, the average coordination numbers (CNs) exceed three, reflecting the presence of sp^3 atoms with $CN = 4$ inside the NW core. With the increasing size and CNs of nanowires the bond lengths l_{B-N} also increased, from 1.43 to 1.55 Å in accordance with the well-known tendency of l_{B-N} growth in boron-nitrogen systems with different atomic coordination in the following sequence: the BN molecule ($CN = 1$, $l_{B-N} = 1.28\,\text{Å}$) $\rightarrow$ the linear chain -B-N-B-N- ($CN = 2$, $l_{B-N} = 1.30\,\text{Å}$) $\rightarrow$ h-BN crystal ($CN = 3$, $l_{B-N} = 1.45\,\text{Å}$) $\rightarrow$ c-BN crystal ($CN = 4$, $l_{B-N} = 1.57\,\text{Å}$) [92]. Figure 6.26 presents the dependence of the calculated total energies for the optimized structures of BN NWs on the areas of their cross-sections [81]. It reveals that the stability of nanowires markedly increased with the growth of their diameters when the energy of the corresponding NWs approached the value of E_{tot} for the crystalline c-BN phase. At comparable values of S_{NW}, the BN nanowires of type III were found to be the most stable in the total energy (although structurally they were rather unstable, as discussed above), while NWs of type I showed the smallest stability. Obviously, the most stable BN NW configuration is type II.

Fig. 6.26 Total energy
E_{tot}, eV/atom of BN NWs
versus their cross-section
area S_{NW}. Nanowire types
are described by the labels:
square [001] (type I), triangle
[111] (type II) and circle
[110] (type III). The *dashed
line* corresponds to the total
energy of *c*-BN bulk [81]
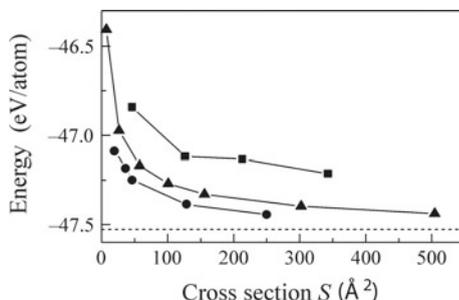
This assumption was confirmed after performing MD simulations of all three BN
NW types (Fig. 6.27) [81]. Losing their monolithic nature at already $T = 0$ K (bottom
of the right panel in Fig. 6.25), the nanowires of type III became so distorted with
the increasing temperature that they transformed to quasi-tubular structures (right
panel of Fig. 6.27c, d). As the temperature increased, beginning with $T = 300$ K, all
the type I nanowires underwent progressing thermal deformations associated, first,
with the transition of the cubic structure of the "core" to the hexagonal structure;
next, with their "transversal" foliation; and, starting with T ~1,000 K, the thermal
decomposition of nanowires occur with the formation of *h*-BN layers and separate
BN groups (as T increased up to 1,500 K). Meanwhile, BN NWs of type II proved to
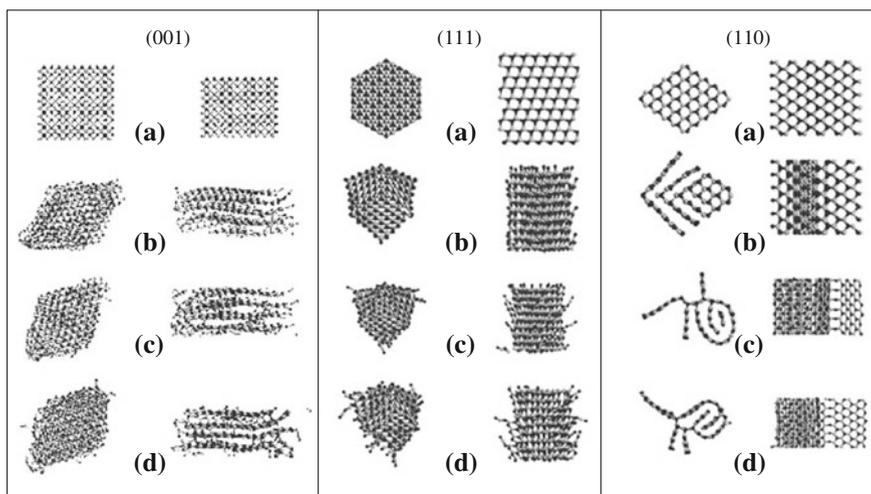
Fig. 6.27 Thermal distortions of BN NWs (types I, II, and III, as presented in Fig. 6.25) at various
temperatures. Atomic structures of NW cross and longitudinal sections were shown (*left* and *right*
panels in each column, respectively) are shown: (**a**) initial (*non-optimized*) atomic models and those
after MD simulations at $T = 300$, 1,000, and 1,500 K (**b**, **c**, and **d**, respectively) [81]

be the most thermodynamically stable under the thermal exposure, retaining the cubic structure of the "core" up to T $\sim$1,000 K [81]. The occurrence of B and N atoms of different coordination in the composition of each nanowire resulted in the fact that their electronic spectra (DOSs) represented a complex superposition of states corresponding to contributions of particular non-equivalent groups of atoms [81]. The width of the NW valence band ($\sim$9.0 eV) estimated using the DFTB method (Fig. 6.28) proved to be somewhat narrower than that for h-BN (10.4 eV) or c-BN (11.8 eV) crystals found earlier [93]. The band gap $\Delta\epsilon_{gap}$ also decreased, down to $\sim$3.0–3.4 eV (approximately, by half, as compared to bulk). According to Fig. 6.28, the highest occupied and the lowest unoccupied bands were formed by the states of atoms of the outer NW layer. For less stable BN nanowires, undergoing significant structural rearrangements and having a large number of atoms with dangling bonds, both a semiconducting type (where $\Delta\epsilon_{gap}$ decreased down to 1.8–0.9 eV), and even a metallic type (that is, with a non-zero density of states at the Fermi level), of DOS spectra were obtained (right and left panels of Fig. 6.28, respectively).

DFTB simulations performed [81] well demonstrated that BN nanowires represent unique hetero-phase 1D materials in which, depending on their size and morphology, various phase transformations can occur. Some "critical" size for each NW type exists, below which c-NWs cannot be formed at all. Unlike homogeneous diamond-like carbon nanowires, stable BN nanowires are always two-phase systems whose "shells" have hexagonal structures and the "core" has a cubic structure. They can exhibit both semiconducting and metallic properties, which attracts enhanced technological interest. Depending on the initial structure (e.g., direction of NW axis), BN nanowires, according to MD simulations, can undergo various types of thermal deformations [81]: from the rearrangement of c-BN structure of their "core" into h-BN one, up to the formation of pseudo-tubular or layered structures from hexagonal layers.
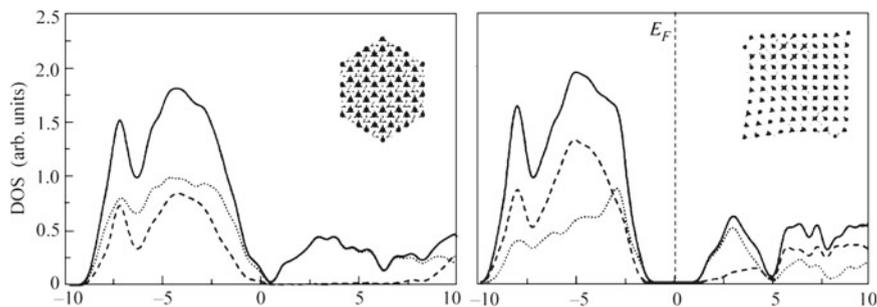
Fig. 6.28 Total densities of states (*solid lines*) of BN NWs of types I and II (at *right* and *left* panels, respectively); partial contributions of the surface (*dotted lines*) and inner (*dashed lines*) B and N atoms are given separately. The vertical line is the Fermi level ($\epsilon_F = 0$ eV) [81]

6.3.3 Monoatomic BN Linear Nanochains

Apart from prismatic-type BN nanowires with diameters varying in the range of 0.7–3.0 nm, as described above, theoretical simulations were performed also on BN nanofilaments of atomic diameters with the structure of linear chain -B-N-B-N-, which can be doped by different atoms (e.g., C and S) and functionalized [94–98]. Fragments of monoatomic BN filaments (they were called "nanowires" in aforementioned papers), which were found to be semiconducting (when using the first principles calculations), being joined to metallic electrodes (e.g., Al and Au) resulted in the appearance of the conductance along linear $(BN)_m$ chains [97, 98]. The electron transport properties of these junctions have potential applications in several components of the novel molecular electronic devices [98]. For simulations of pure BN nanochains (both terminated and infinite) and their finite fragments incorporated between electrodes, various ab initio methods were applied: (i) the standard HF-LCAO method and that combined with the Wannier-function-based formalism [95, 96], (ii) both DFT-LCAO and DFT-PW methods combined with formalism of non-equilibrium Green's function [94, 97, 98], and (iii) MD method provided for a large number of femtosecond time steps [94].

An isolated infinite monoatomic BN nanochain was found to possess a linear geometry exhibiting *sp*-type hybridization with 180° B-N-B (N-B-N) inter-bond angles since its different possible *zz*-structures led to higher total energies as compared to the linear chain (LC) [96]. It means that if the isolated BN chains could exist, they would have mainly a linear structure. A direct band gap $\Delta\epsilon_{gap}$ of monoatomic infinite BN LC (Fig. 6.29) was estimated to be 4.0 eV when using GGA-PW method with Green's function correction [94]. The other remarkable aspect of infinite BN LCs, as compared to C or Si nanochains (Sect. 5.3), is that it does not exhibit any alteration in bond populations and all the nearest boron and nitrogen atoms are equidistant. Any periodic BN structures, being hetero-nuclear in nature, have significant ionic contributions to the bonding as opposed to the purely covalent materials.

On the other hand, the charge distribution in a finite linear $(BN)_m$ nanochain terminated at the borders by B and N atoms cannot be periodically distributed along its axis. A sequence of one-electronic states is formed in this case around the energy gap corresponding to HOMOs (highest occupied molecular orbitals) and LUMOs (lowest unoccupied molecular orbitals) as shown in Fig. 6.30. These orbitals are

Fig. 6.29 Calculated energy band structure of infinite BN linear chain (LC) which bands are drawn for two-atom UC centered on B atom. Fermi level is shown by dot-dashed line [94]
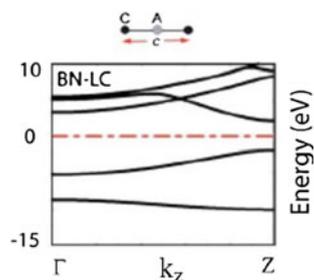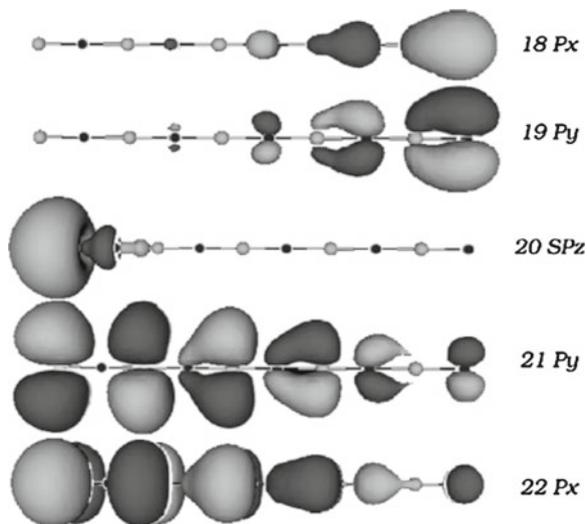
Fig. 6.30 HOMOs ($18\,p_x$, $19\,p_y$, and $20\,sp_z$) and LUMOs ($21\,p_y$ and $22\,p_x$) of linear (BN)$_5$ molecule oriented along z axis (Fig. 6.31) (Reprinted figure with permission from Shi et al. [97], Copyright (2006) by the American Chemical Society)

localized on either boron or nitrogen atoms, due to the difference of B and N ionicity [97]. The HOMOs are composed of degenerate (sp_z) and σ (p_x and p_y) orbitals, which are spatially localized to the left and to the right sides of a (BN)$_5$ molecule. The LUMOs are composed of two degenerate π (p_y and p_x) orbitals which are spatially delocalized in the proximity of the right side of molecule. The characteristics of molecular orbitals localized on both B and N atoms are important for understanding of conductivity in a finite linear BN chain sandwiched between two semi-infinite [001]-oriented Al nanowire electrodes (Fig. 6.31).
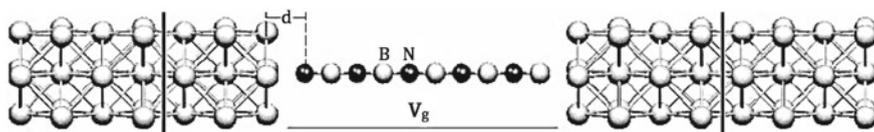
Fig. 6.31 1D model of BN LC coupled to [001]-oriented Al semi-nanowires (x and y directions were oriented perpendicular to the monoatomic BN chain fixed along z direction). 3D supercell with large vacuum gaps between nanowires in the x and y directions was chosen, which practically excluded the direct interaction of the original 1D system described as Al NW(l)-(BN)$_5$-Al NW(r) (as shown in the Figure) with its mirror images. The terminated B and N atoms were positioned symmetrically above the hollow sites of aside Al{001} facets (separated from them by distance d). The region within two black lines is the scattering region and the remaining parts are the *left* and *right* electrodes. Both NW-type Al electrodes extend to the half-infinity (in negative and positive directions). V_g determines the gate voltage [97]

Fig. 6.32 The total transmission spectrum (T_t) and its eigen-channel decompositions (T_1 and T_2) of (BN)$_5$ LC sandwiched between two Al(100) nanoscale electrodes (Fig. 6.31). Note that only two channels contribute to the total transmission and they are equal [97]
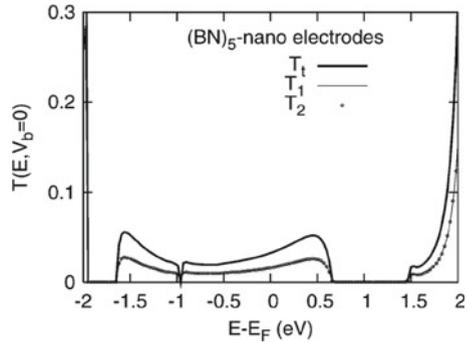
The transport properties of BN linear chain sandwiched between two Al(001) semi-nanowires are determined by the molecular orbitals of the former and the band structures of the latter as well as by their coupling, which can explain those, e.g., the so-called eigen-channels [99]. Figure 6.32 shows the total transmission spectrum (T_t) with its eigen-channel decompositions (T_1 and T_2) of the sandwiched nanostructure. The energy E is relative to the average Fermi level of the two-probe system, i.e., $(\mu_l + \mu_r)/2$, where μ_l and μ_r are electrochemical potentials for both the left and right semi-nanowires, respectively, while V_b is the external bias voltage. The maximum value of the total transmission of BN linear chain is 0.3, which is much smaller than that (2.0) of analogous 10-atom carbon linear chain [97]. The transmission energy regions (where $T(E) > 0$) and transmission energy intervals, i.e., $T(E) = 0$, are mainly determined by Al nanoscale electrodes.

It was suggested that the value of T energy is determined by the band structure of semi-nanowires and the momentum filtering effect of finite (BN)$_5$ chain which means that only those Bloch bands of the electrodes having the same orbital character as the molecular states (Fig. 6.30) near the Fermi level (π-orbitals) conduct well [99]. On the other hand, the transmission energy intervals seem to be insensitive to BN linear chains and are determined by the band gaps of the electrodes. However, when a molecule with mainly σ orbitals is placed near the Fermi energy of the electrodes, the energy intervals are sensitive to (BN)$_5$.

Figure 6.33 shows the current-voltage (I-V) curves of BN LC coupled to Al(100) NW electrodes. The current I was estimated within the Landauer-Büttiker formalism [97]:

$$I(V_b) = \frac{2e}{h} \int_{-\infty}^{\infty} [f_l(E - \mu_l) - f_r(E - \mu_r)]T(E, V_b)dE, \qquad (6.5)$$

where E, V_b, $T(E, V_b)$, μ_l and μ_r are described above, while f_l and f_r are the electron distribution functions of the left and right Al electrodes, respectively. It can be seen that the I-V curve is determined by both BN LC and Al(001) semi-nanowires (Fig. 6.31), while the NDR (negative differential resistance, which is characterized by

Fig. 6.33 The
I-V curves of BN
LC sandwiched between two
Al(001) semi-nanowires [97]
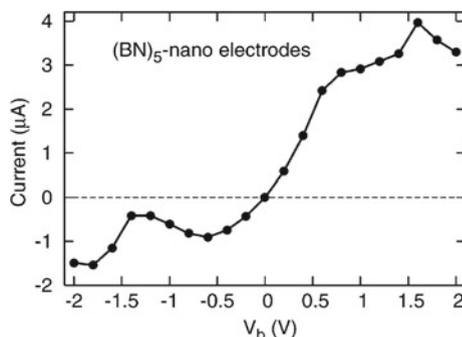
the decrease of the current with the increase of the external bias) is the phenomenon more apparent at V_b voltage intervals –(1.4–0.6) V and 1.6–2.0 V. The origin of NDR can be understood from the changes of coupling between linear (BN)$_5$ molecule and nanoscale Al electrodes at various external biases [97]. The *I-V* curves for BN LC were found to be asymmetric as a result of its asymmetric coupling with both Al(001) semi-nanowires (according to Fig. 6.31, on the left side, nitrogen atom is bound with the left nanoscale Al electrode, while the right electrode is bound with a boron atom).

Mechanical adjustment of the spacing between nanoscale electrodes (Fig. 6.31) resulted in the ability to shift the spacing between the energy levels in a (BN)$_5$ molecule using a gate electrode [100]. The transport properties of the 1D Al NW(l)-(BN)$_5$-Al NW(r) system can be tuned using (i) variation of a distance d between BN LC and arbitrary Al electrode as well as (ii) inclusion of a gate voltage (Fig. 6.31). As shown in Fig. 6.34a, the equilibrium conductance G (determined within the Landauer-Büttiker formalism in the framework of ballistic conduction mechanism as $G = \frac{2e^2}{h} \sum_n T_n$, where T_n is the transmission probability of the mode n [101]) decreases monotonically with the growth of separation d between BN LC and each of two Al electrodes.

Figure 6.34b shows the tuning of the transport behavior of BN LC through the inclusion of the gate voltage V_g. The gate voltage drastically increases the equilibrium conductance of (BN)$_5$, which can be understood from the shift and alignment of the molecular orbitals relative to the Fermi level of the electrodes. Here, the positive gate voltage means the downshift of the energy levels in BN LC [102]. With the increase of V_g, this LC continuously switches from a weakly to a highly conducting state, which indicates that it might be a good candidate for molecular switch [97].

Figure 6.34c shows both the charge transfer from the Al electrodes to BN LC with the increase of d, which decreases monotonically, and the projection of the density of states (PDOS) of the two-probe system onto all the basis orbitals of (BN)$_5$ molecule. These plots show that the equilibrium conductance G has a different variation behavior as that of PDOS since orbitals of BN LC are well localized (in contrast, for a linear C_{10} molecule, G has the same variation behavior as that of PDOS [97]).

Fig. 6.34 The equilibrium conductance G of $(BN)_5$ molecule as a function of d (**a**) and V_g (**b**) as well as the corresponding PDOS at the Fermi level and charge transfer from the electrode to BN LC (**c**) [97]
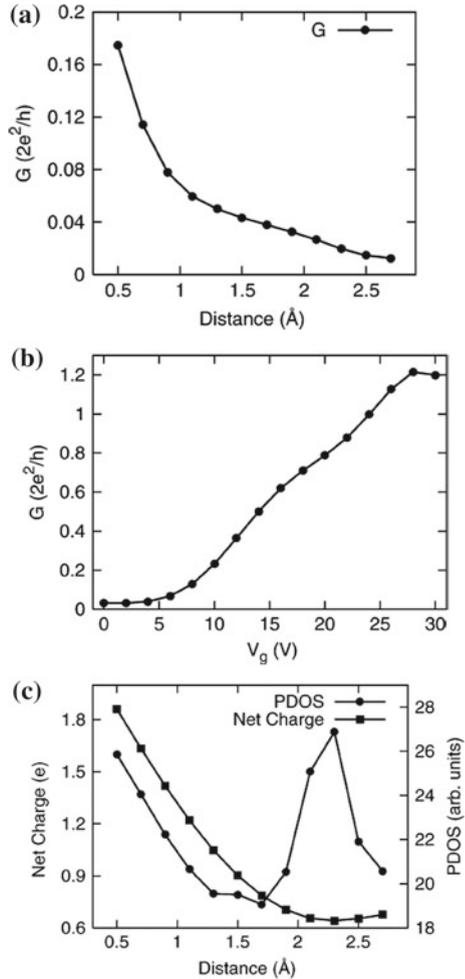
6.4 Group III Metal Nitride Bulk and Nanolayers

Among the sp^3-bonded group-III metal nitrides, AlN is the largest band gap semiconductor, which $\Delta\epsilon_g$ achieves 6.2 eV, characterized by a high temperature stability, considerable thermal conductivity, low thermal expansion, resistance to chemicals used in semiconductor processing, and reliable dielectric properties [103, 104]. Moreover, small lattice mismatch between AlN and GaN lattices makes possible a synthesis of hetero-structural $Al_xGa_{1-x}N$ alloys [105], which can be used in a number of technological applications, mainly in micro- and optoelectronics, e.g., laser diodes and "solar-blind" ultraviolet photodetectors [104]. Their performance can be noticeably improved by the regulation of extrinsic impurities and intrinsic point defects

inside the crystalline samples [106–108]. There are three possible 3D crystal morphologies shared by the group-III metal nitrides: wurtzite (*w*), zinc-blende, or sphalerite (*c*), and rock salt (*rs*) [109]. As to hexagonal graphitic-type *h*-BN morphology, it cannot be realized in the group-III metal nitrides since the appearance of in-plane sp^2 Al-N (Ga-N) bond hybridization is hardly possible, which can be illustrated by a substantially higher ionicity of the latter, where the transfer of charge towards N is 2.56 e (2.65 e) [105], whereas in sp^2-bonded *h*-BN, the analogical effective charge is only 1.01 e accompanied by substantial covalency [3]. This difference can be a reason for essentially larger bond lengths in the group-III metal nitrides as compared to BN: 1.86 Å (1.87 Å) versus 1.46 Å respectively [110]. AlN and GaN (similarly to SiC and GeSi as considered in Sect. 5.4) crystallize in a wurtzite-type structure (Fig. 6.35b) described by $P6_3mc$ space symmetry group. As to a zinc-blende structure ($F\bar{4}3m$ group) shown in Fig. 6.35a, it was found to be metastable for AlN, although *c*-GaN phase can be stabilized using an epitaxial growth of its thin films on the (001) planes of *fcc* structures like MgO [112]. The *rs*-structure ($Fm\bar{3}m$ group) can be achieved only at very high pressures in the group-III metal nitrides, thus, it was not usually considered at all. Numerous theoretical studies of *w*- and *c*-phases of the group-III metal nitrides [104, 109] clearly show that the latter are characterized by a noticeably smaller band gap (achieving several eV decimals). Moreover, both phases differ from each other in the stacking sequence along the [0001] direction in the wurtzite structure and [111] direction in the zinc-blende one (Fig. 6.35), which cross the most

Fig. 6.35 Zinc-blende (**a**) and wurtzite (**b**) structures of the III group metal nitrides (bulk UCs in the *top* panel as well as across images of (111) and (0001) slabs, respectively, in the *middle* panel versus atop images of slab UCs in the *bottom* panel). The *open* and *closed circles* represent metal and nitrogen atoms, respectively [111]
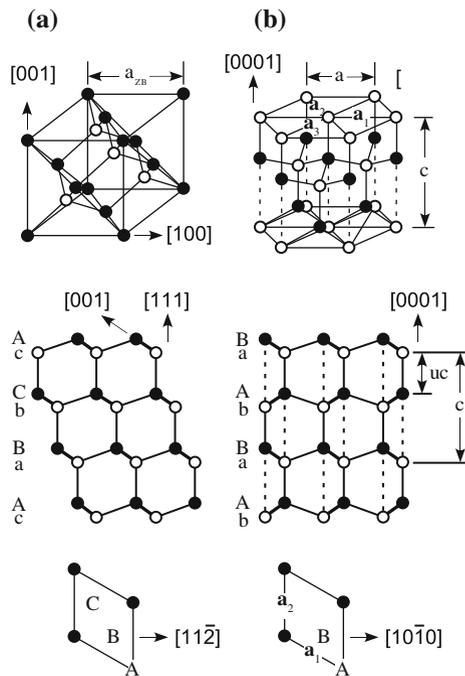
densely packed crystallographic faces of the group-III metal nitrides. The lattice constants a_{zb} (Fig. 6.35a) for c-AlN and c-GaN were found to be 4.38 and 4.50 Å, respectively [113]. The wurtzite lattice constants a and c (Fig. 6.35b) are connected via ratio $c/a = \sqrt{8/3} \approx 1.6333$ and supplemented by the dimensionless internal parameter $u = 3/8 = 0.375$, where uc corresponds to the length of the bonds parallel to the [0001] axis [111]. Additionally, the wurtzite lattice contains pairs of metal and nitrogen atoms, connected by dashed lines along the [0001] direction (Fig. 6.35b) and attracted to each other by the electrostatic forces, which reduce their lengths as compared to bulk crystal. The lattice constants of wurtzite-type AlN and GaN crystals were found to be 3.31 Å (a_{AlN}), 3.19 Å (a_{GaN}), 4.98 Å (c_{AlN}) and 5.19 Å (c_{GaN}) [113], thus confirming a small lattice mismatch between both crystalline materials.

2D plane structures of the group-III metal nitrides were studied mainly for the densely-packed polar surfaces of zinc-blende (111) (Fig. 6.35a) and wurtzite (0001) (Fig. 6.35b). The corresponding ultrathin slabs can be directly compared since the [111]-ordered zinc-blende and [0001]-ordered wurtzite structures have the same coordination up to the third nearest-neighbor shell and the interface geometry (in terms of the number and direction of bonds) is the same (*cf.* Fig. 6.35a, b) [114]. A common feature found for all polar surfaces is a strong tendency towards a metal-rich surface stoichiometry (Fig. 6.36) whereas N atoms are rather thermodynamically unstable on almost all equilibrium surfaces [115, 116]. Recent studies have demonstrated that in w-structures, the two kinds of surfaces are the most stable: (i) the so-called n-type (B), where the first interlayer is shown in the lower part of Fig. 6.36, (ii) the p-type (A), where the outer metal atoms are positioned directly above the sub-
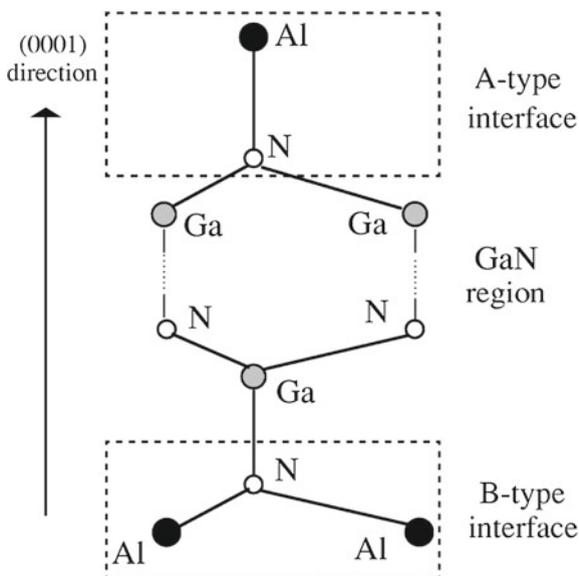
Fig. 6.36 Two types of w-Al/GaN(0001) interface (see explanation in the text) [114]

surface N atoms as shown in the upper part of Fig. 6.36. The *n*-type surfaces usually exhibit a smoother surface morphology leading to a higher material quality [115]. Moreover, if the *n*-type surface of group-III metal nitrides is characterized by a band gap, the width of which is 2–2.5 times smaller than that in bulk, the *p*-type surface possesses practically no noticeable gap between the conduction and valence bands since it is overlaps by the energy states of outer metal layer which is bound with subsurface layers weaker than in the case of *n*-type substrate. Similarly, the *n*-type (111) surface (the middle panel of Fig. 6.35a) is a more favorable for the zinc-blende polar substrate as compared to the *p*-type.

First principles full-potential linearized augmented plane wave (FLAPW) calculations were performed, in order to clarify the role of the interface geometry on piezoelectric fields and potential lineups in [0001] wurtzite and [111] zinc-blende Al/GaN junctions, which are structurally compatible [114], due to proximity of the corresponding lattice parameters of AlN and GaN surfaces. The electric field (its polarity and magnitude) was found to be strongly affected by atomic relaxations in the interface region. On the other hand the Schottky-barrier height (SBH) evaluated in the presence of electric fields [114] showed that their effect is relatively small (a few tenths of an eV). These calculations assess the rectifying behavior of the Al/GaN/Al contacts (Fig. 6.36), in agreement with the experimental values obtained for the SBH barrier [117]. Obviously, non-relaxed AlN (or GaN) bilayer cut from the densely-packed *n*-type slabs with either *c*-(111) or *w*-(0001) terminations (the middle panel of Fig. 6.35) practically coincide and form the buckled sp^3-bonded honeycomb nanolayers (Fig. 6.37), which atop images are the same hexagonal as a flat *h*-BN sp^2-bonded honeycomb nanolayer (Fig. 6.3). Moreover, their geometry optimization carried out using various first principles computational schemes resulted in either substantial decrease of buckling [108] or appearance of flat graphene-like nanolayers [119, 120], unlike buckled SiC and GeSi nanolayers considered in Sect. 5.4. However, unlike sp^2-bonded graphene-like AlN single-layer nanoribbons, a flat honeycomb AlN monolayer, which could be technologically important in optoelectronics and energy engineering, has not been fabricated so far, moreover, its mechanical stability is still unknown [120].

Fig. 6.37 Atop view of *n*-type densely-packed surfaces of the group-III metal nitride. N atoms are shown as *small black balls* [118]
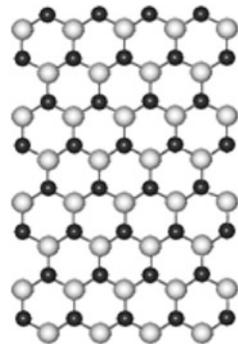
6.5 Group III Metal Nitride Nanotubes

6.5.1 Rolled-Up Single-Wall AlN Nanotubes

1D tubular nanostructures of the group-III metal nitrides attract enhanced attention in both experiments [121–124] and theoretical simulations [108, 110, 125–140], due to numerous technological applications, for instance, in optoelectronic devices working within both ultraviolet and visible light diapasons [135] as well as in alloy-type $Al_xGa_{1-x}N$ and hetero-structural AlN/GaN-based nanoelectronics [138, 140]. AlN NTs were synthesized experimentally using either direct current (DC) arc-plasma-induced melting of aluminum in N-Ar ambient [123, 124] or treating the aluminum powder, impregnated with cobalt sulfate in advance, with NH_3/N_2 ambient in a special tubular furnace [122]. Both types of NT samples, identified using the high-resolution transmission electron microscopy (HRTEM), were accompanied by nanoparticles and nanowires. The diameters of those nanotubes were found to be either small, 2–4 nm, or large, 20–80 nm, whereas the thickness of their walls was estimated to be from 1 up to 20 nm. For synthesis of GaN NTs, w-ZnO NWs were used as templates [121]. Unlike earlier synthesized SW BN NTs, well visualized with graphene-like network on the nanotube wall [10], no observations of analogous SW structures in AlN and GaN NTs have been reported so far.

Nevertheless, in majority of theoretical simulations on the group-III metal nitrides NTs just smooth or slightly buckled single-walled models have been used as the simplest presentation. They were mainly characterized by two equilibrium structures possessing either *ac*- or *zz*-type chiralities (Fig. 6.38), although chiral NTs were considered as well [139] alongside with a wide range of uniform diameters (0.5–6 nm). On the other hand, theoretical models of the crystalline-type sp^3-bonded AlN NTs observed experimentally (similar to those for SiC NT as considered in Sect. 5.4.4),

Fig. 6.38 Views of AlN SW NTs across their axes and along them for **a** armchair-type (5,5) and **b** zigzag-type (9,0) chiralities. N atoms are shown as *small black balls*. Cross-sections of both nanotubes contain values of their optimized radii (R) [127]
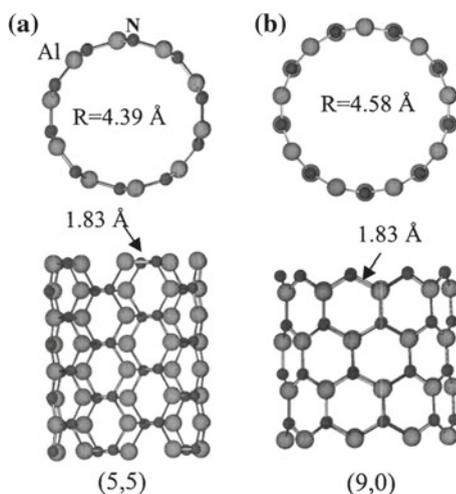
rather than cylindrical layered nanotubes, are needed [135]. For theoretical simulations on all these NT models, both finite cage-like tubules [126, 128, 129, 134] and infinite nanotubes [108, 110, 125, 127, 130–133, 135–140] were used. A wide spectrum of methods was applied in these calculations: atomistic formalism of many-body empirical potentials [110], methods of molecular dynamics [127, 129–131, 135], DFTB [125, 131], DFT-PW [125, 132, 133, 136, 138, 139], DFT-LCAO [108, 127, 130, 134, 135, 137, 140], as well as HF [126, 128]. Analogically to BN SW NTs (Fig. 6.6), a slight distortion was observed after DFT calculations in initially cylindrical honeycomb walls of AlN SW NTs, where Al atoms moved toward the axis of nanotube while N atoms were shifted in the opposite direction after relaxation, which resulted in nanotube buckling [127]. The radial buckling was found to be 0.037 and 0.035 Å for (5, 5) and (9, 0) nanotubes, respectively (Fig. 6.38). The buckling in AlN SW NTs was found to be the smallest as compared to those in BN [25] and GaN [125] SW nanotubes with similar diameters. The larger is R, the smaller will be the buckling, as shown in Fig. 6.6. For (10,10) AlN NT, the buckling was found to be only 0.018 Å. These results are correlated with a difference in hybridizations of Al and N on the curved hexagonal layer. All AlN NTs are semiconductors with band gaps ranging from 2.84 to 3.95 eV [127].

Models of *ac-* and *zz-*type AlN SW NTs with substantially larger diameter (∼6 nm) and, correspondingly, smaller structural stability were considered as (36, 36) nanotubes described by rod symmetry group $P6/m$ (Fig. 6.39a) and (64,0) NTs attributed to symmetry $P4mm$ (Fig. 6.39b), respectively [137]. It was shown that their
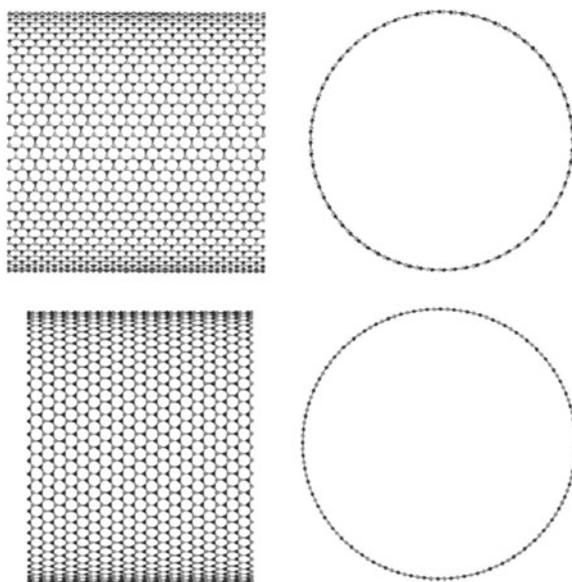
Fig. 6.39 Images of 6 nm thick AlN SW NTs along the axes of nanotubes and across them for **a** *ac-*type (36,36) and **b** *zz-*type (64,0) chiralities [137]

equilibrium bond lengths d_{Al-N}, binding energies *per* bond $E_{bind}(Al\text{-}N)$ and effective charges $q_{Al}(q_N)$ are noticeably closer to the corresponding values of AlN bilayer (Fig. 6.37) than those for AlN SW NTs of smaller diameter ($\sim$1 nm), by about 0.8, 0.6 and 1.3 %, respectively (which are qualitatively close for both *ac-* and *zz-*nanotubes).

To evaluate the strain energy, first of all, the optimized configuration of honeycomb AlN bilayer (Fig. 6.37) was estimated. The calculated binding energy of the AlN graphitic nanolayer was found to be 7.32 eV *per* atom, which corresponds to the nearest-neighbor Al-N distance of 1.83 Å [130]. Therefore, the energy cost *per* atom required to wrap up an AlN graphitic nanolayer into a SW NT of a given diameter and chirality (i.e., the strain energy) can be obtained from the difference between the corresponding binding energies. Figure 6.40 presents a variation of the strain energy as a function of SW NT diameters, where analogous dependencies are presented also for BN, C and GaN nanotubes [130]. The strain energies for considered nanotubes were found to be decreasing with the increasing diameters. It was also revealed that the corresponding strain energies were approximately proportional to the inverse square of the NT diameters, i.e., these nanotubes follow the classical elasticity theory. Similar to the results obtained for BN NTs [3] and GaN NTs [125], the strain energies in AlN NTs are relatively insensitive to their chirality. The energy costs to form AlN SW NTs from a graphitic nanolayer structure were found to be the lowest as compared to those necessary to form BN, GaN, and carbon nanotubes with similar diameters [130]. These are about 0.02–0.04 eV *per* atom lower than those of BN nanotubes and 0.025–0.075 eV *per* atom lower than those of GaN nanotubes (Fig. 6.40). It seems to be an advantage for the formation of AlN SW NTs, in contrast to graphene and boronitrene honeycomb monolayers. However, 2D AlN materials with a graphitic nanolayer configuration, as mentioned above, have not been synthesized experimentally so far. Obviously, the strain energy in an AlN graphitic nanolayer relative to sp^3-bonded AlN bulk structure should also be taken into account when analyzing the probability of AlN SW NTs synthesis. Such an energy was found to be 0.68 eV/atom, which is much higher than that for GaN graphitic sheet (0.36 eV/atom [125]), thus

Fig. 6.40 Strain energy in *ac-* and *zz-*AlN SW NTs relative to their graphitic-like sheet structure versus diameter of these nanotubes, according to (6.1). For comparison, the strain energies in BN, GaN and carbon nanotubes are presented. The *curves* are fitted by the least-square method (Reprinted figure with permission from Zhao et al. [130], Copyright (2004) by the Elsevier B.V. All rights reserved)
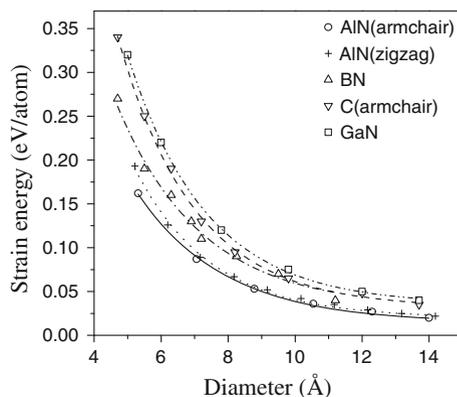
indicating that AlN graphitic nanolayer is rather unstable. Indeed, its growth unlikely starts from a highly metastable phase in experiment [130], which creates a disadvantage to the formation of AlN SW NTs, because such a high strain is difficult to alleviate by growing nanotube.

Thermal stability of AlN *ac*- and *zz*-SW NTs of different diameters was studied using MD simulations based on DFT-LCAO calculations [130]. Structural transformations of AlN nanotubes with (3,3), (6,0), (9,0) and (8,8) chiralities were simulated at several temperatures up to 1,000 K (Fig. 6.41). At 300 K, no essential changes in nanotube structures were observed as compared to optimized NT configurations, since the disorder caused by atomic thermal motions was not significant at this temperature. The cross-sections of nanotubes at 600 K became more elliptic, which was explained by the softness of AlN SW NTs that could be easily deformed in a radial direction [130]. At that temperature, the structural disorder of nanotubes caused by atomic thermal motions became significant. The analysis of the pair distribution functions displayed a feature of solid-liquid coexistence, suggesting that AlN SW NTs start melting. The lattice character of nanotubes in the axial direction disappeared after relaxing these tubes at 1,000 K. The pair distribution functions at that temperature demonstrated liquid features. It allowed the authors to deduce that the highest temperature T, when the rolled-up AlN NTs still can stably exist, is rather low, 600 K [130], due to the high strain energy relative to cubic-type materials involved in the formation of Al SW NTs. Obviously, the structural stability of nanotubes at different temperatures depends also on the NT diameter decreasing with the growth of the latter. For example, a visible deformation of the cross-section of *ac*-nanotube with (8,8) chirality was already observed at 300 K (Fig. 6.41d).
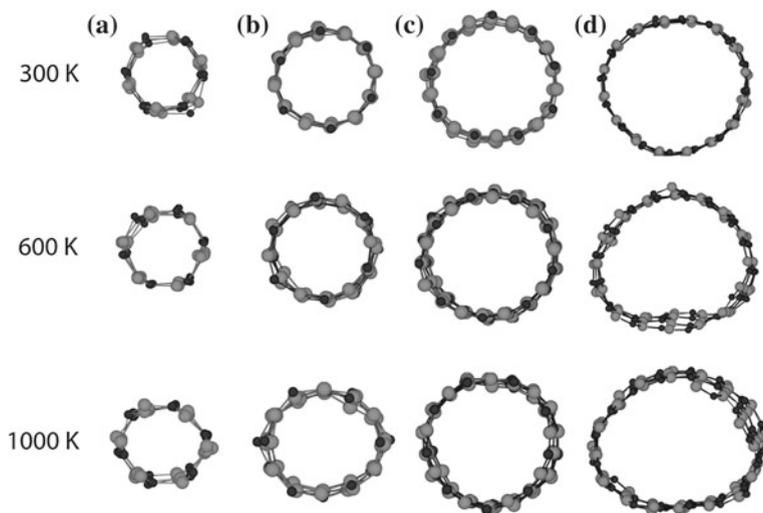
Fig. 6.41 Cross-sections of: **a** (3,3), **b** (6,0), **c** (9,0) and **d** (8,8) AlN SW NTs at the temperatures of 300, 600 and 1,000 K (Reprinted figure with permission from Zhao et al. [130], Copyright (2004) by the Elsevier B.V. All rights reserved)

6.5.2 Rolled-Up Single-Wall GaN Nanotubes

As a typical kind of a wide band-gap semiconductor with a wurtzite structure, GaN
nanotubes are gaining enhanced attention due to the high efficient blue-light-emitting
diodes produced from GaN materials [141] making their application quite promising
for full color displays [128, 142]. Single-crystal GaN NTs with the inner diameters
of 30–200 nm and wall thicknesses of 5–50 nm were successfully synthesized earlier
using the epitaxial casting techniques [121]. The stability of single-wall GaN NTs was
firstly studied using the first-principle DFT-LDA PW calculations on the electronic
and structural properties of different GaN SW NTs [125], e.g., possessing the same
(5,5) and (9,0) chiralities as shown for AlN SW NTs (Fig. 6.38). The optimized
diameters of these nanotubes (D_{NT}), accompanied by buckling, were found to be
8.47 and 8.81 Å, respectively, i.e., by 4 % smaller than for AlN NTs mentioned
above [127], although $d_{Al-N} < d_{Ga-N}$ [138]).

Fig. 6.42 shows the band structures and density of states calculated for the cor-
responding *ac*-(5,5) and *zz*-(9,0) GaN SW NTs [125]. Analogously to SiC SW NTs
(Sect. 5.5.1), zigzag nanotubes possess a direct band gap, whereas armchair nan-
otubes have an indirect gap. The maximum of the valence-band for an *ac*-GaN
NT is just near the middle of the Brillouin zone. The electronic DOSs of *ac*- and
zz-nanotubes were found to be qualitatively similar to each other (Fig. 6.42a, b). A
larger number of Ga(4*p*) and N(2*p*) states are developed by NT bond re-hybridization
upon wrapping as compared with the corresponding graphitic sheet.

To study the electronic structure of ultrathin GaN SW nanotubes, both achiral, i.e.,
(2,2), (3,3), (3,0), (4,0) and (5.0), as well as chiral, i.e., (2,1), (3,1), (3.2), (4,1) and
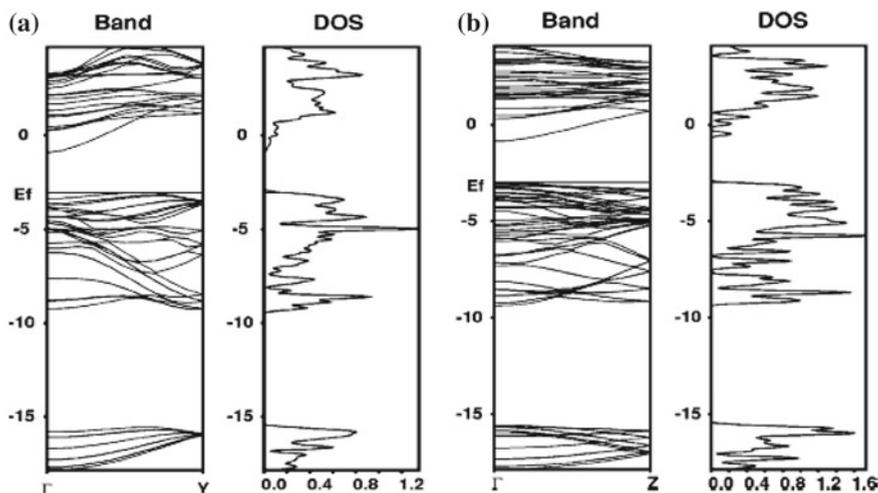
Fig. 6.42 Band structures along the nanotube axis and the corresponding density of states of (5,5)
and (9,0) GaN single-wall nanotubes. *Y*(*Z*) band edges correspond to the symmetric points in the
armchair (*zigzag*) nanotube [125]. **a** armchair. **b** zigzag

Fig. 6.43 The band structures of (n,0) GaN NTs with $n = 3 - 6$. The description of details is given in the text [139]
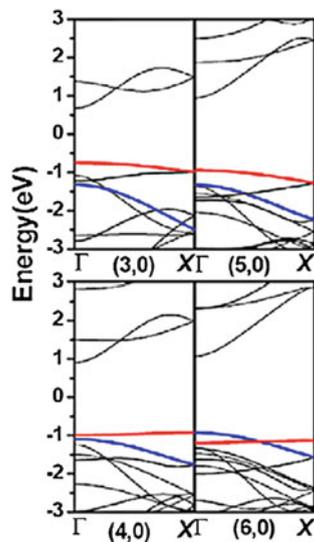
(4,2), with NT diameters changing from 3.0 to 5.5 Å, the DFT-GGA PW calculations were performed [139]. Similar to GaN NTs of larger diameters (Fig. 6.42), both *ac*- and chiral ultrathin nanotubes were found to be the indirect-band-gap semiconductors. However, not all *zz*-NTs possessed the direct gaps, e.g., (4,0) nanotube (Fig. 6.43), i.e., the gap transition from direct- to indirect-band-gap is not merely relative to the decrease of NT diameter. Apparently, the band structures of *zz*-NTs show two different behaviors due to the different symmetry for $(2n, 0)$ and $(2n - 1,0)$ NTs. Four surface states were found near the Fermi level, which would influence the band gap (Fig. 6.43): the double degenerated localized *L*-states characterized by a narrow dispersion (red lines) and the double degenerated extended *E*-states possessing a wide dispersion (blue lines). The *L*-states are pinned at about 1.0 eV below the Fermi level for all *zz*-GaN NTs. However, the *E*-states would move downwards with decreasing diameter, switching their position with the *L*-states around Γ points for just (4,0) GaN NT. The movement of the extended *E*-states leads to the band sequence change, which results in the appearance of indirect-band-gap for (4,0) GaN NTs while other zigzag nanotubes are direct-band-gap semiconductors [139]. The movement of the extended *E*-states can be attributed to the following two factors: the π–π bond re-hybridization, due to the curvature effect of the small-diameter NTs, and the formation of soft buckling separations.

Figure 6.44 shows the dependence of the band gaps for modest-size *ac*- and *zz*-type GaN SW nanotubes on their diameters [125]. Unlike the alternating band gap of carbon zigzag nanotubes with a diamond shape, the band gaps of GaN nanotubes decrease smoothly with the decreasing diameter (Fig. 6.44). The band gap of GaN SW (n,n) NTs decreases slightly with decreasing diameter, whereas that of GaN SW (n,0) NTs reduces significantly. This factor reflects the ionic character of bonding, i.e., *s* and *p* bands localized on Ga and N atoms are well separated [143]. With the
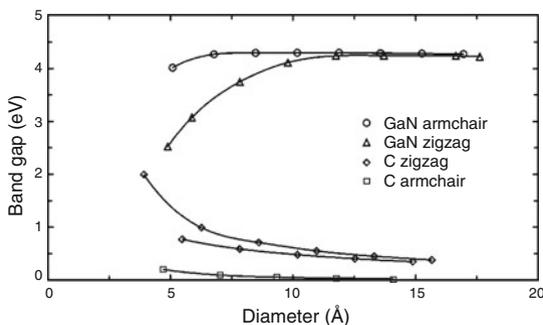
Fig. 6.44 Band gaps of *ac*- and *zz*-GaN SW NTs as a function of the diameter. For comparison, the changes of band gaps in *zz*-CNTs are shown below. (The *bottom curves* describe changes of band gap in *ac*-CNTs.) [125]

increasing nanotube diameter the band gap converges to the value of the graphitic GaN sheet. Similar dependencies of Al SW NT band gaps on nanotube diameters were obtained later [127].

An original idea for the formation of GaN SW nanotubes was suggested to use carbon nanotubes as a template [125]. GaN NTs can be synthesized at the open edges of CNTs since vertically aligned carbon nanotubes were successfully grown on glass [144]. This aligned carbon nanotube can be a suitable template for GaN NT growth. The extra energy costs necessary for the formation of GaN graphitic nanolayers can be overcome by GaN adsorption on the existing tubular form of substrates. The precise structures appearing during the GaN nucleation on carbon nanotubes is still under investigation [125]. The strain caused by the lattice mismatch between graphitic GaN (Fig. 6.37) and graphene (achieving ∼25 %), as well as the relative energetics of *ac*- and *zz*-GaN NTs can play an important role in the synthesis of GaN nanotubes on CNTs. It was found that *zz*-GaN NTs are more favorable than armchair nanotubes where the strain is relaxed within a few GaN layers. Thus, interfaces between metallic *ac*-CNTs and semiconducting *zz*-GaN NTs can be fabricated, which opens the possibility to apply this heterostructure for ultimate nanoscale photodetectors or electroluminescent devices [125].

6.5.3 Rolled-Up Single-Wall (Al,Ga)N Nanotubes

As mentioned in Sect. 6.4, GaN/AlN hetero-structures and $Al_x Ga_{1-x}N$ alloys have a strong technological appeal, due to the possibility of varying their direct band gaps in a wide interval, and to their high thermal and mechanical stability [140]. The following important applications of these structures may be mentioned: LEDs (light-emitting diodes) for low-energy consumption light emission [145], blue lasers for multimedia disks [146], field effect transistors (FET) [147], and high electron mobility transistors

(HEMT) [148]. Although the reproducible synthesis of AlN and GaN single-wall nanotubes is still problematic, the results of theoretical simulations on (Al, Ga)N SW NTs would be very promising in nanoelectronics. Three types of (Al, Ga)N nanotubes have been simulated so far: alloy-type $AlGaN_2$ [138] and $Al_xGa_{1-x}N$ SW NTs [138, 140], as well as $GaN/Al_xGa_{1-x}N$ SW NT hetero-junctions [140].

The total energies of a few possible structures for a honeycomb-type $AlGaN_2$ nanosheet were estimated using the DFT-GGA PW calculations [138]. The configuration shown in Fig. 6.45a, where Ga and Al atoms were separated by N atoms, was found to be most stable. Other structures, e.g., those where Ga atoms were directly bonded to Al atoms, were found to be evidently less stable. More than one type of zz- and ac-$AlGaN_2$ NTs can exist (analogous situation was considered in Sect. 5.5.5), depending on how an $AlGaN_2$ sheet is rolled up (Fig. 6.45a), e.g., two types of zigzag nanotubes: ZZ1 $(n,0)$ with $n = 5$–16 (Fig. 6.45b) and ZZ2 $(0,n)$ with $n = 3$–8 (Fig. 6.45c), as well as two types of armchair nanotubes: AC1 (n,n) with $n = 3$–11 (Fig. 6.45d) and AC2 (m,m) with $m = 2$–5 (Fig. 6.45e).

Figure 6.46 shows the variation of the calculated GGA band gaps of various $AlGaN_2$ nanotubes imaged in Fig. 6.45 with the NT diameter. Those band gaps depend on both the diameter and chirality being converged to that of the honeycomb $AlGaN_2$ sheet when the diameter of the tube becomes very large [138]. The relatively smaller band gaps for the $AlGaN_2$ nanotubes with smaller diameters can be attributed to the curvature-induced strong hybridization effect. For nanotubes with the same diameter, the AC1 NTs have a slightly larger band gap, moreover, the band gaps of the $AlGaN_2$ NTs and a honeycomb sheet are smaller than those of bulk wurtzite $Al_xGa_{1-x}N$ alloys $(0 < x < 1)$, which have tunable direct band gaps between 3.4 and 6.1 eV, depending on Al concentration. Thus, $AlGaN_2$ SW NTs can be recognized as important semiconductors for optoelectronic device applications over the visible spectral range [138].

A more generalized case of the alloy-type single-wall nanotubes, $Al_xGa_{1-x}N$ (10,0) NTs, characterized by the variable x describing Al concentration (with fixed magnitudes of 0.1, 0.3, 0.5, 0.7, 0.9), was simulated using the DFT-LCAO LDA
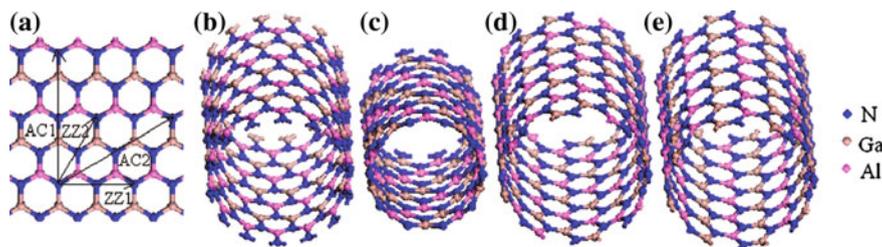
Fig. 6.45 Atomic configurations of the most stable $AlGaN_2$ sheet (**a**), containing wrapping vectors of the four types of NTs: ZZ1 (14,0) (**b**), ZZ2 (0,5) (**c**), AC1 (8,8) (**d**), and AC2 (4,4) (**e**)—the explanations are given in the text. Ga, Al, and N atoms are indicated by *light-brown*, *pink*, and *blue* spheres (Reprinted figure with permission from Pan et al. [138], Copyright (2008) by the American Chemical Society)
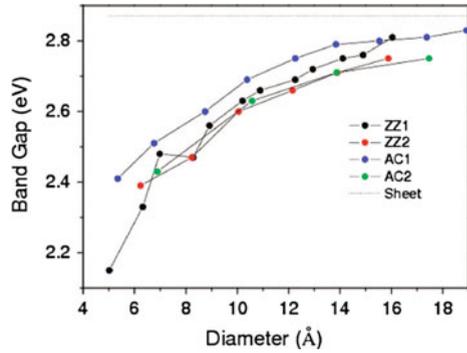
calculations [140]. For each concentration, five independent nanotube configurations
were generated by randomly distributing Ga and Al atoms on the cation sites. The
number of five was chosen because a comparison of various properties calculated
for the case of $x = 0.5$ using the two sets with five and ten independent random
configurations clearly demonstrated qualitatively negligible difference between the
average values obtained from both sets (for each Al concentration, the standard
deviations from the average values were found to be lower than 10^{-2} eV). Figure 6.47
shows alloy-type nanotubes with two particular zz-NT structures of Al$_{0.3}$Ga$_{0.7}$N and
Al$_{0.5}$Ga$_{0.5}$N (the disordered analog of AlGaN$_2$ nanotube configurations which are
present in Fig. 6.45b, c).

The calculated average band gap for each Al concentration can deviate from the
simple linear interpolation between the extreme values from the perfect GaN and
AlN nanotubes. The average band gap variation depending on the Al concentration
in the alloy nanotubes was described by a non-linear equation which included the
so-called bowing coefficient b, according to the following equation [140]:

$$E_{gap}^{Al_xGa_{1-x}N}(x) = (1 - x)E_{gap}^{GaN} + xE_{gap}^{AlN} - bx(1 - x), \qquad (6.6)$$

where $E_{gap}^{Al_xGa_{1-x}N}(x)$ is the average band gap for arbitrary Al concentration x, while
E_{gap}^{GaN} and E_{gap}^{AlN} are the band gaps for perfect GaN sand AlN nanotubes, respectively.
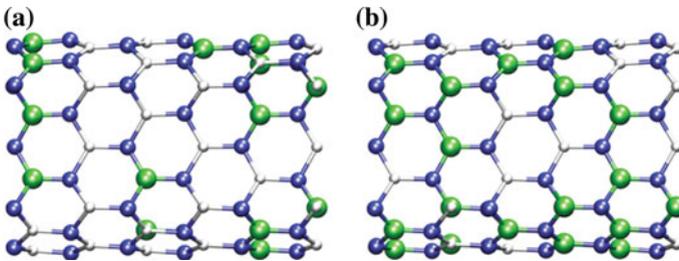
Fig. 6.47 Models of disordered Al$_x$Ga$_{1-x}$N (10,0) NTs with **a** $x = 0.3$ and **b** $x = 0.5$. The small,
medium and large spheres represent Ga, N and Al atoms, respectively [140]
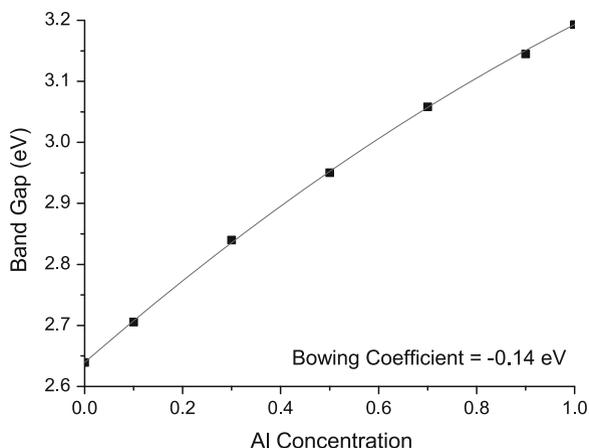
Fig. 6.48 LDA band gap variation of $Al_xGa_{1-x}N$ nanotubes as a function of Al concentration x (Reprinted figure with permission from de Almeida et al. [140], Copyright (2009) by the Elsevier B.V. All rights reserved)

Figure 6.48 shows the results for the average band gap variation with x. The total negative bowing coefficient was estimated from this plot to be ∼0.14 eV [140]. Although the band gap bowing coefficient for wurtzite $Al_xGa_{1-x}N$ bulk random alloys can have a large dispersion from positive to negative values (due to the existence of different random configurations with different band gaps, as was concluded elsewhere [149]). This is not the case for $Al_xGa_{1-x}N$ alloy nanotubes, where the standard deviation in the band gap values and the total energies for different configurations of each NT with different Al concentrations is lower than 10^{-2} eV. No evidence was found on the dependence of the average distance between Al atoms in each NT and their total energies (and, consequently, the formation energies) on arbitrary Al concentration. After the corrections of LDA results based on the comparison between the experimental and theoretical data obtained for wurtzite AlN and GaN bulk, the range of allowed band gaps obtained by varying the value of x in the $Al_xGa_{1-x}N$ NTs, was changed from 3.45 to 4.85 eV ($\lambda = 359$ to 256 nm in the ultraviolet region) with a band gap variation of 1.4 eV, almost the double of that for bulk alloys [140].

The (10,0) $GaN/Al_xGa_{1-x}N$ nanotube hetero-junctions were studied for $x = 0.1, 0.3, 0.5, 0.7, 0.9$ and 1.0 (the limit case of GaN/AlN junction as shown in Fig. 6.49) [140]. The atomic positions and the supercell size have been fully relaxed. At the final configurations both GaN and AlN nanotubes were stressed, due to the difference between the diameters of isolated nanotubes. The maximum difference between the diameters of the nanotubes in the hetero-junction occurs for the limit case $x = 1.0$. The properties of the $GaN/Al_xGa_{1-x}N$ NT hetero-junctions for each Al concentration were averaged using three independent $Al_xGa_{1-x}N$ random configurations.

Figure 6.50 shows the band structure alignment profile for the GaN/AlN (10,0) NT hetero-junction. The results reveal type-I band alignment with electrons and
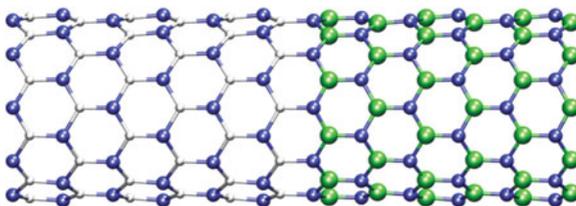
Fig. 6.49 Model of the GaN/AlN (10,0) NT hetero-junction. The *small*, *medium* and *large spheres* represent Ga, N and Al atoms, respectively [140]

Fig. 6.50 Profile of the band structure for the GaN/AlN (10,0) NT hetero-junction. E_{gap}^{GaN} and E_{gap}^{AlN} represent the band gaps of (10,0) AlN and GaN NTs while the meanings of VBO and CBO are described in the text (Reprinted figure with permission from de Almeida et al. [140], Copyright (2009) by the Elsevier B.V. All rights reserved)
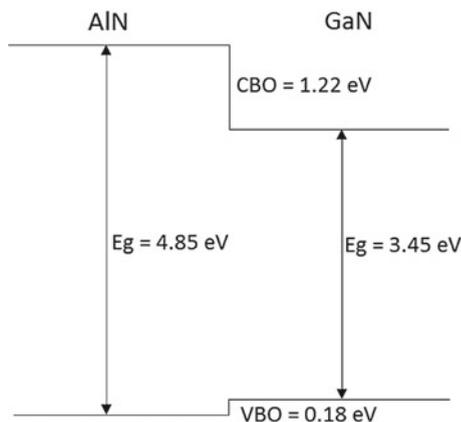
holes, both localized at the GaN side of the interface. The calculated valence and conduction band offsets (VBO and CBO, respectively) for the GaN/AlN nanotube hetero-junction were found to be 0.18 and 0.34 eV, respectively. The VBO value was obtained definitely lower than that found for *c*- and *w*-GaN/AlN bulk hetero-junctions (0.82 and 0.84 eV, respectively [150]). After the correction of band gap parameters according to the scheme based on the comparison of the experimental and theoretical data, as described above, the CB offset for the GaN/AlN NT hetero-junction increased up to 1.22 eV [140].

In spite of the promising prospects for technological applications described above, the synthesis of the stable AlN, GaN and (Al,Ga)N SW nanotubes remains a great experimental challenge because of their high strain energy as compared to the bulk materials [135].

6.5.4 Faceted AlN Nanotubes

Even if single-wall nanotubes of the group-III metal nitrides were synthesized, the further growth of the NT wall along the radial direction would not stop immediately [121, 135]. It would adsorb the incoming nitride species in the environment and form

thick-walled sp^3-bonded single-crystalline nanotubes with faceted hexagonal cross sections (similar to those of SiC NT considered Sect. 5.5.4) in order to release the strain energy. Moreover, the cylindrical multi-wall shape of GaN NT was found to be unstable and broken even at 300 K as followed from the MD simulation [131]. The surface dipoles on the lateral facets of AlN and GaN NTs facilitate the adsorption of polar group-III metal nitride species and keep the growth of hexagonal-shaped nanotube wall continuing along the radial direction [135]. The most effective way for the simulation of the sp^3-bonded faceted AlN and GaN nanotubes possessing the point symmetry D_{3h} was found to be a removal of the core nanowire symmetrically arranged around its axis from the larger NW of the same faceting (Fig. 6.51). The axial orientation of the as-synthesized hexagonal-shaped AlN (GaN) NWs and faceted AlN (GaN) NTs is always in the [0001] direction whereas the experimental data for determining their lateral facet orientations have not been available so far [135]. In analogy with single-crystalline SiC nanotubes, the corresponding six lateral facets can be chosen as attributed to the $\{10\bar{1}0\}$ family (Sect. 5.5.4), since its surface energy is smaller than that of $\{11\bar{2}0\}$ (136 vs. 143 meV/Å^2, respectively), due to a lower density of the dangling bonds on the former (0.12 vs. 0.14/Å^2). A similar result was also reported for GaN NWs, which gave 118 and 123 meV/Å^2 for $(10\bar{1}0)$ and $(11\bar{2}0)$ surfaces, respectively [151].

Figure 6.51 presents dependencies of the strain energies for AlN NWs, faceted AlN NTs of different wall thicknesses and rolled-up AlN SW NTs on their diameters, i.e., $E_{strain}(D)$ [135].

For the first two types of nanostructures, the strained energy was determined as the difference between their total energy *per* atom and that for AlN wurtzite bulk, while the diameter was evaluated by the average of the radial distance between the central axis and the outermost atoms. As defined above, E_{strain} for the rolled-up
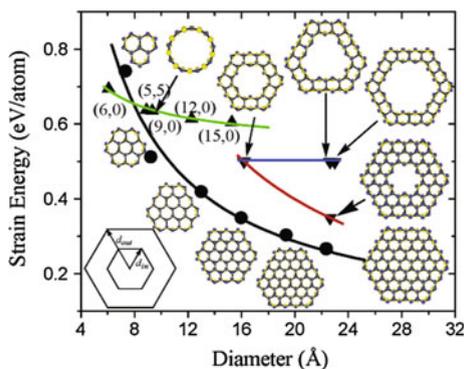
Fig. 6.51 The strain energies of AlN NWs, faceted AlN NTs and rolled-up AlN SW NT as functions of diameter. E_{strain} for different configurations of AlN NWs are represented by the *solid circles*, while the *black line* is the fitting *curve* by using the expression $E_{strain} = C/D$. The strain energies of faceted AlN NTs and single-wall AlN NTs are denoted by the *down* and *up triangles*, respectively (Reprinted figure with permission from Zhao et al. [135], Copyright (2006) by the American Chemical Society)

SW NT was estimated as the difference between the total energy of nanotube *per* atom and that for the corresponding honeycomb AlN(0001) sheet. Obviously, the strain energy of a nanowire consequently reduces with the growth of its diameter, following its inverse proportionality, i.e., $E_{strain} \sim 1/D$ [135]. The strain energy of AlN SW NT decreases monotonically with the increasing nanotube diameter and saturates at the value corresponding to the AlN graphitic-like sheet (Fig. 6.51).

However, for faceted AlN NTs, the corresponding $E_{strain}(D)$ dependencies were found quite different. The strain energies of double-wall single-crystal AlN NTs with three different diameters, but equal thickness, keep constant, ∼0.50 eV/atom. The strain energy of a triple-wall faceted AlN NT is greatly reduced, to ∼0.35 eV/atom, which is comparable to that of ∼0.27 eV/atom for AlN NW with the same diameter.

The variation of strain energy for thick-walled faceted AlN NTs can be understood since E_{strain} in this case mainly arises from the curvature of the external and internal surfaces and the local structural distortion of the surface atoms. The main distortion occurs mainly near the surfaces, whereas the deviation of the bond lengths and bond angles in the core region from those of the perfect wurtzite AlN crystal is quite small. The strain energy of the faceted AlN NTs can be approximately evaluated by the expression [135]:

$$E_{strain}^{AlNNT} = \frac{8E_{surf}}{\sqrt{3}n(d_{out} - d_{in})}, \tag{6.7}$$

where E_{surf} is the surface energy of all six $\{10\bar{1}0\}$ facets, n is the atomic density, while d_{out} and d_{in} are the outer and inner diameters of the faceted AlN NTs (shown in the inset of Fig. 6.51). The strain energy of the faceted AlN NTs is proportional to the inverse of the wall thickness and independent of the nanotube diameter. The E_{strain} of the double- and triple-wall AlN nanotubes were found to be 0.53 and 0.35 eV/atom, respectively. By using this expression, $E_{surf} \approx 136$ meV/Å^2, while $n \approx 0.14/$Å^3 for the double-wall AlN NT and $0.12/$Å^3 for the triple-wall AlN NT. They are in good agreement with 0.50 and 0.35 eV/atom for faceted DW and TW AlN NTs, respectively, obtained by direct first-principles calculations. This expression is also valid for describing AlN NTs with $d_{in} = 0$, (i.e., AlN NW) and well reproduces their strain energies [135].

The band structures of *w*-AlN bulk (Fig. 6.35b), nanowire, rolled-up and faceted AlN nanotubes (Fig. 6.51), as well as H-doped AlN NW and faceted NT were evaluated using the DFT-LCAO method [135]. Wurtzite-type AlN bulk possesses a direct band gap at Γ point of the Brillouin zone (Fig. 6.52a), analogically to other group-III metal nitrides [104]. Despite underestimate of the band gap width, typical for traditional DFT methods, they are known to reproduce well both the occupied states and the dispersion of the bands [152]. The band structures of both AlN NW (Fig. 6.52b) and faceted AlN NT (Fig. 6.52c) clearly indicated that some bands appeared in the band gap of *w*-AlN, which were found to be very smooth and, thus, highly localized in a real space. An analysis of the corresponding PDOSs showed that they mainly arose from the states of atoms located on the hexagonal facets (Fig. 6.51), which are the surface states [135]. The occupied surface bands consisted of mainly the atomic
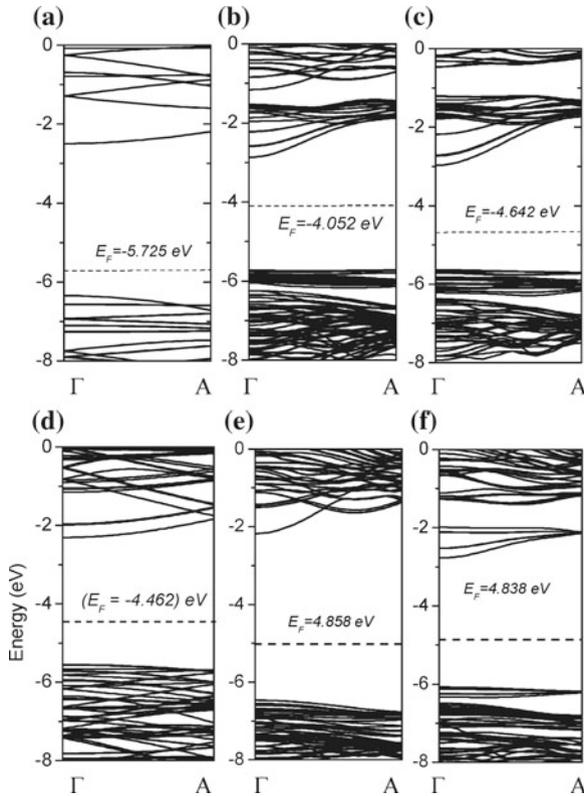
Fig. 6.52   Band structures along the direction $\Gamma(0, 0, 0)2\pi/a \rightarrow A(0, 0, 0.5)2\pi/a$ in the reciprocal space of the Brillouin zone drawn for: **a** bulk AlN (wurtzite); **b** AlN NW; **c** faceted AlN NT, **d** rolled-up (9,0) AlN SW NT, **e** H-doped AlN NW, and **f** H-doped faceted AlN NT. The dashed lines represent the Fermi levels which were directly obtained from Fermi-Dirac distribution at room temperature (Reprinted figure with permission from Zhao et al. [135], Copyright (2006) by the American Chemical Society)

N(2p) states, while the unoccupied surface bands arose from the Al(3p) states. This was found to be consistent with asymmetry of the charge distribution on the surfaces where the valence electron density is strongly accumulated around N atoms because of their strong 2p potentials [135]. On the other hand, the band structure of rolled-up zz-AlN NT bears no resemblance to that of w-AlN bulk, due to their structural difference (Fig. 6.52d). The width of the occupied surface bands of the AlN NW was found to be about 0.45 eV with its frontier state 0.52 eV above the top of the valence band of w-AlN (Fig. 6.52b). For the faceted AlN NT, the width of occupied surface bands is extended to 0.66 eV and the frontier surface state is 0.74 eV above the top of the valence band of w-AlN, due to the contribution from the atoms on the inner nanotube facets (Fig. 6.52c). These surface states narrow the band gap and, thus, should definitely be responsible for changes in the electronic properties of AlN NWs

and faceted NTs [135]. The surface bands located inside the band gap of the clean AlN NW disappear in the corresponding hydrogen-passivated nanowire (Fig. 6.52e). However, the surface bands remain in the band gap of H-doped faceted AlN NT, as shown in Fig. 6.52f, which is related to the unsaturated bonds at the interior facets. This also confirms that the flat bands located in band gaps of pure AlN NW and faceted NT are indeed the surface bands.

It has also been found that when the wall width of the faceted AlN NT is reduced to a single atomic layer, the hexagonal cross-section becomes unstable and transforms to a round cross-section after relaxation, forming a rolled-up *zz*-AlN SW NT [135]. On the other hand, the faceted AlN DW NT imaged in Fig. 6.51 (in the middle of the upper part) can be disintegrated into the two individual (9,0) and (15,0) rolled-up AlN SW NTs, respectively, with the corresponding strain energies 0.64 and 0.61 eV/atom (*cf*. with 0.50 eV/atom for faceted AlN DW NTs), which can form rolled-up *zz*-AlN DW NTs. When the latter coaxial nanotube was heated at 1000 K (in the framework of MD simulation), a distorted hexagonally faceted nanotube was obtained again by the formation of ionic Al-N bonds between the inner and outer round nanotube shells. Hence, the tendency of transition from faceted to rolled-up AlN NT configuration and back is quite obvious. This energy balance clearly demonstrates the difficulties in fabricating both single- and multi-wall rolled-up AlN NTs, In any case, it is a great challenge to realize the synthesis of the reproducible rolled-up AlN SW NTs [135].

6.6 Group III Metal Nitride Nanowires

6.6.1 Prismatic AlN Nanowires

Randomly oriented as well as aligned AlN NWs were fabricated using a number of alternative methods: the Al powder reaction in the NH_3/N_2 atmosphere [153], the catalytic metal-organic chemical vapor deposition [154], the radio frequency magnetron discharge sputtering of the Al-containing target in the Ar/N_2 gas mixture [86], the direct arc discharge [155], and self-patterning [156]. Group-III metal nitride nanowires provide essential number of applications, ranging from chemical and temperature sensors [157] to nanomechanical resonators [158] and field emitters [159]. The diameters of AlN NWs (d_{NW}) synthesized using different methods were estimated to be in the range of 5–100 nm. The adsorption edge of AlN NWs was found to be blue-shifted by 0.27 eV from the bulk edge as revealed by transmission spectra [160], which was attributed to the quantum size effect in the radial direction [161]. This effect makes AlN as well as other homogeneous and heterogeneous group-III metal nitride nanowires an attractive material for high performance light emitting diodes covering the spectral regime of approximately 370–480 nm [162]. Although the number of aluminium and other group-III metal nitride NWs fabricated using different techniques substantially increases, a deeper analysis of the basic process of nanowires formation is still lacking, therefore, controlling the

growth of the nanowires is still a challenging issue [163]. A number of theoretical simulations on AlN NWs have been performed so far [135, 157, 158, 163–168]. The corresponding 1D NW models were exclusively chosen as those possessing a single-crystalline w-AlN NW morphology (WZ, space group $P6_3mc$ as shown in Fig. 6.35) with the growth direction along the [0001] axis, although the structure of their lateral facets could not be directly identified in the experiments [135]. However, recent theoretical simulations have showed that with the decrease of nanowire diameter to the sizes of ultrathin NW a structural transformation of w-AlN NWs to graphite-like h-AlN NWs can occur (GL, which morphology is typical for BN described by $P6_3/mmc$ group as imaged in Fig. 6.1a) [158, 163, 167] although such a transformation is rather not possible in the case of AlN bulk and its various surfaces with prevailing sp^3 bonding between Al and N atoms as considered in Sect. 6.4. For simulations of 1D AlN nanowires, various ab initio methods were applied: (i) the DFT-LCAO methods as implemented in either CRYSTAL [165, 166, 168] or SIESTA [135, 158, 167] packages as well as (ii) DFT-PW methods [157, 163, 164] applied for nanowires incorporated in repeating tetragonal supercells with such a dimension that the interaction between NWs and their nearest images was negligible. Besides, periodic atomistic models applied in all theoretical studies of nanowires mentioned above, both continuous and finite element models, were used for detailed description of mechanical (e.g., elastic) NW properties and comparison with atomistic models [166, 168].

The axial orientation of arbitrary w-AlN nanowire coincides with the [0001] direction accompanied with hexagonal cross sections (Fig. 6.53), whereas the orientations of six NW lateral facets (faceting) can be determined via the minimum of their total surface energy $E_{surf}(d_{NW})$ or strain energy $E_{strain}(d_{NW})$ defined from (6.7) for the case of $d_{in} = 0$ (the profile of which is shown in Fig. 6.51). For [0001]-oriented wurtzite-type nanowires, the energetically more preferable lateral facets of AlN NWs can be considered, as shown in either Fig. 6.53b or Fig. 6.53c, densely-packed facets with different angular orientations. According to the results of ab initio
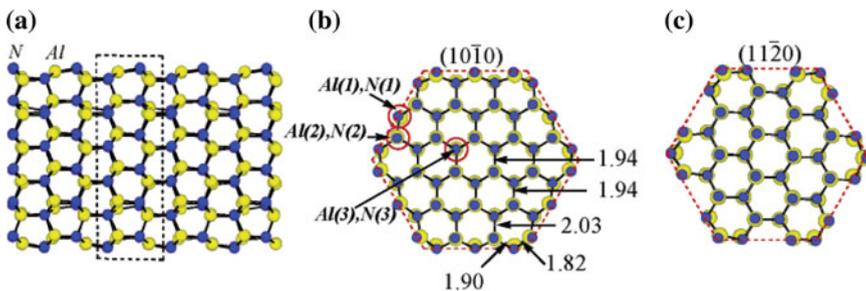
Fig. 6.53 Equilibrium configurations of [0001]-oriented AlN NWs with a different faceting: **a** aside view and **b** across view of an AlN NW with six {10$\bar{1}$0} lateral facets; **c** across view of an AlN NW with six {11$\bar{2}$0} facets. *Dash-limited rectangle* (**a**) determines the period of nanowire while *dash-limited hexagons* (**b**, **c**) determine profiles of nanowire cross-sections. The labeled atoms in central panel **b** were used for construction of the corresponding DOSs imaged in Fig. 6.54 [135]

slab calculations [135], the corresponding values of $E_{surf}(d_{NW})$ were found to be 136 and 143 meV/Å^2, respectively. Figure 6.53b, c give the equilibrium configurations of two AlN NWs with similar diameters, 16.0 and 15.6 Å, but different lateral facets, $\{10\bar{1}0\}$ and $\{11\bar{2}0\}$, respectively. $E_{strain}(d_{NW})$ of the former was calculated to be ∼94 meV/atom smaller than that of the latter, while the corresponding total surface energies of these nanowires were found to be 153 and 156 meV/Å^2, respectively [135], slightly higher than those obtained for infinite two-dimensional slabs as mentioned above. These differences can be well attributed to the corner atoms of the hexagonal NW cross-section whose coordinate environment is quite different from that of the atoms on infinite two-dimensional slabs, and, thus, the Al-N bonds associated with these atoms were shortened to ∼1.82 Å as compared to those of other surface and internal atoms (Fig. 6.53b). Thus, AlN NWs with $\{10\bar{1}0\}$ faceting can be considered as the energetically most preferable.

The analysis of the projected density of states (PDOS) shows that they mainly arise from the states of the atoms positioned on the facets (Fig. 6.54), clearly indicating a presence of predominantly surface states (*cf.* with Fig. 6.52b which shows the band structure of *w*-AlN nanowire terminated by six facets). Occupied surface bands mainly arise from the states of N atoms, while unoccupied surface bands mainly arise from the states of Al atoms, respectively. This is consistent with the asymmetry of charge distribution on the surfaces where the valence electron density is strongly accumulated around the N atoms because of their strong 2*p* potentials.

When the diameter of AlN NW decreased to the ultrathin size (as was mentioned above), a phase transformation WZ → GL was repeatedly observed [158, 163, 167]. As a result, the length of *w*-AlN lattice parameter *c* (Fig. 6.55), the direction of
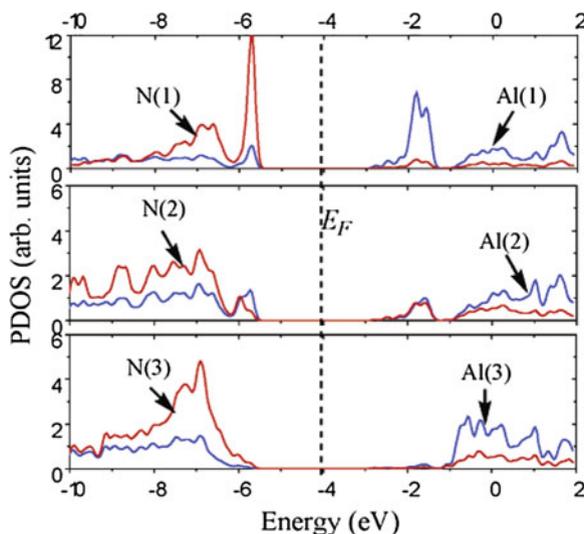
Fig. 6.54 Electron density of states projected onto different atoms labeled in Fig. 6.53b. The *dashed line* designates the Fermi level (Reprinted figure with permission from Zhao et al. [135], Copyright (2006) by the American Chemical Society)
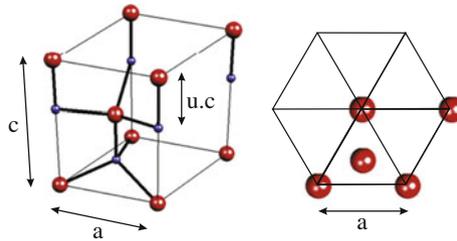
Fig. 6.55 Unit cell for wurtzite lattice structure of arbitrary binary compound (detailed description is given in Fig. 6.35b) (Reprinted figure with permission from Yvonnet et al. [168], Copyright (2010) by the Elsevier B.V. All rights reserved)

which coincides with the direction of NW axis, was found to be reduced, while cross-sections of newly-formed h-AlN NWs included Al and N atoms in equidistantly separated planes unlike those in w-AlN NWs (Fig. 6.56).

An initial atomic configuration for the construction of h-Al NW (GL phase), which possesses the diameter of ultrathin size (e.g., that imaged in the left panel of Fig. 6.56, which can be rather considered as ultrathin nanotubes), was chosen the pristine AlN nanowire of WZ phase corresponding to the native morphology of bulk material [158]. The initial 1D lattice parameters were chosen to be those of AlN bulk (Fig. 6.55): $a_{WZ} = 3.11$ Å and $c_{WZ} = 4.98$ Å. Then the system was consequently compressed along the nanowire axis using the maximum displacement of 0.1 Å (with total geometry optimization) while the interatomic forces were stabilized being less than 0.04 eV/Å. The final configuration obtained for the free-standing AlN NW attributed to the hexagonal GL phase where Al and N atoms were placed in alternating positions in honeycomb cross-sections, with the lattice constant $a_{GL} = 1.97$ Å, that is, the in-plane distance between two successive Al and N atoms. The distance between the nearest equidistantly separated hexagonal sections is $0.5c_{GL} = 1.87$ Å, i.e., length of GL NW unit cell is $l_{NW} = c_{GL} = 3.74$ Å being reduced from 4.98 Å for WZ NW [158]. However, by applying a pulling force of 0.40 nN, AlN NW retains the original WZ configuration with slightly reduced lattice parameters $a_{WZ} = 2.79$ and $c_{WZ} = 4.86$ Å.

To understand the origin of WZ $\leftrightarrow$ GL NW phase transformation, their properties were analyzed [163]. For example, a noticeable difference between GL and WZ nanowire phases is their volume difference, which is proportional to $l_{NW} \cdot (d_{NW})^2$. Despite the resemblance in the atomic structure, the bulk WZ structure has a lower coordination number (4) as compared to that of GL (5). Therefore, the GL structure possesses a more negative Coulomb binding energy as compared to the WZ phase. On the other hand, the WZ structure has a stronger bond energy than the GL phase. The formation of the nanowire lost the bond energy at the surface. It means that for ultrathin nanowires with high surface-to-volume ratio, the GL structure becomes more stable due to its large Coulomb interaction energy, whereas for thicker nanowires, the WZ structure regains its stability due to a larger contribution from the bond energy [163].

WZ

GL
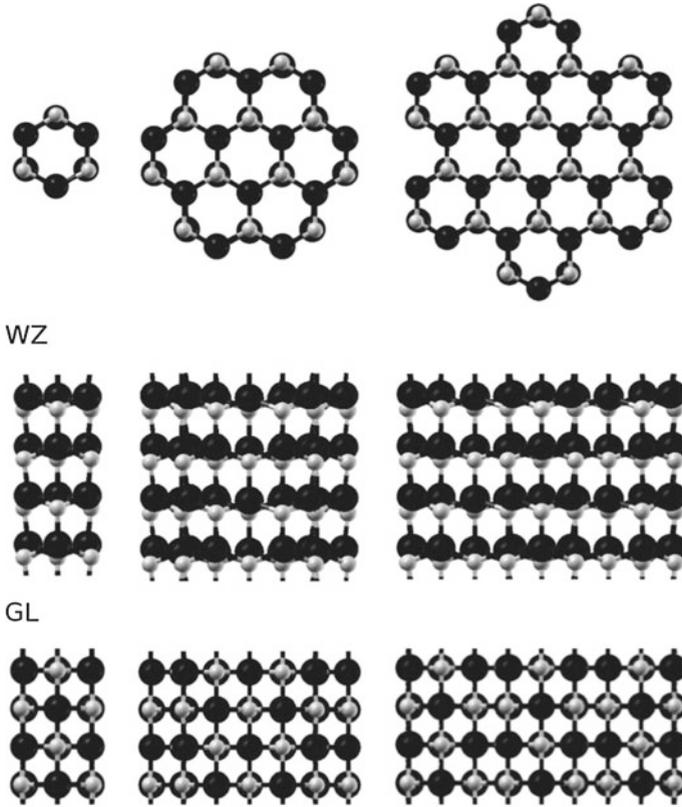
Fig. 6.56 Cross-sections (*top panel*) and lateral images (*middle and bottom panels*) of [0001]-oriented AlN NWs labeled as $R1$, $R2$ and $R3$ (possessing three different diameters) for the two structural phases, WZ and GL. The Al and N atoms are represented by *dark* and *light gray balls* respectively (Reprinted figure with permission from Mitran et al. [167], Copyright (2011) by the Elsevier B.V. All rights reserved)

The quantitative parameter, which can help for the better understanding of differences between the structures of AlN nanowires of GL and WZ phases (depending on both d_{NW} and l_{NW} parameters), is formation energy *per* Al-N pair [164]:

$$E_{form}(d_{NW}, l_{NW}) = [E_{tot}(n_{Al-N}) - n_{Al-N}\mu_{Al} - 0.5n_{Al-N}\mu_N]/n_{Al-N}, \quad (6.8)$$

where n_{Al-N} is the number of Al-N pairs *per* NW unit cell, E_{tot} the calculated total energy of AlN nanowire, μ_{Al} and μ_N the chemical potentials of Al and N obtained from the energies of Al atom in the face-centered cubic metal and isolated N_2 molecule, respectively. For both GL and WZ Al NWs of different diameters and UC lengths, the equilibrium periodicity of the nanowire ($l_{NW} = c_{eq}$) is obtained by minimizing the total energy E_{tot}. The main goal of this comparative analysis
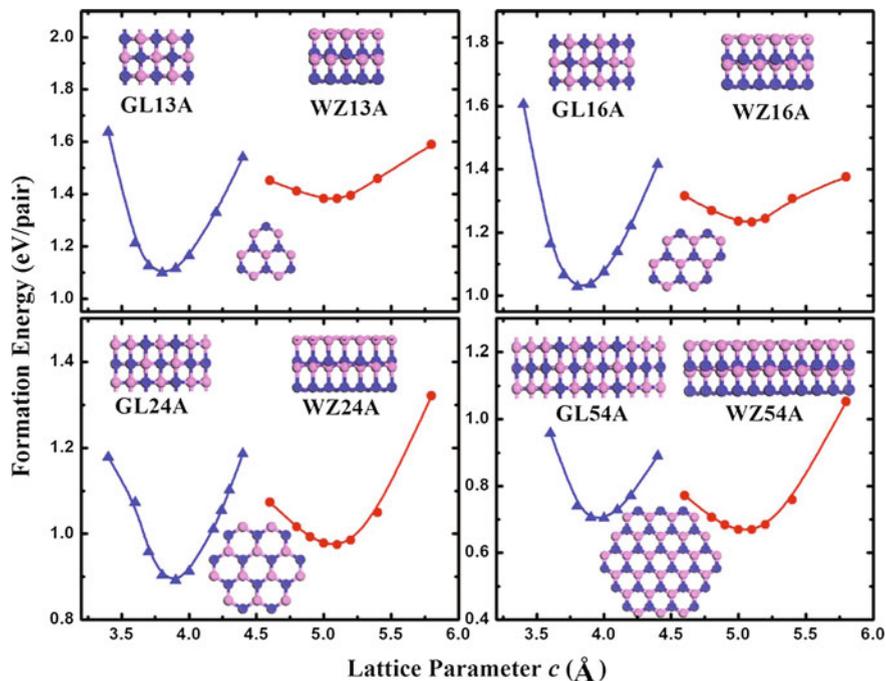
Fig. 6.57 Formation energies of GL and WZ phases of [0001]-oriented AlN nanowires as a function of NW UC length c. Two digits after phase labels correspond to the number of atoms in mono- (GL) or bi- (WZ) layered cross-sections. The insets are the lateral and across views of the nanowires (Reprinted figure with permission from Wu et al. [163], Copyright (2009) by the AIP Publishing LLC)

is the study of the energetic stability of different AlN nanowire phases including its dependence on the NW diameter. Figure 6.57 presents plots of energy curves $E_{form}(l_{NW})$ for different values of d_{NW} for both GL and WZ phases of nanowires accompanied by their corresponding lateral and across images. The minima of energy curves shown in Fig. 6.57 directly correlate with the optimized structures of AlN NWs. Obviously, the nanowires of GL phase are energetically more stable than WZ phase NWs for ultrathin nanowire diameters only, while for thicker NWs, the GL becomes more unstable. When the diameter increases up to 54 atoms *per* Al-N layer, the NW WZ phase is more favored as the formation energy for GL54A is higher by 0.034 eV *per* Al-N pair than that for WZ54A. On the other hand, E_{form} for GL13A NW is lower by 0.285 eV/pair *per* Al-N pair than that for WZ13A, i.e., the former is substantially more stable [163].

Phase transformation WZ $\leftrightarrow$ GL can be considered not only for morphology of nanowires possessing infinite length, but also for finite size nanorods, the length of which can be consequently increased up to infinity (NW) [163]. Figure 6.58 presents a schematic phase diagram of AlN nanorod, which suggests a possible growth route
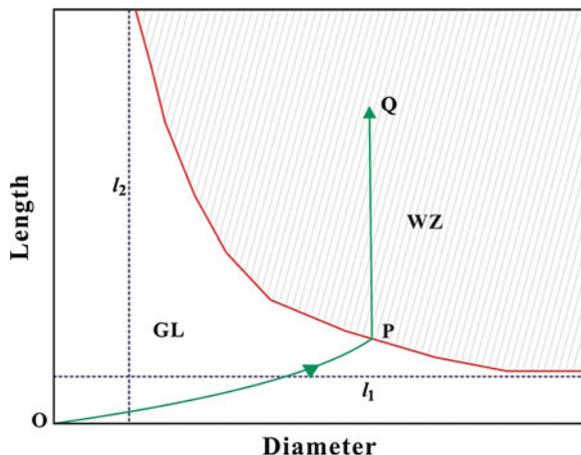
Fig. 6.58 Qualitative diagram showing areas for GL and WZ phases of [0001]-oriented AlN nanorod depending on its diameter and length. *Straight lines* l_1 and l_2 show two asymptotes of the coexistence border between both phases, where line l_1 corresponds to the transformation length for the infinite large diameter of nanorod (thickness of 2D film) while l_2 corresponds to the smallest possible diameter for AlN nanowire of the infinite length. A possible trajectory of nanorod growth $O \rightarrow P \rightarrow Q$ is described in the text (Reprinted figure with permission from Wu et al. [163], Copyright (2009) by the AIP Publishing LLC)

$O \rightarrow P \rightarrow Q$, which describes the appearance of WZ morphology. The process $O \rightarrow P$ occurs in the GL structure region, reflecting the fact that in the early stage of nanorod growth, the graphite-like structure is more favored. As the growth process continues, both the diameter of nanorod and its length grow reaching P point, where both GL and WZ phases can coexist. Further structure transformation foresees higher stability of nanorod in the WZ phase. Alongside with the structure transformation, an electric dipole moment appears associated with the WZ structure (it is zero for GL morphology). This dipole generates an electric field around the nanorod and the radicals, which are used during the synthesis procedure for the growth of AlN nanowires. Due to much larger electrostatic attractive forces, the incoming radicals are positioned on the top facets of nanorod and are barely able to have a chance to hit the sidewall [169]. In this way, the nanowire can grow along the [0001] direction with the unchanged diameter. This is described as the path $P \rightarrow Q$, which is perpendicular to the horizontal diameter axis (Fig. 6.58). Such understanding of the NW growth process suggests that in order to control the value of NW diameter, one must focus on the initial precursor, i.e., the GL nanorod structure [163]. To control effectively the first stage of growth, the WZ phase always must grow at the point P of the phase diagram, then uniform nanowires with the fixed diameter could be synthesized. Analogous mechanism was also suggested for the growth of GaN and ZnO nanowires [163, 170].

6.6.2 Thermal and Vibrational Properties of AlN Nanowires

Besides ab initio simulations on the structural and electronic properties of h- and w-AlN NW studied recently, as considered in previous Subsection [135, 157, 163–166], the attention was also directed towards their thermal, mechanical and vibrational properties [167]. The difference in nanostructure properties from those in bulk is caused by ultrathin nanowire diameters, which results in the physical reorganization of the atoms at lateral NW surface. For a high surface-to-volume ratio, the effects of the surface states are significant [164], effectively reducing the band gap, which has consequences in the optical absorption and electronic transport. Moreover, the AlN NWs experience a size-dependent phase transition WZ $\leftrightarrow$ GL as described above [163].

It is expected that thermal properties of nanowires are dramatically influenced whenever they are switched between different structural (phase) configurations [167]. Such transitions may occur due to the tensional or compressional stress caused by either thermal or mechanical perturbations, leading to the overall alteration of the whole system functionality. Therefore, further understanding in predicting the stress-induced phase transitions and revealing the consequences in thermal transport is needed. Such a characterization demands the analysis of the phonon spectrum $\hbar\omega(\mathbf{k})$. The corresponding ab initio approaches were firstly focused on Si nanowires (Sect. 5.3) concerning an atomistic approximation to thermoelectric properties [171] or a characterization of the Raman-active radial breathing mode [172]. The vibrational properties of CdSe nanowires were simulated when considering the WZ phase [173]. Experimental studies of local structural transitions and the phonon dynamics are generally pursued by means of Raman spectroscopy. The obtained results confirmed a size-dependent behavior of the phonon frequencies observed for GaAs NWs, especially for those associated with the surface modes [174]. Moreover, under the hydrostatic pressure, a transition from wurtzite to rock-salt phase was established for AlN nanowires [175].

After geometry optimization of AlN NW, the corresponding force constant matrix can be determined. To achieve the accurate results beyond Γ point phonons described by energy $\hbar\omega(k_z)$, a new supercell was assembled by joining three unit cells along the nanowire axis and further determination of the forces acting on each atom [167]. By displacing the atoms in the middle unit cell, the variations of forces (i.e., elements of the force constant matrix) around the equilibrium point were computed using the SIESTA package [176], which allows one to estimate the thermal conductance and specific heat. In the limit of low temperatures, assuming the nanowire length to be smaller than the phonon mean free path, one can neglect the mechanism of phonon scattering and employ Landauer's formalism adapted to thermal conduction in order to obtain the thermal conductance [177, 178]:

$$\kappa = \frac{\hbar}{2\pi k_B \mathrm{T}} \int_0^\infty \frac{e^{\hbar\omega/k_B \mathrm{T}}}{(e^{\hbar\omega/k_B \mathrm{T}} - 1)^2} \omega^2 \Theta(\omega) d\omega, \qquad (6.9)$$
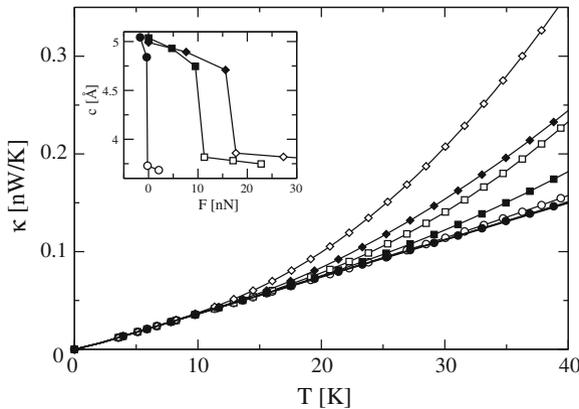
Fig. 6.59 Thermal conductance for AlN NWs under axial stress, for both WZ (*filled symbols*) and GL (*empty symbols*) phases and for different radii: $R1$ (*circles*), $R2$ (*squares*) and $R3$ (*diamonds*) as shown in Fig. 6.56. The *thick solid line* represents an ideal four-mode thermal conductance. The inset contains the variation of the lattice constant c with applied stress, indicating the transition points (Reprinted figure with permission from Mitran et al. [167], Copyright (2011) by the Elsevier B.V. All rights reserved)

where T is the temperature of the nanowire, k_B Boltzmann constant and ω phonon frequency, while $\Theta(\omega)$ represents the ballistic transmission function, which equals to the number of phonon modes at a given energy, in the case of the perfect NW structure, analogously to (5.5).

Figure 6.59 shows the thermal conductance of AlN NW at a low temperature. These data correspond to the applied pressures closest to the transition points (as shown in inset). For temperatures below $T_{ac} = 9\,\text{K}$ (when only the four acoustic modes have the major contribution to the thermal conductance), all the nanosystems converge towards the unique, almost linear dependence. Therefore, thermal conductance can be practically the same for both phases only below T_{ac}, a fact that may receive consideration in the design of the future electronic devices [167]. A value of T_{ac} is consistent with the frequency $\omega_{ac} \approx 200\,\text{cm}^{-1}$, for which the four acoustic modes are primarily occupied for both WZ and GL phases. With the temperature growth, the optical modes contribute to a thermal conductance and the behavior becomes differentiated: (i) the nanowires in the GL phase, which correspond to a higher applied pressure, have systematically higher conductance than their WZ counterparts, since the density of phonon modes is higher for the GL phase of the [0001]-oriented AlN NW (Fig. 6.60); (ii) the deviations from the declined straight line become larger with the NW size increase. Moreover, as the pressure is further enhanced beyond the transition point, the thermal conductance increases at a slower rate. Taking the $R2$ and $R3$ structures (Fig. 6.56) and applying 22.6 nN, the force necessary for reaching the GL phase is doubled, while the thermal conductance at 40 K increases to less than 3%. Obviously, at higher temperatures, the scattering mechanism plays a more important role, as the phonon mean free path decreases
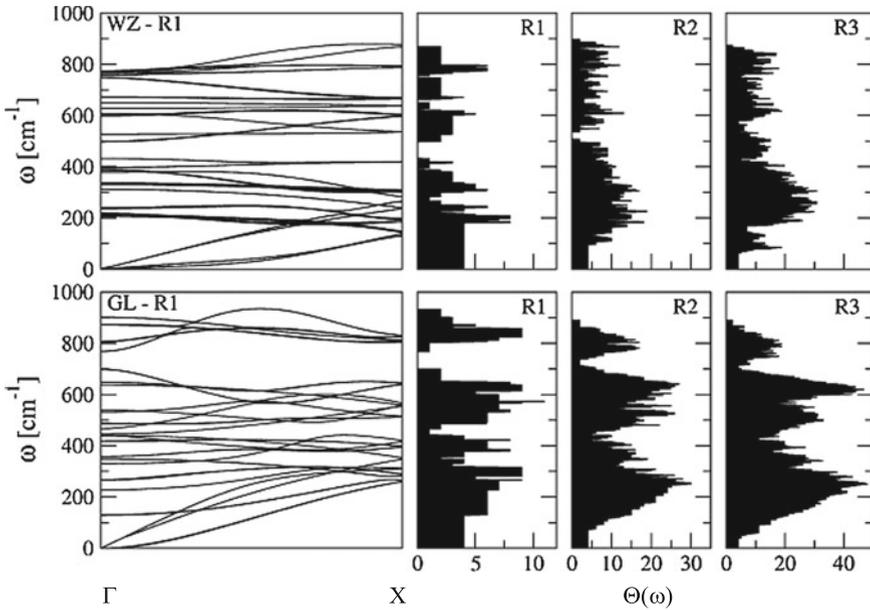
Fig. 6.60 The phonon band structure for $R1$-type AlN NW (Fig. 6.56) under stress applied for its WZ and GL phases. The phonon distributions of transmission function $\Theta(\omega)$, as defined in (6.9), are indicated for each nanowire structure [167]

[179], and the calculated curves overestimate the thermal conductance. The inset in Fig. 6.59 indicates the abrupt change in the lattice constant along the nanowire as pressure is applied, showing that the critical forces increase with the NW diameter. The quantifying behavior of the thermal conductance and heat capacity depending on NW sizes may be of crucial importance for the development of nanoscale low-temperature sensors [167]. Moreover, thermodynamical quantities that can be further derived may serve for modeling the synthesis process. In order to obtain the equilibrium configurations of AlN NWs considered in Fig. 6.56, their structures were completely relaxed [167]. This simulation step was crucial for obtaining reliable phonon dispersion curves (Fig. 6.60). The starting NW configurations were prepared in the WZ phase using bulk lattice parameters. Under no applied pressure, amongst the considered systems only the $R1$ type of nanowire changed its structure to the GL phase, which is consistent with the results obtained earlier [163], where it was argued that the GL formation energy at zero pressure is smaller. If a large enough pulling stress is applied ($\sim$0.37 nN) the $R1$ type nanowire retains the WZ structure. The NWs of larger diameter favor the morphology of WZ phase in their native, free-standing configurations. As a large enough compressive stress is applied to all nanowires, their configuration is switched to the unbuckled GL phase and the transition points are sensitive to the NW diameter. The calculated phonon spectrum of AlN NW in the direction X is presented in Fig. 6.60 for the $R1$ structure [167]. The two applied pressures ($F_{WZ} = 0.37$ nN and $F_{GL} = 0.21$ nN) correspond to the two phases with

different lattice constants of AlN NWs, namely, c_{GL} (3.72 Å) is considerably shorter than c_{WZ} (4.83 Å). The phonon spectrum of the aluminum nitride nanowire in the GL phase is shifted towards higher frequencies, which is the consequence of the packing, as compared to that of WZ phase. The acoustic modes were found to be essential in the description of the low temperature conductance. Altogether, there are four acoustic modes in phonon spectra of wurtzite-type nanowires: a dilatational mode, a torsional mode and two flexural modes [180]. The first two modes present a linear dispersion around the Γ point of the irreducible Brillouin zone, while the other two indicate a quadratic behavior. The maximum frequencies of the flexural modes were found to be $\omega_{WZ} = 142\,\mathrm{cm}^{-1}$ and $\omega_{GL} = 264\,\mathrm{cm}^{-1}$, which correspond to the X point in the IBZ, and are noticeably higher in the GL phase. Due to the different sizes of the IBZ in the $\Gamma \rightarrow X$ direction, resulting from the different lattice constants c_{WZ} and c_{GL}, one may conclude that there are larger average phonon group velocities of the flexural modes in the GL phase. A similar situation was observed for dilatational and rotational modes in the vicinity of the Γ point [167].

The transmission functions $\Theta(\omega)$ are also presented in Fig. 6.60 for all the considered nanowires. The GL phase introduces an overall larger phonon mode density. In particular, in the GL phase of the nanowire, there are optical modes with a lower energy as compared to the WZ case that enhance the transmission. For the $R1$ NW type, the minimum frequencies lie at $130\,\mathrm{cm}^{-1}$ and $180\,\mathrm{cm}^{-1}$ for the GL and WZ NWs, respectively, corresponding to the maximum frequencies for which $\Theta = 4$. The minimum frequency of the lowest optical modes decreases with the increasing AlN NW diameter of both structural configurations [167].

6.6.3 Elastic Properties of AlN Nanowires

Both types of hexagonal AlN NWs can be classified according to the number of circular layers in the nanowire consisting of both Al and N atoms (n_l) separated by the shortest distance d_{Al-N} (Fig. 6.61). Obviously, hexagonal nanowire consisting of n_l layers contains $N_n = 12n_l^2$ atoms *per* NW unit cell, while the number of atoms in the surface layer $N_{sn} = 12(2n_l - 1)$. Thus, the NW surface weight (in terms of the number of atoms) can be expressed as:

$$w_{sn} = \frac{2n_l - 1}{n_l^2}. \tag{6.10}$$

To simulate the elastic properties of AlN NWs, the elastic distortion of the nanowire was applied only along the NW axis, which was chosen to be the $z(3)$ axis [166]. To describe the energy of nanowire *per* atom, the simple additive model was developed:

$$e^{(NW)} = (1 - w_{sn})e^{(b)} + w_{sn}e^{(s)}, \tag{6.11}$$
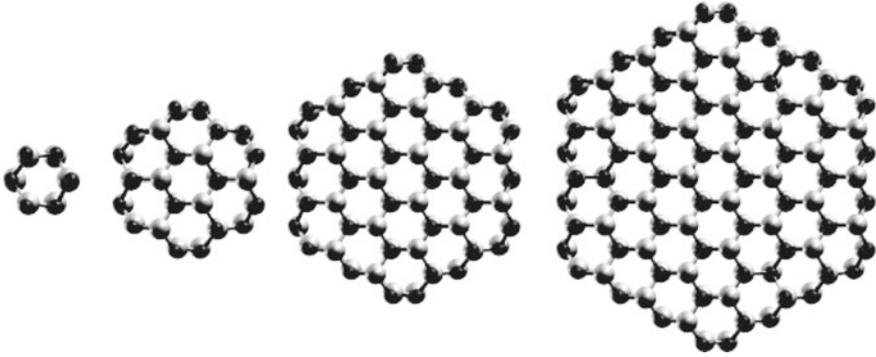
Fig. 6.61 Cross-sections of relaxed AlN nanowires with $n_l = 1, 2, 3$ and 4 (from *left* to *right*). Al and N atoms are shown as *gray* and *black*, respectively (Reprinted figure with permission from Mitrushchenkov et al. [166], Copyright (2010) by the IOP Publishing)

where w_{sn} is defined by (6.10), while $e^{(b)}$ and $e^{(s)}$ are the bulk and surface energies *per* atom of the same AlN phase as considered in the nanowire (as to the choice of the surfaces, it was determined by the facets terminating the nanowire) [166]. The energy contribution of bulk ($e^{(b)}$) was assumed to possess a uniform deformation in the *xy* plane ($\varepsilon_1 = \varepsilon_2$), while along the axis of periodicity (z), the elastic deformation of the nanowire was determined as ε_3. All shear deformations were set to zero. As the deformations were counted with respect to ideal bulk structure, there were no linear terms in bulk energy $e^{(b)}$ and only quadratic terms were present:

$$e^{(b)} = \frac{1}{2}\widetilde{C}_{11}^{(b)}\varepsilon_1^2 + \widetilde{C}_{13}^{(b)}\varepsilon_1\varepsilon_3 + \frac{1}{2}\widetilde{C}_{33}^{(b)}\varepsilon_3^2. \tag{6.12}$$

This expression was obtained from a classical definition of the elastic constants for ideal crystal with hexagonal structure ($C_{ij} = \frac{1}{V}\frac{\partial^2 E}{\partial \varepsilon_i \partial \varepsilon_j}$, where E is the calculated total energy *per* bulk unit cell, V its volume, which equals to $(a^2 c \sqrt{3})/2$, Fig. 6.55, while $i, j = 1, 2, \ldots, 6$), assuming that $\varepsilon_1 = \varepsilon_2$, which results in a certain transformation of the elastic constants: $\widetilde{C}_{11}^{(b)} = 2(C_{11}^{(b)} + C_{12}^{(b)})$, $\widetilde{C}_{13}^{(b)} = 2C_{13}^{(b)}$ and $\widetilde{C}_{33}^{(b)} = C_{33}^{(b)}$. With bulk cell parameters, the surface is not present in its relaxed state, therefore, the tension terms ($\tau_{ij} = \frac{1}{V}\frac{\partial E}{\partial \varepsilon_i}|_{\epsilon=0}$) should be also included in the expression of the surface energy, assuming that the surface is deformed when being relaxed [166]:

$$e^{(s)} = \frac{1}{2}\widetilde{C}_{11}^{(s)}\varepsilon_1^2 + \widetilde{C}_{13}^{(s)}\varepsilon_1\varepsilon_3 + \frac{1}{2}\widetilde{C}_{33}^{(s)}\varepsilon_3^2 + \tau_1^{(s)}\varepsilon_1 + \tau_3^{(s)}\varepsilon_3. \tag{6.13}$$

Within this simplified model, $x(1)$ deformations of volume and surface are the same. This is a quite natural assumption, especially for thick nanowires [166], as the surface must follow the deformation of the internal NW area. When applying the atomistic nanowire approximation, the surface can deform non-uniformly, especially close to the nanowire edges. Using the aforementioned additive model based

on (6.11–6.13), with bulk and surface parameters (deduced from the fitting of the slab calculations) and minimizing the energy e^{NW}, the nanowire elastic behavior and deformation were calculated as a function of the nanowire diameter [166]. The thickest nanowire calculated using the DFT-LCAO method corresponded to $n_l = 7$ and $d_{NW} = 3.74$ nm. The cross section of such nanowire contains 588 Al and N atoms *per* unit cell. To simulate elastic properties for AlN NWs possessing larger diameters ($\geq$10 nm), which were experimentally synthesized earlier [86, 153–156], both continuum and finite-element models were developed [168]. The latter (FEM), characterized by discretization of the nanowire lateral surface, well reproduces the non-uniformity in distribution of deformations in the vicinity of the surface, which was obtained using the first principles calculations.

For atomistic nanowire models described above, which can be treated using first principles methods, the two significant parameters to be determined are the elastic constants and the change of the relaxed NW UC length (l_{NW}) as compared to the bulk value, although these two quantities do not describe the internal relaxation in the nanowire. To look at this more deeply, the internal structure of fully relaxed nanowires was investigated [166]. The angular relaxation was found practically negligible, as well as the along-the-wire relative relaxation. The main effect was observed for the radial relaxation, which seemed to be practically unchanged in the internal part of AlN nanowire, while the surface effects were present in the surface and subsurface layers. Figure 6.62 presents the relative radial relaxation in AlN NW for both Al and N atoms. The relaxation of the surface NW layer was found to be $\sim$10 times larger than that in the internal NW area, thus, the surface atoms were forcedly omitted within the format of both plots, i.e., the surface effects presented in Fig. 6.62, actually correspond to the subsurface layer. According to Fig. 6.62, the internal area of AlN NW is homogeneously expanded in the same way for both types of atoms, so that it does behave
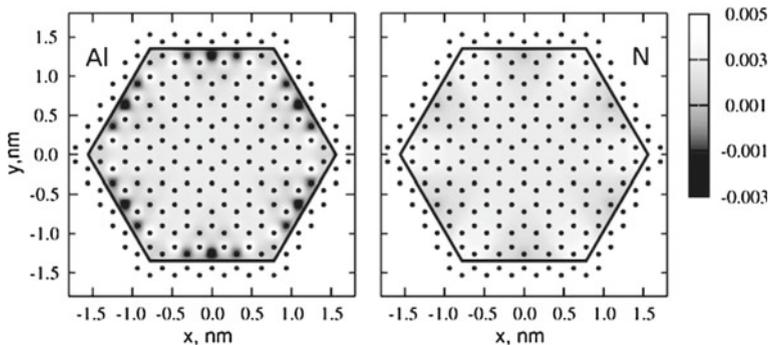
Fig. 6.62 Radial deformations in AlN NWs with the $n_l = 6$ using bulk value of c parameter (Fig. 6.55) for atoms of Al (*left panel*) and N (*right panel*). Coordinates are given in nanometers (for the center of NW, $x = y = 0$). *Thick lines* represent the ideal NW diameter $d(n_l) = 2(n_l - 1)a$ (which is expressed via a parameter of bulk) corresponding to the volume of the internal (excluding the surface) area of the nanowire. The ideal (*bulk*) positions of atoms are shown by *small filled circles* (Reprinted figure with permission from Mitrushchenkov et al. [166], Copyright (2010) by the IOP Publishing)

as an isotropic bulk crystal. The relaxation around the NW center can be taken as the macroscopic parameter which should be reproduced by the NW elastic model. Cross-sectional elastic deformations were defined as $\varepsilon_{rel}^{NW} = \frac{r-r_0}{r_0}$, where r is the relaxed radial distance of a given atom from the NW axis, and r_0 the unrelaxed (bulk) value.

Similar simulations were performed also for AlN(0001) slab system containing the same number of layers between the two external surfaces as in the case of AlN nanowire (Fig. 6.62). Figure 6.63 presents the comparison of the internal relaxation parameters of the NW described by $n_l = 6$ and the corresponding slab ($n_l = 12$). For a correct comparison between these parameters, the along-the-nanowire cell parameter c was fixed to its bulk value, and all other parameters were fully relaxed. For the plotted slab data, the values of relative deformations along the in-plane $y(2)$ axis were chosen: $\varepsilon_{rel}^{slab} = \frac{y-y_0}{y_0}$. The same parameter was plotted for NW: in this case, y axis corresponds to the vertical direction in Fig. 6.62. As a result, the following conclusions were drawn [166]:

 (i) while the nanowire is uniformly expanded under the free relaxation, the slab system is mostly compressed by the similar amount;
 (ii) surface effects are negligible for nanowires below two external layers, while for slab systems, long-range anisotropic effects exist far away from the surface, thus, the internal area of the slab does not behave like homogeneous isotropic media, but rather has deformations alternating between the adjacent atomic layers;
(iii) the surface is slightly less flat in nanowires as compared to a slab system of the same width.

On the whole, the anisotropy of slab elasticity could be easily understood as a consequence of the surface anisotropy. However, six differently oriented facets of
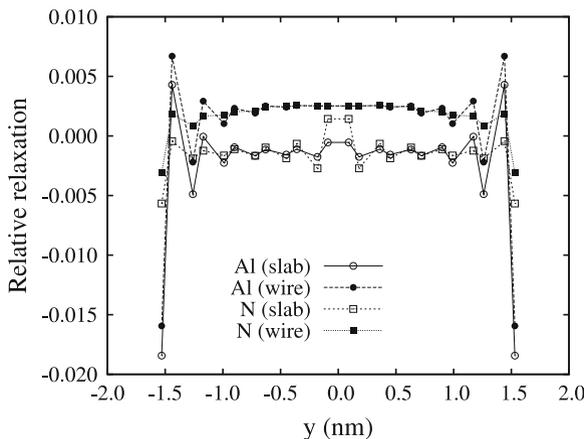
Fig. 6.63 Plots of functions $\varepsilon_{rel}(y)$ for AlN NW ($n_l = 6$) and the corresponding AlN(0001) slab ($n_l = 12$). Inset presents the labels of *elastic curves* for Al and N atoms forming nanowire and slab (Reprinted figure with permission from Mitrushchenkov et al. [166], Copyright (2010) by the IOP Publishing)

AlN NW substantially reduce their anisotropy, especially in the internal NW area leading to its isotropic behavior. Thus, one could expect that the surface parameters obtained from the slab calculations need to be somehow adjusted to the properly described nanowires [166]. This was a possible way to avoid difficulties with the definition of the nanowire diameter and UC volume when performing first principles calculations: to slightly adjust the surface parameters obtained from the slab calculations, in order to accurately reproduce elastic behavior of the calculated nanowires. For example, using bulk parameters and adjusted surface parameters of AlN, one could minimize the energies $e^{(NW)}$, $e^{(b)}$ and $e^{(s)}$ relatively to elastic deformations ε_1 and ε_3, as defined by (6.11)–(6.13). (In practice, the C_{33} and τ_3 constants are quite different for the bulk and surface, therefore they need adjustment, the same as τ_1, which is quite sensitive to the surface structure; however, C_{11} could be fixed as for bulk). Dependence on the NW surface weight w_{sn} defined by (6.10) could provide simple analytic expressions for $\varepsilon_r^{rel}(w)$, $\varepsilon_3^{rel}(w)$, and $C_{33}^{rel}(w)$ based on the results of ab initio calculations [166] as shown in Fig. 6.64.

Obviously, the approaches with initial slab parameters could reproduce the Young's modulus (correlated with C_{33}^{rel} value since for neglecting the along-wire strain, $C_{33}^{rel} = C_{33}^{(b)}|_{\epsilon_3=0}$ [166]) and the radial xy deformation (ε_r^{rel}), but this is not true for the along-wire z relaxation (ε_3^{rel}), which is indeed a sensible parameter. However, the adjusted surface parameters corresponding to the model can well reproduce the calculated ab initio values. The largest deviations from the simple approach correspond to the point $n_l = 3$, because the nanowire in that case is, certainly, too thin, and equals $n_l = 7$, most likely because of the lower accuracy of ab initio calculations on polyatomic systems of larger sizes [166]. The coefficients adjusted within the atomistic model can be transformed into standard *per*-volume (in GPa) and *per*-surface (in Nm^{-1}) parameters which are used in the FEM model mentioned above [168]. Obviously, this approach can be applied to nanowires of a larger diameter where ab initio calculations are no longer possible. Also, it opens up prospects for future simulations, e.g., application of this approach to a variety of other NW types, including non-hexagonal ones.
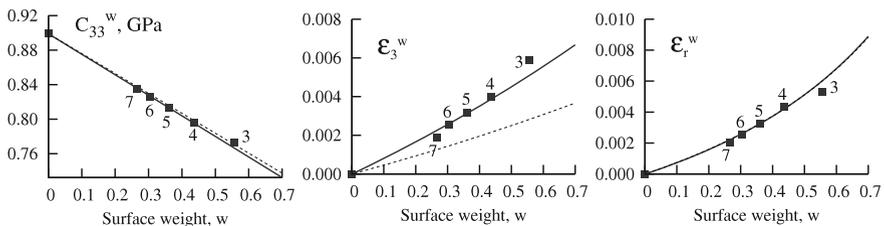
Fig. 6.64 The results obtained for atomistic first principles simulations on elastic parameters plotted as functions of surface weight. Ab initio results for nanowires are marked with square dots and numbers corresponding to the value of n_l. The bulk system corresponds to $w_{sn} = 0$. *Dashed* and *solid lines* correspond to the initial and adjusted surface parameters, respectively (Reprinted figure with permission from Mitrushchenkov et al. [166], Copyright (2010) by the IOP Publishing)

6.6.4 Prismatic GaN Nanowires and Their Elasticity

Due to the proximity among a considerable number of properties for AlN and GaN bulk, low-index densely-packed surfaces and buckled honeycomb-type nanotubes (except for a large difference between their band gaps: 6.2 vs. 3.5 eV in bulk, respectively [104]), most nanowire properties for both nitride compounds have to be qualitatively similar. This is why the current Subsection is devoted to the discussion of mainly those results that were not presented in the previous Subsections, e.g., atom-centered GaN NWs possessing triangular-type shaped cross-sections [181, 182] (for AlN, mainly hollow-centered hexagonal shaped NW models have been considered so far); (ii) H-terminated GaN nanowires and the comparison of their properties with those of clean GaN NWs (hydrogenation of their lateral facets was found to be energetically advantageous, due to a higher reactivity of dangling bonds [182, 183]); (iii) a simplified approach to estimate the NW elasticity [181]. Routine description of the calculated geometry and electronic structure, analogous to that reported for AlN NWs [135, 157, 164], was given for GaN NWs as well [169, 182, 184]. Moreover, ab initio simulations were performed for several types of defective GaN NWs containing either point vacancies [185, 186] or dopants substituted native atoms [187, 188], the electronic and magnetic properties of which could be regulated when changing the point defect concentration. For simulations of GaN nanowires, infinite (1D) models were mainly applied (e.g., periodic nanorod [169]), and for their calculations, the following methods were used: DFT-LCAO [181–184, 186], DFT-PW [169, 185, 187, 188] and MD [169]. In the experimental studies of GaN NW synthesis, mainly wurtzite morphology of nanowires was observed [189–191], although they were also reported in the zinc blende structure as obtained in conditions of synthesis at elevated temperatures in the presence of free Ga^+ ions [192]. The diameters of synthesized nanowires typically ranged from 5 to 100 nm [193, 194]. A few different GaN NW growth directions were also reported, e.g., [0001] [189, 191], $\{10\bar{1}0\}$ [195, 196] and $\{11\bar{2}0\}$ [191, 196]. The majority of synthesized GaN nanowires, especially [0001]-oriented, typically formed hexagonal shapes of cross-sections [197], although in nanowires with $\{11\bar{2}0\}$ direction of the NW axis, triangularly shaped forms were observed as well [198]. In some experiments, the growth of GaN NWs was accompanied by the presence of hydrogen species, which saturated their lateral facets, thus, making nanowires energetically more stable [183, 199]. GaN NWs with internal *p–n* junctions were fabricated through incorporation of Mg dopants [200], while Mn-doped GaN NWs displayed a ferromagnetic behavior already at room temperature [201].

In a comprehensive first-principles study of the atomic and electronic structures of various gallium nitride nanowires (Fig. 6.65), their dependence on the NW shape and diameter as well as the influence of facet hydrogenation were examined [182]. All nanowires imaged in Fig. 6.65 possess a family of lateral $\{10\bar{1}0\}$ facets, the surface energy of which is lower as compared to the $\{11\bar{2}0\}$ surface (118 vs. 123 meV/Å^2, respectively) [151], i.e., $\{10\bar{1}0\}$ NW faceting is energetically more preferable, similar to the same hierarchy observed for AlN NW facets as considered in Sect. 6.5.1 (Fig. 6.53). Triangular- and hexagonal-shaped GaN NWs imaged in Fig. 6.65 can be

(a)   **(b)**

48   108   26   66
(9.5 Å)   (15.9 Å)   (6.3 Å)   (12.7 Å)

132   160   300   92   194
(19.7 Å) (21.0 Å)   (28.6 Å)   (15.9 Å)   (25.5 Å)
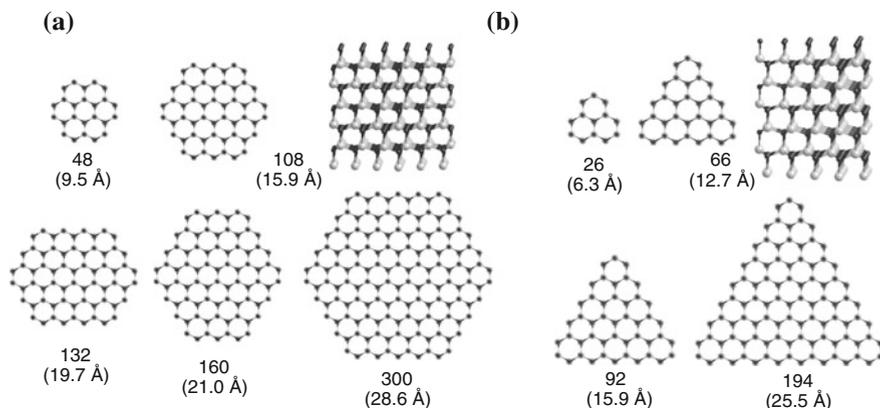
Fig. 6.65 Cross-sections and aside views of [0001]-oriented GaN NWs of different sizes and shapes (A is hexagonal and B triangular ones). The number of atoms per UC and diameters (in parentheses) are labeled for each model. N and Ga atoms are indicated as *dark* and *light balls*, respectively [182]

described by different rod groups: $P3m1$ and $P6_3mc$, respectively (except the two nanowires containing 132 and 160 atoms per UC, the cross-sections of which form distorted hexagons with either elongated or shrank contours regarding the x axis directed across NW).

Analogically to AlN NWs, Ga-N bonds were found essentially compressed at unsaturated aside nanowire facets (6.0–7.0 %) as compared to those in GaN bulk (2.01 Å) [169, 182, 183, 187] and at the center of GaN nanowires (which were contracted only by ∼0.6 %). The GaN $\{10\bar{1}0\}$ slab was also reported to possess values of d_{Ga-N} decreased by ∼6 % as compared to bulk [151]. With the increasing d_{NW}, the averaged value of d_{Ga-N} also increased (as can be expected) slowly approaching the bond length in bulk [182].

The saturation of dangling bonds of GaN nanowires with hydrogen resulted in the appearance of Ga-H and N-H quasi-bonds upon the NW facets [183]. (Sect. 5.2.2 contains, for comparison, across and aside images showing the hydrogen atom distribution upon faceted Si NTs.) For a single H atom, the calculated energies of bonding with nanowires were found to be 2.99 eV for the N-H bond ($d_{N-H} \approx 1.04$ Å) and 1.63 eV for the Ga-H bond ($d_{Ga-H} \approx 1.04$ Å). This was in a good agreement with the corresponding values obtained earlier for a hydrogenated GaN surface [202]. When comparing d_{Ga-H} calculated for both H-saturated and unsaturated nanowires, these bond lengths changed qualitatively in a similar way, although d_{Ga-H} values of the former were found to be substantially smaller [182]. For example, in a H-passivated GaN nanowire, the contraction of Ga-N bonds parallel to its [0001] axis achieved 1.0–1.7 % at the NW edge and less than 0.2 % at the NW center. Figure 6.66 presents the band structures for unsaturated GaN nanowires of diameters selected as either "small" or "large" and possessing either hexagonal or triangular shapes (although qualitatively similar results were obtained for all the other NW models shown in Fig. 6.65), which were calculated using the DFT-LCAO method [182]. It is evident
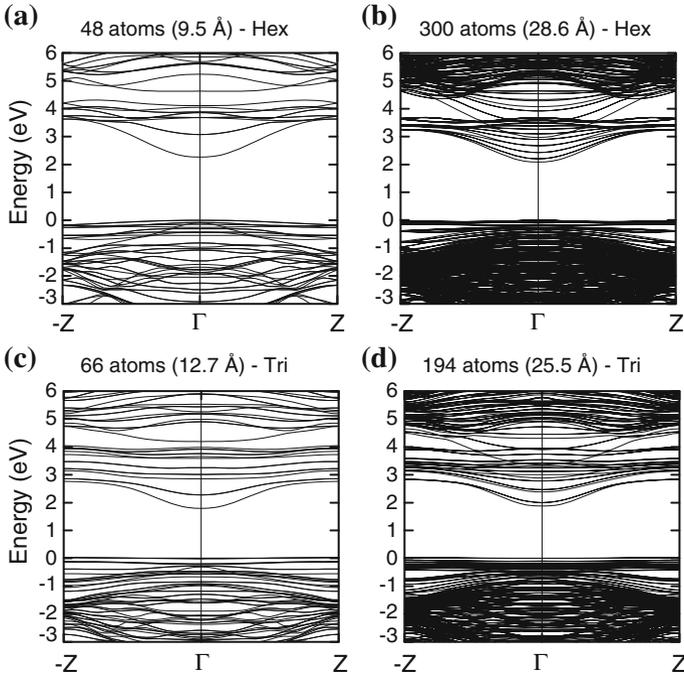
Fig. 6.66 The band structures for unsaturated GaN NWs of different diameters and shapes. The energy zero is set at the highest occupied level (VBM). "Hex" and "Tri" represent *hexagonal* and *triangular* shapes of nanowires, respectively [182]

that the corresponding NW dangling bonds produce the edge-induced states (bands) in the band gaps located above the valence band maximum (VBM) and below the conduction band minimum (CBM). The band gap of unsaturated GaN nanowires, i.e., the gap between both edge-induced states, is not changed significantly with the growth of the nanowire diameter since they are quite well localized. The analysis of the calculated total and projected DOSs for GaN nanowires of different diameters and shapes [182] clearly showed that Ga($3p$) orbitals predominantly contribute to the edge states that appear near and below the CBM while N($2p$) orbitals contribute to the edge states appearing at and above the VBM in the band structure plots as shown in Fig. 6.66.

Figure 6.67 presents the band structures for H-saturated GaN nanowires possessing the same diameters and shapes as considered in Fig. 6.66. When NWs were saturated with hydrogen atoms, the dangling bonds disappeared, i.e., the bands attributed to them were found to be from the nanowire band gap, thus, $\Delta\epsilon_{gap}^{satur} > \Delta\epsilon_{gap}^{unsatur}$. It means that the hydrogen atoms have a stabilizing effect on the bonding molecular orbitals pushing the anti-bonding molecular orbitals up. Such a behavior is typical for both the small and large nanowires of both hexagonal and triangular shapes [182].
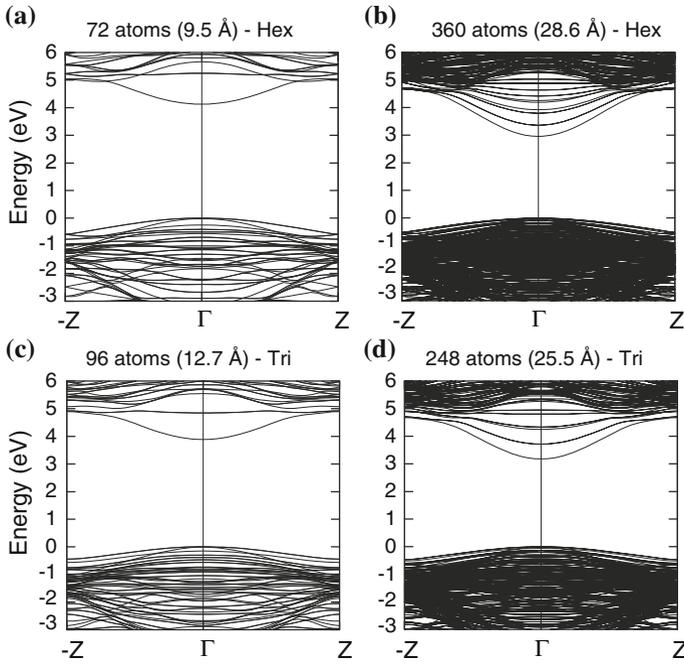
Fig. 6.67 The band structures for H-saturated GaN NWs of different diameters and shapes. Other details of presented plots are described in caption of Fig. 6.66 [182]

Fig. 6.68 Relative band gap as a function of nanowire diameter as calculated using the DFT-LCAO method. Values of $\Delta\epsilon_{gap}$ are relative to the calculated bulk GaN band gap [182]
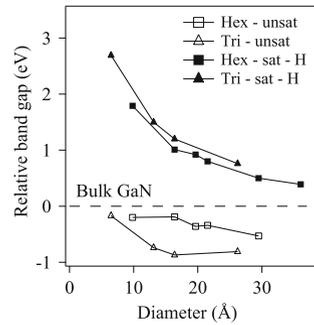
Moreover, the band gap of H-saturated GaN nanowires noticeably decreased with the increasing d_{NW}, unlike unsaturated NWs (Fig. 6.66).

The calculated band gaps as a function of the NW diameter, i.e., $\Delta\epsilon_{gap}(d_{NW})$, for hexagonal and triangular nanowires are shown in Fig. 6.68 [182]. For H-saturated nanowires, the essential decrease of $\Delta\epsilon_{gap}$ with the growing diameter eventually approaches the bulk band gap values. For unsaturated nanowires, a little change in the band gaps with the increasing diameter was found, illustrating the influence of the

localized edge-like dangling bond states in the band gap, as mentioned previously. For the unsaturated NWs, the band gaps of triangular nanowires were noticeably smaller than of hexagonal nanowires; however, for H-saturated NWs, this trend was reversed, although the difference was found to be much smaller [182]. For the given effective value of d_{NW}, the triangular and hexagonal nanowire calculations contained slightly different numbers of GaN units, so when examining the band gap as a function of the number of atoms, the band gaps of H-saturated hexagonal- and triangular-shaped NWs look similar (Fig. 6.68). However, for the unsaturated nanowires the trend remains, with the band gap being consistently smaller for the triangular NWs, which could be explained by both a smaller stability of triangular NWs and a higher energy of the occupied edge-induced states, as compared to the hexagonal nanowires [182]. The energetic stability of nanowires possessing different diameters and shapes is directly correlated with their formation energy E_{form}: the smaller is d_{NW}, the higher the energy. To estimate E_{form} *per* atom for unsaturated GaN NWs, (6.8) could be slightly modified since that energy for AlN NW was defined *per* Al-N bond [164], while for a H-saturated nanowire, the definition of the formation energy should contain the member describing the hydrogen atom [182]:

$$E_{form}(d_{NW}) = [E_{tot}(n_{GaN}) - n_{GaN}\mu_{Ga} - 0.5n_{GaN}\mu_N]/2n_{GaN}, \qquad (6.14)$$

$$E_{form}(d_{NW}) = [E_{tot}(n_{GaN}, n_H) - n_{GaN}\mu_{Ga} - 0.5n_{GaN}\mu_N$$
$$- n_H\mu_H]/(n_{GaN} + n_H), \qquad (6.15)$$

where n_{GaN} and n_H are the numbers of GaN pairs and H atoms *per* NW unit cell, E_{tot} the calculated total energy of the saturated GaN nanowire, μ_{Ga}, μ_N and μ_H the chemical potentials of Ga, N and H obtained from energies of the Ga atom in the face-centered cubic metal and isolated N_2 and H_2 molecules, respectively.

The formation energies per atom for unsaturated and saturated nanowires as functions of the nanowire diameter, according to definitions given in (6.14) and (6.15), are presented in Fig. 6.69. The corresponding energy curves show the increasing NW stability with the growth of d_{NW} approaching the stability found in bulk GaN [182]. Obviously, the hexagonal nanowires are slightly more stable than triangular nanowires of the same size, although when all dangling bonds were saturated, the

Fig. 6.69 Relative formation energy *per* atom as a function of d_{NW} for [0001]-oriented unsaturated and H-saturated GaN NWs. Energies are relative to the heat of formation *per* atom of GaN bulk. Other details of the presented plots are described in the caption of Fig. 6.66 [182]

(W116)   (W122)   (W146)
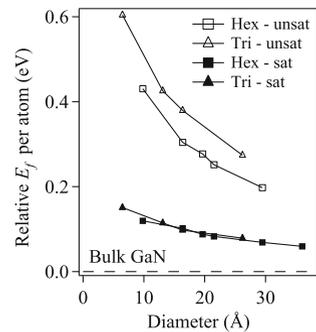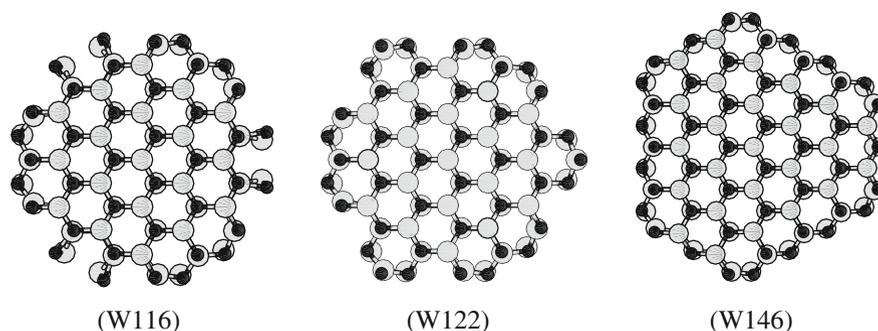
Fig. 6.70 Cross-sections of GaN nanowires considered for study of their elastic properties. The growth direction is normal to the plane of NW images. A number behind the W gives the number of atoms in NW unit cell (Reprinted figure with permission from Gulans and Tale [181], Copyright (2007) by the WILEY-VCH Verlag GmbH & Co. KGaA, Weinheim)

local bonding environment appears to be very similar to both the hexagonal- and triangular-shaped NWs with a slight priority for the former. This could be explained by the fact that for the same number of atoms, the triangular nanowires have a slightly greater circumference number of dangling bonds compared to the corresponding hexagonal nanowires. Thus, the former always experience a slightly smaller degree of "real" GaN environment as compared to the latter.

Three alternative models of atom-centered [0001]-oriented GaN nanowires with quasi-hexagonal shapes were considered (Fig. 6.70), all described by $P3m1$ rod group and containing different number of atoms per NW unit cells [181]. The first two models were terminated by alternating $\{10\bar{1}0\}$ and $\{11\bar{2}0\}$ lateral facets, while W146 NW contained only non-polar facets. W116 NW corresponds to the roundest shape amongst all three models.

The surface energies of these nanowires per formula unit were calculated using the DFT-LCAO method [181]. The high value of surface energy for W116 (0.91 eV) is not surprising due to the presence of the external atoms with two dangling bonds so that the overall number of dangling bonds is very high. In contrast, W146 had the smallest energy (0.58 eV) being energetically most preferable. The average surface energy *per* dangling bond turned out to be similar in all cases. The differences could be explained by the peculiarities of the environments for surface atoms. Since most of the surface atoms in these nanowires possess similar neighborhoods as compared to $\{10\bar{1}0\}$ and $\{11\bar{2}0\}$ slabs, some qualitative similarities were observed also between the calculated properties and electronic structures of the faceted NWs and slabs [181]. Therefore, slabs of 10 atomic layers were constructed, which was found to be enough to ensure the convergence of the surface energy and atomic relaxations with the corresponding nanowires, in order to perform slab studies instead of time- and space-consuming NW calculations that decrease computational expenses significantly. Taking into account the difference between elastic properties of the surface and core round atomic layers in nanowires, as considered in previous Subsection, a simple model for nanowire elasticity was proposed [181]. For this aim, the total energy of a nanowire per unit

cell was expressed as the sum of bulk and surface contributions:

$$E_{tot} = E_{bulk} + E_{surf} = n_b E_b + \sum_i n_{si} E_{si}, \qquad (6.16)$$

where E_{bulk} is expressed using the total energy E_b of bulk crystal *per* formula unit and the number n_b of formula units in the considered unit cell. The remaining part of the total energy is the surface energy E_{surf} expressed as the sum of E_{si} contributions from n_{si} atoms belonging to different surface types (i), for example, $\{10\bar{1}0\}$ and $\{11\bar{2}0\}$. For the quantitative estimate of w-GaN elastic parameters, the energies E_b and E_{si}, were approximated by the second order polynomial expression [181]:

$$E_k(a, c) = \alpha_k(a - a_{0k})^2 + \beta_k(c - c_{0k})^2 + \gamma_k(a - a_{0k})(c - c_{0k}), \qquad (6.17)$$

where k is either b or si, α_k, β_k, γ_k are elastic tensor elements, while a_{0k} and c_{0k} equilibrium lattice constants in bulk, which were determined either from bulk or surface calculations. Knowing the explicit expression for the terms in (6.16), Young's modulus for a nanowire could be estimated by a double differentiation of the total energy E_{tot} [181]:

$$E_Y = \frac{c_0}{S_0} \frac{d^2 E_{tot}}{dc^2}, \qquad (6.18)$$

where S_0 is the cross section area and c_0 is the equilibrium value of NW unit cell length.

The dependence of Young's modulus versus d_{NW} calculated for hollow-centered hexagonal shaped nanowires with facets of equal sizes (Fig. 6.61) is shown in Fig. 6.71. To determine the second derivative of the total energy and to obtain
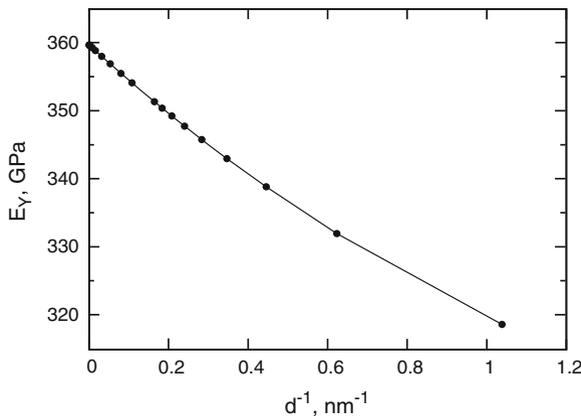
Fig. 6.71 Size dependence of the Young's modulus E_Y in *hexagonally-shaped* GaN nanowires (Reprinted figure with permission from Gulans and Tale [181], Copyright (2007) by the WILEY-VCH Verlag GmbH & Co. KGaA, Weinheim)

the Young's modulus according to (6.18), a set of constants obtained for each surface and bulk were calculated by varying GaN lattice constants and performing quadratic fit [181]. The constants obtained for bulk corresponded to the elastic moduli $C_{11} + C_{12} = 492$, $C_{33} = 403$, and $C_{13} = 103$ GPa, which were in a reasonable agreement with the experimental values based on the averages of consistent measurements ($C_{11} + C_{12} = 516$, $C_{33} = 389$, and $C_{13} = 98$ GPa [203]). The results of the performed calculations on elastic properties of GaN nanowires qualitatively reproduced bulk limit of the Young's modulus and confirmed the NW softening with the decrease of d_{NW} observed elsewhere [204]. So far, gallium nitride nanowires have covered a wider spectrum of technological applications as compared to AlN NWs, being one of the most promising building blocks in nanotechnologies related to UV-blue LEDs, detectors, lasers, high temperature and/or high power devices, as well as to potential spintronic devices [190, 205].

References

1. R. Haubner, M. Wilhelm, R. Weissenbacher, B. Lux, *High Performance Non-oxide Ceramics II, Series, Structure and Bonding*, vol. 102 (Springer, Berlin, Heidelberg, New York, 2002), pp. 1–45
2. P.B. Mirkarimi, K.F. McCarty, D.L. Medlin, Mater. Sci. Eng. R **21**, 47 (1997)
3. R.A. Evarestov, Yu.F. Zhukovskii, A.V. Bandura, S. Piskunov, J. Phys. Chem. C **114**, 21061 (2010)
4. T.E. Mosuang, J.E. Lowther, J. Phys. Chem. Solids **63**, 363 (2002)
5. K. Watanabe, T. Taniguchi, H. Kanda, Nat. Mater. **3**, 404 (2004)
6. J. Furthmüller, J. Hafner, G. Kresse, Phys. Rev. B **50**, 15606 (1994)
7. A. Lichanot, P. Azavant, U. Pietsch, Acta Crystallogr. B **52**, 586 (1996)
8. X. Blasé, A. Rubio, S.G. Louie, M.L. Cohen, Europhys. Lett. **28**, 335 (1994)
9. N.G. Chopra, R.J. Luyken, K. Cherrey, V.H. Crespi, M.L. Cohen, S.G. Louie, A. Zettl, Science **269**, 966 (1995)
10. D. Golberg, Y. Bando, M. Eremets, K. Takemura, K. Kurashima, H. Yusa, Appl. Phys. Lett. **69**, 2045 (1996)
11. A. Loiseau, F. Willaime, N. Demoncy, G. Hug, H. Pascard, Phys. Rev. Lett. **76**, 4737 (1996)
12. E. Bengu, L.D. Marks, Phys. Rev. Lett. **86**, 2385 (2001)
13. R. Czerw, S. Webster, D.L. Carroll, S.M.C. Vieira, P.R. Birkett, C.A. Rego, S. Roth, Appl. Phys. Lett. **83**, 1617 (2003)
14. D. Golberg, M. Mitome, Y. Bando, C.C. Tang, C.Y. Zhi, Appl. Phys. A **88**, 347 (2007)
15. V.L. Kuznetsov, I.N. Mazov, A.I. Delidovich, E.D. Obraztsova, A. Loiseau, Phys. Status Solidi (B) **244**, 4165 (2007)
16. E. Perim, D.S. Galvão, Nanotechnology **20**, 335702 (2009)
17. S. Guerini, V. Lemos, P. Piquini, Nanotechnology **17**, 556 (2006)
18. X. Blasé, A. De Vita, J.C. Charlier, R. Car, Phys. Rev. Lett. **80**, 1666 (1998)
19. P.W. Fowler, K.M. Rogers, G. Seifert, M. Terrones, H. Terrones, Chem. Phys. Lett. **299**, 359 (1999)
20. T. Dumitrică, H.F. Bettinger, G.E. Scuseria, B.I. Yakobson, Phys. Rev. B **68**, 085412 (2003)
21. Y.H. Kim, K.J. Chang, S.G. Louie, Phys. Rev. B **63**, 205408 (2001)
22. S. Okada, S. Saito, A. Oshiyama, Phys. Rev. B **65**, 165410 (2002)
23. D. Sánchez-Portal, E. Hernández, Phys. Rev. B **66**, 235415 (2002)
24. V.N. Popov, Phys. Rev. B **67**, 085408 (2003)

25. L. Wirtz, A. Rubio, R. Arenal, A. Loiseau, Phys. Rev. B **68**, 045425 (2003)
26. H.J. Xiang, J. Yang, J.G. Hou, Q. Zhu, Phys. Rev. B **68**, 035427 (2003)
27. W.H. Moon, H. Hwang, Physica E **23**, 26 (2004)
28. S.H. Jhi, D.J. Roundy, S.G. Louie, M.L. Cohen, Solid State Commun. **134**, 397 (2005)
29. L. Wirtz, M. Lazzeri, F. Mauri, A. Rubio, Phys. Rev. B **71**, 241402 (2005)
30. F. Zheng, G. Zhou, S. Hao, W. Duan, J. Chem. Phys. **123**, 124716 (2005)
31. H. Liu, G. Zhou, Q. Yan, J. Wu, B.L. Gu, W. Duan, D.L. Zhao, Phys. Rev. B **75**, 125410 (2007)
32. S. Guerini, V. Lemos, P. Piquini, S.S. Coutinho, Phys. Status Solidi (B) **244**, 110 (2007)
33. S. Hao, G. Zhou, W. Duan, J. Wu, B.-L. Gu, J. Am. Chem. Soc. **130**, 5257 (2008)
34. H. Pan, Y.P. Feng, J. Lin, Nanotechnology **19**, 095707 (2008)
35. Y.M. Chou, H.W. Wang, Y.J. Lin, W.H. Chen, B.C. Wang, Diam. Relat. Mater. **18**, 351 (2009)
36. P.N. Dyachkov, D.V. Makaev, J. Phys. Chem. Solids **70**, 180 (2009)
37. Y. Kinoshita, S. Hase, N. Ohno, Phys. Rev. B **80**, 125114 (2009)
38. S. Riikonen, A.S. Foster, A.V. Krasheninnikov, R.M. Nieminen, Phys. Rev. B **80**, 155429 (2009)
39. Yu.F. Zhukovskii, S. Piskunov, N. Pugno, B. Berzina, L. Trinkler, S. Bellucci, J. Phys. Chem. Solids **70**, 796 (2009)
40. Yu.F. Zhukovskii, S. Bellucci, S. Piskunov, L. Trinkler, B. Berzina, Eur. J. Phys. B **67**, 519 (2009)
41. R.K.F. Lee, B.J. Cox, J.M. Hill, Nanoscale **2**, 859 (2010)
42. R.A. Evarestov, Yu.F. Zhukovskii, A.V. Bandura, S. Piskunov, M.V. Losev, J. Phys. Chem. C **115**, 14067 (2011)
43. W.Q. Han, in *Mixed Metal Nanomaterals*, ed. by Ch. Kumar (Wiley-VCH, Weinheim, 2009), pp. 411–462
44. R. Arenal, X. Blasé, A. Loiseau, Adv. Phys. **59**, 101 (2010)
45. R.A. Jishi, M.S. Dresselhaus, G. Dresselhaus, Phys. Rev. B **47**, 16671 (1993)
46. R. Saito, G. Dresselhaus, M.S. Dresselhaus, *Physical Properties of Carbon Nanotubes* (Imperial College Press, London, 1998)
47. O. Dubay, G. Kresse, Phys. Rev. B **67**, 035401 (2003)
48. D. Bogdan, R. Isai, A. Calborean, C. Morari, Physica E **44**, 1441 (2012)
49. J. von Neumann, E. Wigner, Physica Z **30**, 67 (1929)
50. P. Umari, A. Pasquarello, A. Dal Corso, Phys. Rev. B **63**, 094305 (2001)
51. O.E. Alon, Phys. Rev. B **64**, 153408 (2001)
52. F. Ding, K. Bolton, A. Rosén, J. Phys. Chem. B **108**, 17369 (2004)
53. Q.M. Zhang, J.C. Wells, X.G. Gong, Z. Zhang, Phys. Rev. B **69**, 205413 (2004)
54. J. Zhao, A. Martinez-Limia, P.B. Balbuena, Nanotechnology **16**, S575 (2005)
55. S. Reich, L. Li, J. Robertson, Phys. Rev. B **72**, 165423 (2005)
56. M. Cantoro, S. Hofmann, V. Scardaci, A. Parvez, S. Pisana, C. Ducati, A. Blackburn, A.C. Ferrari, J. Robertson, Nano Lett. **6**, 1107 (2006)
57. Y.A. Zhu, Y.C. Dai, D. Chen, W.K. Yuan, Surf. Sci. **601**, 1319 (2007)
58. N.I. Alekseev, N.A. Charykov, Russ. J. Phys. Chem. A **82**, 2191 (2008)
59. F. Ding, P. Larsson, J.A. Larsson, R. Ahuja, H. Duan, A. Rosén, K. Bolton, Nano Lett. **8**, 463 (2008)
60. O.V. Yazyev, A. Pasquarello, Phys. Rev. Lett. **100**, 156102 (2008)
61. H. Amara, J.M. Roussel, C. Bichara, J.P. Gaspard, F. Ducastelle, Phys. Rev. B **79**, 014109 (2009)
62. A. Börjesson, W. Zhu, H. Amara, C. Bichara, K. Bolton, Nano Lett. **9**, 1117 (2009)
63. Yu.F. Zhukovskii, S. Piskunov, E.A. Kotomin, S. Bellucci, Cent. Eur. J. Phys. **9**, 539 (2011)
64. N. Grobert, Mater. Today **10**, 28 (2007)
65. B.J. Wang, V.K. Kayastha, Y.K. Yap, Z. Fan, J.G. Lu, Z. Pan, I.N. Ivanov, A.A. Puretzky, D. Geohegan, Nano Lett. **5**, 2528 (2005)
66. M.J. López, A. Rubio, J.A. Alonso, L.C. Qin, S. Iijima, Phys. Rev. Lett. **86**, 3056 (2001)
67. M.H.F. Sluiter, Y. Kawazoe, Phys. Rev. B **69**, 224111 (2004)

68. A.B. Dalton, S. Collins, E. Muoz, J.M. Razal, V.H. Ebron, J.P. Ferraris, J.N. Coleman, B.G. Kim, R.H. Baughman, Nature **423**, 703 (2003)
69. D. Golberg, Y. Bando, Appl. Phys. Lett. **79**, 415 (2001)
70. C.W. Chen, M.H. Lee, S.J. Clark, Nanotechnology **15**, 1837 (2004)
71. A. Celik-Aktas, J.M. Zuo, J.F. Stubbins, C. Tang, Y. Bando, Acta Cryst. A **61**, 533 (2005)
72. J. Cumings, A. Zettl, Chem. Phys. Lett. **316**, 211 (2000)
73. R. Bacon, J. Appl. Phys. **31**, 283 (1960)
74. K.S. Novoselov, A.K. Geim, S.V. Morozov, D. Jiang, S.V. Dubonos, I.V. Grigorieva, A.A. Firsov, Science **306**, 666 (2004)
75. X. Chen, R.A. Boulos, J.F. Dobson, C.L. Raston, Nanoscale **5**, 498 (2013)
76. D.A. Dikin, S. Stankovich, E.J. Zimney, R.D. Piner, G.H.B. Dommett, G. Evmenenko, S.T. Nguyen, R.S. Ruoff, Nature **448**, 457 (2007)
77. E. Perim, R. Paupitz, D.S. Galvão, J. Appl. Phys. **113**, 054306 (2013)
78. S.F. Braga, V.R. Coluci, S.B. Legoas, R. Giro, D.S. Galvão, R.H. Baughman, Nano Lett. **4**, 881 (2004)
79. H. Shioyama, T. Akita, Carbon **41**, 179 (2003)
80. P.J.F. Harris, Crit. Rev. Solid State Mater. Sci. **30**, 235 (2005)
81. V.V. Ivanovskaya, A. Zobelli, G. Seifert, A.L. Ivanovskii, JETP Lett. **85**, 626 (2007)
82. L.T. Sun, J.L. Gong, Z.Y. Zhu, D.Z. Zhu, Z.X. Wang, W. Zhang, J.G. Hu, Q.T. Li, Diam. Relat. Mater. **14**, 749 (2005)
83. V.V. Pokropivny, A.L. Ivanovskii, Russ. Chem. Rev. **77**, 837 (2008)
84. S.L. Rumyantsev, M.E. Levinshtein, A.D. Jackson, S.N. Mohammmad, G.L. Harris, M.G. Spencer, M.S. Shur, in *Properties of Advanced Semiconductor Materials GaN, AlN, InN, BN, SiC, SiGe*, ed by M.E. Levinshtein, S.L. Rumyantsev, M.S. Shur (Wiley, New York, 2001), p. 6792
85. H. Zhang, J.D. Fitzgerald, L.T. Chadderton, J. Yu, Y. Chen, Phys. Rev. B **74**, 045407 (2006)
86. T. Sekiguchi, Q. Liu, T. Tanaka, J. Hu, Y. Zhu, Y. Bando, Eur. Phys. J. Appl. Phys. **27**, 107 (2004)
87. Y.J. Chen, H.Z. Zhang, Y. Chen, Nanotechnology **17**, 786 (2006)
88. J. Zhan, X. Haoa, S. Wen, M. Jiang, Physica E **25**, 409 (2005)
89. C.N.R. Rao, F.L. Deepak, G. Gundiah, A. Govindaraj, Progr. Solid State Chem. **31**, 5 (2003)
90. P. Widmayer, H.G. Boyen, P. Ziemann et al., Phys. Rev. B **59**, 5233 (1999)
91. R.M. Wentzcovitch, S. Fahy, M.L. Cohen, S.G. Louis, Phys. Rev. B **38**, 6191 (1988)
92. K. Albe, Phys. Rev. B **55**, 6203 (1997)
93. Y.N. Xu, W.Y. Ching, Phys. Rev. B **44**, 7787 (1991)
94. R.T. Senger, S. Tongay, E. Durgun, S. Ciraci, Phys. Rev. B **72**, 075419 (2005)
95. D. Jacquemin, E.A. Perpete, B. Champagne, Phys. Chem. Chem. Phys. **4**, 432 (2002)
96. A. Abdurahman, A. Shukla, M. Dolg, Phys. Rev. B **65**, 115106 (2002)
97. X.Q. Shi, Z.X. Dai, X.H. Zheng, Z. Zeng, J. Phys. Chem. B **110**, 16902 (2006)
98. M. Qiu, K.M. Liew, J. Appl. Phys. **113**, 054305 (2013)
99. C.C. Kaun, H. Guo, P. Grütter, R.B. Lennox, Phys. Rev. B **70**, 195309 (2004)
100. A.R. Champagne, A.N. Pasupathy, D.C. Ralph, Nano Lett. **5**, 305 (2005)
101. Yu.M. Galperin, *Quantum Transport*. Lecture Notes (Lund University Press, 1998)
102. S. Datta, Nanotechnology **15**, S433 (2004)
103. C. Jain, M. Willander, J. Narayan, R. van Overstraeten, J. Appl. Phys. **87**, 965 (2000)
104. P. Ruterana, M. Albrecht, J. Neugebauer, *Nitride Semiconductors: Handbook on Materials and Devices* (Wiley, New York, 2003)
105. J.M. Wagner, *Structure and Lattice Dynamics of GaN and AlN: Ab Initio Investigations of Strained Polytypes and Superlattices* (PhD Thesis, Friedrich-Schiller-Universität, Jena, 2004)
106. F. Mireles, S.E. Ulloa, Phys. Rev. B **58**, 3879 (1998)
107. J.M. Vail, D. Schindel, A. Yang, O. Penner, R. Pandey, H. Jiang, M.A. Blanco, A. Costales, Q.C. Qiu, Y. Xu, J. Phys.: Condens. Matter **16**, 3371 (2004)
108. Yu.F. Zhukovskii, N. Pugno, A.I. Popov, C. Balasubramanian, S. Bellucci, J. Phys.: Condens. Matter **19**, 395021 (2007)

109. H. Morkoç, *Nitride Semiconductors and Devices*. Springer Series in Material Science (Springer, Berlin, 1999)
110. J.W. Kang, H.J. Hwang, Comput. Mater. Sci. **31**, 237 (2004)
111. T. Hanada, in *Oxide and Nitride Semiconductors*, ed by T. Yao, S.K. Hong, Processing, Properties, and Applications. Series Advances in Materials Research, vol. 12 (Springer, Berlin, Heidelberg, 2009), pp. 1–19
112. B.K. Meyer, *III-V Nitrides Semiconductors and Ceramics: From Material Growth to Device Applications* (Elsevier Health Sciences, Amsterdam, 1998)
113. I. Vurgaftman, J.R. Meyer, J. Appl. Phys. **94**, 3675 (2003)
114. S. Picozzi, G. Profeta, A. Continenza, S. Massidda, A.J. Freeman, Phys. Rev. B **65**, 165316 (2002)
115. T.K. Zywietz, J. Neugebauer, M. Scheffler, Appl. Phys. Lett. **74**, 1695 (1999)
116. C.I. Wu, A. Kahn, Appl. Phys. Lett. **74**, 546 (1999)
117. P. Kung, M. Razeghi, Opto-Electron. Rev. **8**, 201 (2000)
118. A.N. Enyashin, S. Gemming, G. Seifert, in *Materials for Tomorrow. Theory, Experiments and Modelling*, ed. by S. Gemming, M. Schreiber, J-B. Suck. Springer Series in Materials Science, vol. 93 (Springer, Berlin, Heidelberg, New York, 2006), pp. 33–57
119. C. Zhang, J. Appl. Phys. **111**, 043702 (2012)
120. Q. Peng, X.J. Chen, S. Liu, S. De, RSC Adv. **3**, 7083 (2013)
121. J. Goldberger, R. He, Y. Zhang, S. Lee, H. Yan, H.J. Choi, P. Yang, Nature **422**, 599 (2003)
122. Q. Wu, Z. Hu, X. Wang, Y. Lu, X. Chen, H. Xu, Y. Chen, J. Am. Chem. Soc. **125**, 10176 (2003)
123. C. Balasubramanian, V.P. Godbole, V.K. Rohatgi, A.K. Das, S.V. Bhoraskar, Nanotechnology **15**, 370 (2004)
124. C. Balasubramanian, S. Bellucci, P. Castrucci, M. De Crescenzi, S.V. Bhoraskar, Chem. Phys. Lett. **383**, 188 (2004)
125. S.M. Lee, Y.H. Lee, Y.G. Hwang, J. Elsner, D. Porezag, T. Frauenheim, Phys. Rev. B **60**, 7788 (1999)
126. D. Zhang, R.Q. Zhang, Chem. Phys. Lett. **371**, 426 (2003)
127. M. Zhao, Y. Xia, D. Zhang, L. Mei, Phys. Rev. B **68**, 235415 (2003)
128. Ş. Erkoç, O.B. Malcioglu, E. Taşci, J. Mol. Struct. (Theochem) **674**, 1 (2004)
129. Y.R. Jeng, P.C. Tsai, T.H. Fang, Nanotechnology **15**, 1737 (2004)
130. M. Zhao, Y. Xia, Z. Tan, X. Liu, F. Li, B. Huang, Y. Ji, L. Mei, Chem. Phys. Lett. **389**, 160 (2004)
131. B. Xu, A.J. Lu, B.C. Pan, Q.X. Yu, Phys. Rev. B **71**, 125434 (2005)
132. E. Durgun, S. Tongay, S. Çiraci, Phys. Rev. B **72**, 075420 (2005)
133. Z. Qian, S. Hou, J. Zhang, R. Li, Z. Shen, X. Zhao, Z. Xue, Physica E **27**, 81 (2005)
134. R.R. Zope, B.I. Dunlap, Phys. Rev. B **72**, 045439 (2005)
135. M. Zhao, Y. Xia, X. Liu, Z. Tan, B. Huang, C. Song, L. Mei, J. Phys. Chem. B **110**, 8764 (2006)
136. M. Simeoni, S. Santucci, S. Picozzi, B. Delley, Nanotechnology **17**, 3166 (2006)
137. Yu.F. Zhukovskii, A.I. Popov, C. Balasubramanian, S. Bellucci, J. Phys.: Condens. Matter **18**, S2045 (2006)
138. H. Pan, Y.P. Feng, J. Lin, J. Chem. Theory. Comput. **4**, 703 (2008)
139. Y. Guo, X. Yan, Y. Yang, Phys. Lett. A **373**, 367 (2009)
140. J.M. de Almeida, T. Kar, P. Piquini, Phys. Lett. A **374**, 877 (2010)
141. S. Nakamura, T. Mukai, M. Senoh, Appl. Phys. Lett. **64**, 1687 (1994)
142. H.M. Kim, T.W. Kang, K.S. Chung, J.P. Hong, W.B. Choi, Chem. Phys. Lett. **377**, 491 (2003)
143. T. Yamamoto, H.K. Yoshida, Jpn. J. Appl. Phys. **36**, Part 2, L180 (1997)
144. W. Han, Y. Bando, K. Kurashima, T. Sato, Appl. Phys. Lett. **73**, 3085 (1998)
145. D.A. Steigerwald, J.C. Bhat, D. Collins, R.M. Fletcher, M.O. Holcomb, M.J. Ludowise, P.S. Martin, S.L. Rudaz, IEEE J. Sel. Top. Quant. Electron. **8**, 310 (2002)
146. I. Ichimura, F. Maeda, K. Osato, K. Yamamoto, Y. Kasami, Jpn. J. Appl. Phys. **39**, 937 (2000)
147. M.A. Khan, X. Hu, G. Simin, J. Yang, R. Gaska, M.S. Shur, Appl. Phys. Lett. **77**, 1339 (2000)

148. S. Rajan, A. Chini, M.H. Wong, J. Appl. Phys. **102**, 044501 (2007)
149. M. Marques, L.K. Teles, L.G. Ferreira, Phys. Rev. B **75**, 033201 (2007)
150. S.H. Wei, A. Zunger, Appl. Phys. Lett. **69**, 2719 (1996)
151. J.E. Northrup, J. Neugebauer, J. Phys. Rev. B **53**, R10477 (1996)
152. R.A. Evarestov, *Quantum Chemistry of Solids. The LCAO First Principles Treatment of Crystals*. Springer Series in Solid State Sciences, vol. 153 (Springer, Berlin, 2007)
153. R.K. Paul, K.H. Lee, B.T. Lee, H.Y. Song, Mater. Chem. Phys. **112**, 562 (2008)
154. J. Su, G. Cui, M. Gherasimova, H. Tsukumato, J. Han, D. Ciubaru, H. Lim, L. Pfefferle, Y. He, A.V. Nurmikko, C. Broadbridge, A. Lehman. Appl. Phys. Lett. **86**, 013105 (2005)
155. L.H. Shen, X.F. Li, J. Zhang, Y.M. Ma, F. Wang, G. Peng, Q.L. Cui, G.T. Zou, Appl. Phys. A **84**, 73 (2006)
156. G.R. Yazdi, M. Syvajarvi, R. Yakimova, Appl. Phys. Lett. **90**, 123103 (2007)
157. Z. Zhou, J. Zhao, Y. Chen, P. von Ragué Schleyer, Z. Chen, Nanotechnology **18**, 424023 (2007)
158. G.A. Nemnes, J. Nanomater. **2013**, 408475 (2013)
159. C. Xu, L. Xue, C. Yin, G. Wang, Phys. Status Solidi (A) **198**, 329 (2003)
160. Q. Zhao, H. Zhang, X. Xu, Z. Wang, J. Xu, D. Yu, G. Li, F. Su, Appl. Phys. Lett. **86**, 193101 (2005)
161. L.E. Brus, J. Chem. Phys. **80**, 4403 (1984)
162. Y.K. Song, A.V. Nurmikko, M. Gherasimova, S.R. Jeon, J. Han, Phys. Status Solidi (A) **201**, 2721 (2004)
163. Y. Wu, G. Chen, H. Ye, Y. Zhu, S.H. Wei, Appl. Phys. Lett. **94**, 253101 (2009)
164. Y. Wu, G. Chen, H. Ye, Y. Zhu, S.H. Wei, J. Appl. Phys. **104**, 084313 (2008)
165. A. Mitrushchenkov, R. Linguerri, G. Chambaud, J. Phys. Chem. C **113**, 6883 (2009)
166. A. Mitrushchenkov, G. Chambaud, J. Yvonnet, Q.C. He, Nanotechnology **21**, 255702 (2010)
167. T.L. Mitran, A. Nicolaev, G.A. Nemnes, L. Ion, S. Antohe, Comput. Mater. Sci. **50**, 2955 (2011)
168. J. Yvonnet, A. Mitrushchenkov, G. Chambaud, Q.C. He, Comput. Methods Appl. Mech. Eng. **200**, 614 (2011)
169. M.H. Tsai, Z.F. Jhang, J.Y. Jiang, Y.H. Tang, L.W. Tu, Appl. Phys. Lett. **89**, 203101 (2006)
170. Z. Gao, Y. Gu, Y. Zhang, J. Nanomater. **2010**, 462032 (2010)
171. T. Markussen, A.P. Jauho, M. Brandbyge, Phys. Rev. B **79**, 035415 (2009)
172. E. Bourgeois, M.V. Fernandez-Serra, X. Blase, Phys. Rev. B **81**, 193410 (2010)
173. M. Mohr, C. Thomsen, Nanotechnology **20**, 115707 (2009)
174. D. Spirkoska, G. Abstreiter, A. Fontcuberta i Morral, Nanotechnology **19**, 435704 (2008)
175. L. Shen, Q. Cui, Y. Ma, Q. Li, Y. Ma, B. Liu, T. Cui, J. Phys. Chem. C **114**, 8241 (2010)
176. J.M. Soler, E. Artacho, J.D. Gale, A. Garcia, J. Junquera, P. Ordejón, D. Sánchez-Portal, J. Phys.: Condens. Matter **14**, 2745 (2002)
177. D.E. Angelescu, M.C. Cross, M.L. Roukes, Superlatt. Microsctruct. **23**, 673 (1998)
178. L.G.C. Rego, G. Kirczenow, Phys. Rev. Lett. **81**, 232 (1998)
179. A. Al Shaikhi, G.P. Srivastava, Phys. Rev. B **76**, 195205 (2007)
180. J.C. Li, C.L. Wang, H. Peng, M.X. Wang, R.Z. Zhang, H.C. Wang, J. Liu, M.L. Zhao, L.M. Mei, J. Appl. Phys. **108**, 063702 (2010)
181. A. Gulans, I. Tale, Phys. Status Solidi (C) **4**, 1197 (2007)
182. D.J. Carter, J.D. Gale, B. Delley, C. Stampfl, Phys. Rev. B **77**, 115349 (2008)
183. D.Q. Fang, A.L. Rosa, Th. Frauenheim, R.Q. Zhang, Appl. Phys. Lett. **94**, 073116 (2009)
184. R. Agrawal, H.D. Espinosa, Nano Lett. **11**, 786 (2011)
185. P. Dev, H. Zeng, P. Zhang, Phys. Rev. B **82**, 165319 (2010)
186. D.J. Carter, M. Fuchs, C. Stampfl, J. Phys.: Condens. Matter **24**, 255801 (2012)
187. Q. Wang, Q. Sun, P. Jena, Nano Lett. **5**, 1587 (2005)
188. Z. Wang, J. Li, F. Gao, W.J. Weber, J. Appl. Phys. **108**, 044305 (2010)
189. C.C. Chen, C.C. Yeh, C.H. Chen, M.Y. Yu, H.L. Liu, J.J. Wu, K.H. Chen, L.C. Chen, J.Y. Peng, Y.F. Chen, J. Am. Chem. Soc. **123**, 2791 (2001)
190. J.R. Kim, H.M. So, J.W. Park, J.J. Kim, Appl. Phys. Lett. **80**, 3548 (2002)

191. Y.K. Byeun, K.S. Han, S.C. Choi, J. Electroceram. **17**, 903 (2006)
192. S. Dhara, A. Datta, C.T. Wu, Z.H. Lan, K.H. Chen, Y.L. Wang, C.W. Hsu, C.H. Shen, L.C. Chen, C.C. Chen, Appl. Phys. Lett. **84**, 5473 (2004)
193. B.S. Simpkins, L.M. Ericson, R.M. Stroud, K.A. Pettigrew, P.E. Pehrsson, J. Cryst. Growth **290**, 115 (2006)
194. B.S. Xu, L.Y. Zhai, J. Liang, S.F. Ma, H.S. Jia, X.G. Liu, J. Cryst. Growth **291**, 34 (2006)
195. H.Y. Peng, N. Wang, X.T. Zhou, Y.F. Zheng, C.S. Lee, S.T. Lee, Chem. Phys. Lett. **359**, 241 (2002)
196. T. Kuykendall, P.J. Pauzauskie, Y. Zhang, J. Goldberger, D. Sirbuly, J. Denlinger, P. Yang, Nat. Mater. **3**, 524 (2004)
197. S.D. Hersee, X. Sun, X. Wang, Nano Lett. **6**, 1808 (2006)
198. S. Gradecak, F. Qian, Y. Li, H.G. Park, C.M. Lieber, Appl. Phys. Lett. **87**, 173111 (2005)
199. M. He, P. Zhou, S. Mohammad, G. Harris, J. Halpern, R. Jacobs, W. Sarney, L. Salamanca-Riba, J. Cryst. Growth **231**, 357 (2001)
200. G. Cheng, A. Kolmakov, Y. Zhang, M. Moskovits, R. Munden, M.A. Reed, G. Wang, D. Moses, J. Zhang, Appl. Phys. Lett. **83**, 1578 (2003)
201. H.J. Choi, H.K. Seong, J. Chang, K.I. Lee, Y.J. Park, J.J. Kim, S.K. Lee, R. He, T. Kuykendall, P. Yang, Adv. Mater. **17**, 1351 (2005)
202. J.E. Northrup, R.D. Felice, Phys. Rev. B **56**, R4325 (1997)
203. R.R. Reeber, K. Wang, MRS Internet J. Nitride Semicond. Res. **6**, 3 (2001)
204. C.Y. Nam, P. Jaroenapibal, D. Tham, D.E. Luzzi, S. Evoy, J.E. Fischer, Nano Lett. **6**, 153 (2006)
205. J.C. Johnson, H.J. Choi, K.P. Knutsen, R.D. Schaller, P. Yang, R.J. Saykally, Nat. Mater. **1**, 106 (2002)

R.A. Evarestov

Theoretical Modeling of Inorganic Nanostructures

Symmetry and ab-initio Calculations of Nanolayers, Nanotubes and Nanowires

R.A. Evarestov
Department of Chemistry
St. Petersburg State University
St. Petersburg
Russia

Printed on acid-free paper